nature COMMUNICATIONS

ARTICLE

https://doi.org/10.1038/s41467-019-12230-5 OPEN

Local-to-global signal transduction at the core of a Mn^{2+} sensing riboswitch

Krishna C. Suddala[1,6], Ian R. Price[2,6], Shiba S. Dandpat[1], Michal Janeček[3,4], Petra Kührová[4,5], Jiří Šponer[3,5], Pavel Banáš[3,4,5], Ailong Ke[2] & Nils G. Walter[1]

The widespread Mn^{2+}-sensing *yybP-ykoY* riboswitch controls the expression of bacterial Mn^{2+} homeostasis genes. Here, we first determine the crystal structure of the ligand-bound *yybP-ykoY* riboswitch aptamer from *Xanthomonas oryzae* at 2.96 Å resolution, revealing two conformations with docked four-way junction (4WJ) and incompletely coordinated metal ions. In >100 μs of MD simulations, we observe that loss of divalents from the core triggers local structural perturbations in the adjacent docking interface, laying the foundation for signal transduction to the regulatory switch helix. Using single-molecule FRET, we unveil a previously unobserved extended 4WJ conformation that samples transient docked states in the presence of Mg^{2+}. Only upon adding sub-millimolar Mn^{2+}, however, can the 4WJ dock stably, a feature lost upon mutation of an adenosine contacting Mn^{2+} in the core. These observations illuminate how subtly differing ligand preferences of competing metal ions become amplified by the coupling of local with global RNA dynamics.

[1] Single Molecule Analysis Group and Center for RNA Biomedicine, Department of Chemistry, University of Michigan, Ann Arbor, MI 48109, USA. [2] Department of Molecular Biology and Genetics, Cornell University, Ithaca, NY 14850, USA. [3] Institute of Biophysics of the Czech Academy of Sciences, Kralovopolská 135, Brno 612 65, Czech Republic. [4] Department of Physical Chemistry, Faculty of Science, Palacký University, tř. 17 listopadu 12, Olomouc 771 46, Czech Republic. [5] Regional Centre of Advanced Technologies and Materials, Faculty of Science, Palacký University, tř. 17 listopadu 12, Olomouc 771 46, Czech Republic. [6] These authors contributed equally: Krishna C. Suddala, Ian R. Price. Correspondence and requests for materials should be addressed to A.K. (email: ailong.ke@cornell.edu) or to N.G.W. (email: nwalter@umich.edu)

Riboswitches are structured RNA domains commonly found in the 5′-untranslated regions of bacterial mRNAs, where they regulate many essential and virulence genes in response to binding of a specific ligand[1–3]. Currently, there are over 40 different riboswitch classes known to respond to ligands ranging from metabolites[4], enzyme cofactors[5], signaling molecules[6–8], tRNAs[9], and to metal ions[10–12]. Ligand binding generally stabilizes a conformation of the riboswitch that modulates either Rho-independent transcriptional termination or translation initiation through accessibility of the Shine-Dalgarno (SD) sequence. The static ligand-bound structures, and the ligand-recognition modes, of a number of riboswitch aptamers have been determined at atomic resolution[2,12–14]. Often, the ligand occupies a linchpin position in the global fold where distal residues of the RNA are brought together; however, the dynamic paths by which the local binding of a ligand as small as a metal ion are transduced into the large-scale molecular rearrangements necessary for a regulatory decision by the gene expression machinery largely remain enigmatic[14].

The *yybP–ykoY* RNA motif is one of the most widespread riboswitches across bacteria, including many human and plant pathogens[15–17]. It has evolved to sensitively detect Mn^{2+} metal ions and broadly regulate a variety of genes, particularly those involved in Mn^{2+} homeostasis, at the levels of either transcription or translation[12,15,18]. We and others have previously solved crystal structures of the aptamer domain of this riboswitch[12,19], henceforth simply referred to as "riboswitch", revealing that it senses the charge, geometry, and Lewis-acid hardness of Mn^{2+} by forming direct inner-sphere contacts from five phosphoryl oxygens and the N7 of an invariable adenosine. The global structure showed that formation of the Mn^{2+} binding site requires "docking" of two distal helical legs of a four-way junction (4WJ) to form a paperclip-shaped global architecture, facilitated by an A-minor interaction and a second, nonspecific divalent metal ion binding site (Fig. 1a)[12]. However, the transduction of ligand binding in this metal-sensing core into global structural changes that affect the distal helix P1.1 involved in riboswitching is not understood, rendering it an archetypical representative of our level of understanding of many crystallized riboswitches[14].

Here, we first solve the structures of two ligand-binding states of the *yybP–ykoY* transcriptional riboswitch from the rice pathogen *X. oryzae*[20,21], captured in distinct conformations that offer snapshots of structural changes *en route* to full ligand binding. We then use these conformers for atomistic molecular dynamics (MD) simulations that reveal how ligand-dependent local structural perturbations in the metal-sensing core are linked to the stability of distal P1.1 helix to affect riboswitching. Finally, using single-molecule FRET (smFRET), we investigate the global structural dynamics of the riboswitch in the presence of varying concentrations of Mg^{2+} and Mn^{2+}, as well as other transition metals, revealing a previously unobserved extended conformation of the riboswitch. We show that addition of Mg^{2+} induces two kinetically distinct docked and undocked conformations that are in dynamic equilibrium with one another. In contrast, upon addition of submillimolar Mn^{2+}, the riboswitch adopts a stably docked (SD) conformation that becomes abolished upon mutation of the conserved core adenosine. Taken together, our work reveals the ligand-dependent (un)folding pathway of the Mn^{2+} sensing riboswitch as a guide for how subtle binding preferences distinguishing two similar metal ion ligands cascade through the coupling of local with global RNA conformational dynamics into powerful effects on gene regulation.

Results

RNA-based Mn^{2+} sensing by stepwise removal of metal ion hydration. Previously, we determined the structures of the Mn^{2+}-bound and Mn^{2+}-free states from the *L. lactis* (Llac-Mn PDB: 4Y1I) and *E. coli* (PDB: 4Y1M) *yybP–ykoY* riboswitches, respectively[12]. The Mn^{2+}-sensing core was shown to be first bridged via the binding of a Mg^{2+} ion to a nearby site, then undergoes further conformational changes into the final Mn^{2+}-bound state. Importantly, Mn^{2+} sensing involves the complete stripping of the Mn^{2+} ion's hydration shell, substituted with a set of selective metal–RNA contacts. Since completely dehydrating a metal ion is energetically costly, this process was speculated to take place in stepwise fashion, possibly achieved by a stepwise set of local conformational changes in the metal ion sensing loop[12]. However, no structural intermediates have been captured so far; hence our understanding of the selective metal ion sensing process has remained vague.

In this study, we report the partial and complete Mn^{2+} dehydration states, captured in the same crystal lattice of the *X. oryzae yybP–ykoY* riboswitch and resolved to 2.96 Å (Xory-Mn, Fig. 1a, b and Table 1). This riboswitch controls the *yebN* Mn^{2+} efflux pump gene[21] in *X. oryzae, a* phytopathogenic bacterium that causes rice blight. To facilitate crystallization, the wild-type (WT) *Xory* sequence was modified distally from the metal ion sensing core not to affect metal ion binding, tightening the 4WJ and stabilizing P1.1 to aid crystallization (see Methods, Fig. 1a). The crystal lattice contains two Xory-Mn riboswitch molecules (Supplementary Figs. 1–4 and 6). While their overall architecture is similar to that of the previously determined *L. lactis* 4Y1I (Llac-Mn) structure, with an r.m.s.d of ~2.5 Å, they represent two distinct functional states (Fig. 1c). Conformer 1 is clearly in the canonical Mn^{2+}-sensing state despite minor sequence differences in the metal ion binding core, hence providing a comparable reference point for mechanistic interpretation. Its structure superimposes well with the previously determined, canonical, Mn^{2+}-bound *L. lactis* structure (Fig. 1c). Both feature two coaxial stacked "legs" connected at the top by the 4WJ, a superimposable metal ion sensing core, with bound Mn^{2+} and Mg^{2+} ions in superimposable positions[12] (Fig. 1c). As in Llac-Mn, the L1 loop in Xory-Mn adopts a sarcin-ricin-like motif (SRL-like)[19] and extrudes a conserved A10 to form a cross-helix A-minor interaction with helix P3.1 above L3 (Figs. 1c and 2a, b)[12]. The L3 loop is extruded from the opposite side of the helical stacks, adopting a highly compressed conformation and stacks below A10 in L1. The close juxtaposition of phosphates in the L1–L3 interface creates a metal ion binding hotspot. In Llac-Mn, a largely inner-sphere coordinated (five phosphoryl oxygens and one water molecule) metal ion is located above the A10 residue (Supplementary Fig. 5). Both Mg^{2+} and Mn^{2+} can access this site[12]; we will henceforth refer to it as $M_{A,Mg}$ because the physiological concentration of Mg^{2+} is usually 100-fold higher than Mn^{2+}. This metal ion binding site is preserved in Xory-conformer 1, although the inner-sphere contacts to A10 and G8 are either lost or replaced by outer-sphere contacts (Fig. 2a). Of note, although 80 mM $SrCl_2$ were present in the crystallization buffer, discernible strontium anomalous signals were found in many sites of Xory-conformer 1 but almost none in the $M_{A,Mg}$ site (Supplementary Fig. 3), suggesting that, like Llac-Mn, Xory-conformer 1 prefers smaller divalent ions such as Mg^{2+} or Mn^{2+} in $M_{A,Mg}$. Mn^{2+} is coordinated specifically in a nearby site ($M_{B,Mn}$), through complete dehydration and a Mn^{2+}-specific "soft" contact from the N7 of an invariable adenosine residue (A41 in *Llac* and A48 in *Xory*)[12] (Fig. 1d). In Llac-Mn, the four residues following the Mn^{2+}-sensing adenosine in the L3 loop form a three-residue stack with U43 mediating a U-turn motif[12]. Due to sequence differences ($ACA_{48}\underline{U_{49}ACU_{52}}$ in *Xory vs* $UCA_{41}\underline{AU_{43}UC}$ in *Llac*), while the three-residue-stacking theme is preserved, the U-turn is found to be mediated by the first residue (U_{49}) in Xory-conformer 1, rather than the second

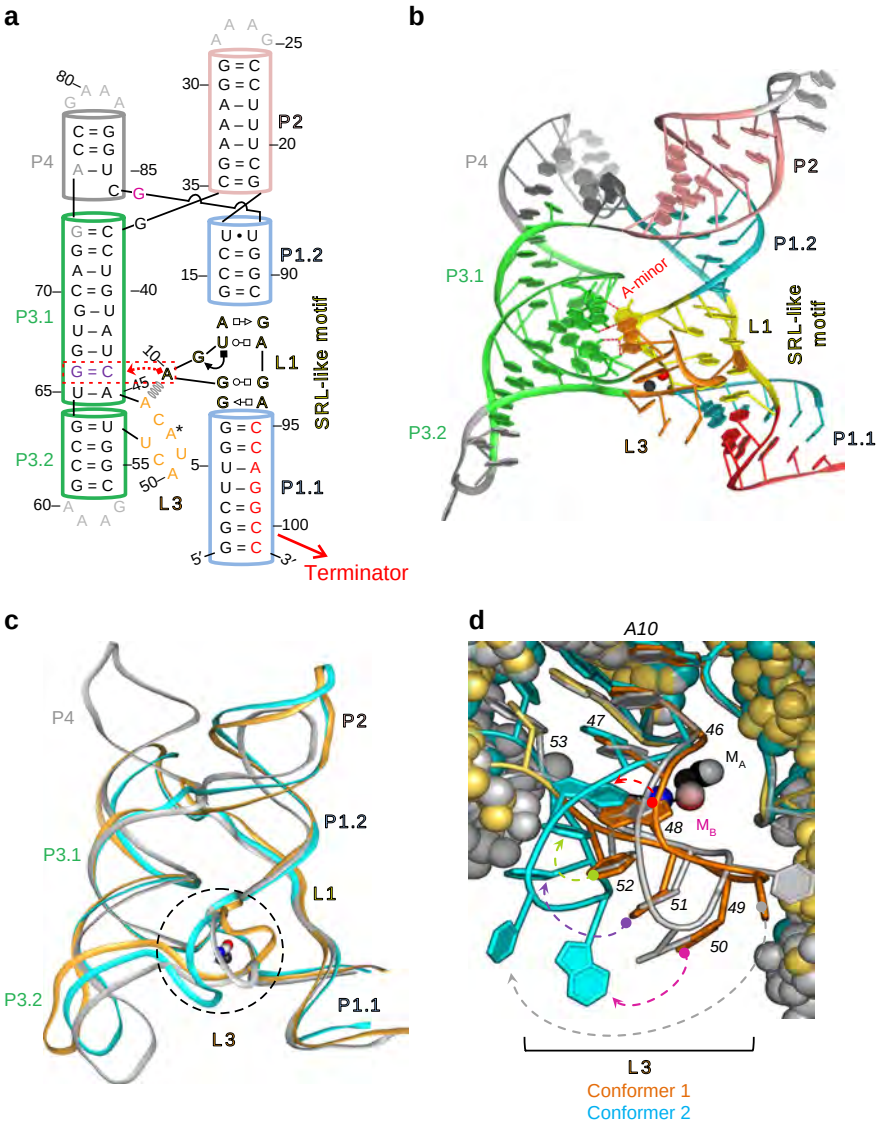

Fig. 1 Sequence and structure of the *X. oryzae* (*Xory*) crystal structure. **a** Secondary structure of the *X. oryzae* crystal construct. A native CA dinucleotide was omitted between G73–A74 for crystallization purposes only. The A-minor interaction between L1 and L3 and the SRL-like conformation of L1 is shown. **b** Crystal structure of Conformer 1 (PDB ID: 6N2V) with different secondary structures labeled. **c** Comparison of overall structures of Conformers 1 (orange) and 2 (cyan) and the previous Mn^{2+}-bound *L. lactis* structure (gray). The two molecules in the asymmetric unit are overall fairly similar. However, they differ dramatically at the metal ion binding sites (dotted circle). **d** Conformer 1 (orange) is relatively similar to the *L. lactis* structure at the $M_{B,Mn}$ binding site. All the same metal ion contacts are made, although U49, away from the Mn^{2+} site, is shifted (gray dotted arrow). Conformer 2 (cyan) differs in that a metal ion is still bound at the $M_{B,Mn}$ site, but only half of the metal ion contacts are made, and the binding site A48 is flipped (red dotted arrow) to expose N1 rather than N7. U49 (gray arrow), A50 (magenta arrow), C51 (purple arrow), and U52 (green arrow) are all significantly shifted from the previously reported Mn-bound conformation

residue (U_{43}) in Llac-Mn (Fig. 1d and Supplementary Fig. 5). Despite the idiosyncratic folding in the L3 loop, the inner-sphere contacts to Mn^{2+} are mediated by the same set of phosphates and the invariable adenosine, suggesting that they utilize the same mechanism to sense Mn^{2+} (Fig. 2a).

Whereas Xory-conformer 1 serves as a reference point to reveal common themes in Mn^{2+} sensing among *yybP–ykoY* riboswitches, Xory-conformer 2 provides a rare, intermediate snapshot of the riboswitch sampling for Mn^{2+} through a partial dehydration process. The Mg^{2+} ion is more loosely coordinated in the $M_{A,Mg}$ site; an inner-sphere coordination from U52 of the L3 loop is lost (Fig. 2b). This is because the L3 loop has yet to adopt its final Mn^{2+}-sensing conformation, as the first four residues in L3 have not formed the ordered stacks atop the invariable A48. Importantly, a partially dehydrated metal ion is already present at the $M_{B,Mn}$ site despite lacking half of the contacts seen in Conformer 1, where only the inner-sphere contacts by the phosphates of A45 and A46 are preserved (Fig. 2b). Interestingly, the electron density is sufficiently clear to suggest that the invariable adenosine residue (A48) rotates slightly and orients its N1 group closer than N7 towards $M_{B,Mn}$ (a 2.6 Å outer-sphere contact). Also of note, the temperature B-factors for L3 are higher in Conformer 2 than Conformer 1 (Fig. 2c, d), indicating elevated conformational flexibility. Importantly, this includes larger flexibility around P1.1, suggesting a possible link between the flexibilities of these two key regions. We interpret this conformation as representing the functional state of the *yybP–ykoY* riboswitch sampling metal ions

Table 1 X-ray crystallographic data collection and refinement statistics for the *X. oryzae* yybP-ykoY Mn^{2+} riboswitch

Xory yybP-ykoY riboswitch	Crystal 1
Data collection	
Space group	P 21 21 21
Cell dimensions	
a, *b*, *c* (Å)	81.32, 85.19, 92.49
α, *β*, *γ* (°)	90, 90, 90
Resolution (Å)	62.66–2.96 (3.07–2.96)*
R_{sym} or R_{merge}	0.110 (1.51)
$I/\sigma I$	14.2 (1.26)
Completeness (%)	99.83 (99.63)
Redundancy	81.90
CC1/2	1 (0.599)
CC*	1 (0.866)
Refinement	
Resolution (Å)	62.66–2.96 (3.07–2.96)
No. of reflections	13901 (1361)
R_{work}/R_{free}	0.205 (0.220)
No. of atoms	
RNA	4214
Ligand/ion	120
Water	7
B-factors	
RNA	69.17
Ligand/ion	93.43
Water	66.69
R.M.S. deviations	
Bond lengths (Å)	0.005
Bond angles (°)	0.59
PDB accession code	6N2V

Note that the data were mildly anisotropic, with reflections along the reciprocal axis stronger. Thus, I/sigma for these reflections was well over 1.2 (indeed, over 1.5 up to 2.85 Å resolution)
*One crystal was used. Values in parentheses are for highest-resolution shell

in solution. The partial dehydration process selects a metal ion with an ionic radius similar to Mn^{2+}. Mg^{2+} could in theory access the site, however, the N1 and N7 functional groups in the invariable adenosine residue would favor a softer metal ion such as Mn^{2+} (Fig. 2b). We envision that a further conformational transition to that in Conformer 1 would complete the metal ion selection process, as this process would exert additional stringency by not only selecting ionic radius, but also specifying an octahedral coordination and a clear preference for a "soft" transition metal ion (Fig. 2a, b). Taken together, our crystal structures provide important insights into the stepwise metal-sensing process and form the basis for the following MD simulations.

Effect of $M_{A,Mg}$ and $M_{B,Mn}$ inner-sphere contacts on L3 stacking. To provide deeper insights into the RNA dynamics associated with metal ion identity, we performed 43 atomistic MD simulations, equivalent to a total of 113 µs of real-time (see Supplementary Table 1, Methods), with different metal ions in the $M_{A,Mg}$ and $M_{B,Mn}$ sites and starting either from Xory-Mn Conformers 1 or 2 (as reported here) or from *L. lactis* structures (PDB IDs 4Y1I and 6CB3)[12,19]. We found that the arrangement of the ion binding sites in chain A of the 6CB3 *L. lactis* structure involved three Cd^{2+} ions and required the deprotonated form of uracil $U44^{-}$ to prevent loss of its first-shell coordination in the simulations. In addition, the replacement of the Cd^{2+} ions by one Mn^{2+} and two Mg^{2+} ions in the $M_{B,Mn}$, $M_{A,Mg}$, and M_C ion binding sites resulted in modest reorganization of their first-shell coordination spheres even in the presence of a deprotonated $U44^{-}$. Therefore, this particular arrangement of ion binding sites appears to be specific for large Cd^{2+} ions, likely due to their enhanced affinity to nitrogen ligands and preference for hepta-coordination over the native Mn^{2+} ion (Supplementary Discussion, Supplementary Note 3 and Supplementary Figs. 11–14). Therefore, we view this specific arrangement around the toxic and xenobiotic Cd^{2+} ions as not fully relevant for physiological Mn^{2+}/Mg^{2+} ionic conditions.

As expected, given the limited timescales compared to experiments[22,23], we found that our simulations generally maintained quite stable inner-sphere contacts for divalent metal ions, including their coordination with water molecules (Fig. 3a). To accelerate these dynamics, we performed additional MD simulations that replaced one or both divalent ions at the $M_{A,Mg}$ and $M_{B,Mn}$ ion binding sites with monovalent K^{+} ions (Supplementary Table 1). Replacement of divalent ions by monovalents increases flexibility of the starting ion-binding arrangement, which allows us to observe more local dynamics on the simulation timescale while retaining most relevant aspects of ion binding, since monovalent and divalent ions do compete for the same binding sites.[22,23] Indeed, the global architecture of the riboswitch was maintained except for local perturbations of L3 and a variable P2–P4 interhelical angle (Supplementary Figs. 7, 8, and Supplementary Note 1).

The simulations revealed that the inner coordination spheres of monovalent ions in both the $M_{A,Mg}$ and $M_{B,Mn}$ sites were significantly more stable when the second binding site was occupied by a divalent rather than monovalent ion (Fig. 3a). This observation suggests that binding of the divalent ion into one binding site helps pre-organize and stabilize the second binding site, consistent with the notion of cooperativity between $M_{A,Mg}$ and $M_{B,Mn}$. Furthermore, while some experimentally observed inner-sphere contacts remained very stable upon replacement with a monovalent, other contacts were lost (Fig. 3a–c). Notably, the bridging inner-sphere contacts of the U52 phosphate with the $M_{A,Mg}$ ion and those of the C51 and G9 phosphates with the $M_{B,Mn}$ metal ion were found to be most labile across all simulations (Fig. 3a, Supplementary Table 2, and Supplementary Figs. 15–19). These are the same inner-sphere contacts found to be lost in the crystallized Conformers 1 and 2 compared to the 4Y1I and 6CB3 (chain B) *L. lactis* structures, supporting the notion that the crystallized *X. oryzae* Conformers are relevant as *en route* to (un) folding of the metal ion binding sites. In contrast, the inner-shell contacts of the A46 phosphate with the ions in both $M_{A,Mg}$ and $M_{B,Mn}$, as well as that of the G9 phosphate with the ion in $M_{A,Mg}$, were stable across all simulations (Fig. 3a, Supplementary Table 2, and Supplementary Figs. 15–19). These interactions are likely stabilized by coupling of the A-minor interaction of A10 to the G66–C44 base pair and associated stacking of A10 on the neighboring A46. All these interactions are parts of the L1–L3 tertiary docking contact and remained stable across all simulations (Fig. 3d).

We also found the dynamics of the entire L3 loop to be sensitive to the type of ion in the $M_{B,Mn}$ site. When Mn^{2+} in the $M_{B,Mn}$ site was replaced with K^{+}, the flexibility of the L3 loop was increased so that the loop populated various conformations with broken stacking patterns (Fig. 3e and Supplementary Note 4). These perturbations originated from the weakened inner-sphere contact of the A48(N7) nitrogen to the $M_{B,Mn}$ metal, suggesting that the L3 loop is involved in direct sensing of the Mn^{2+} ion by forming a linchpin to support a tight stacking patterns only in the presence of the native Mn^{2+} (Fig. 3e).

Stability of the L1 loop requires an A-minor interaction. To complement our probing of structural dynamics in the docked state with those in the undocked state, we performed additional

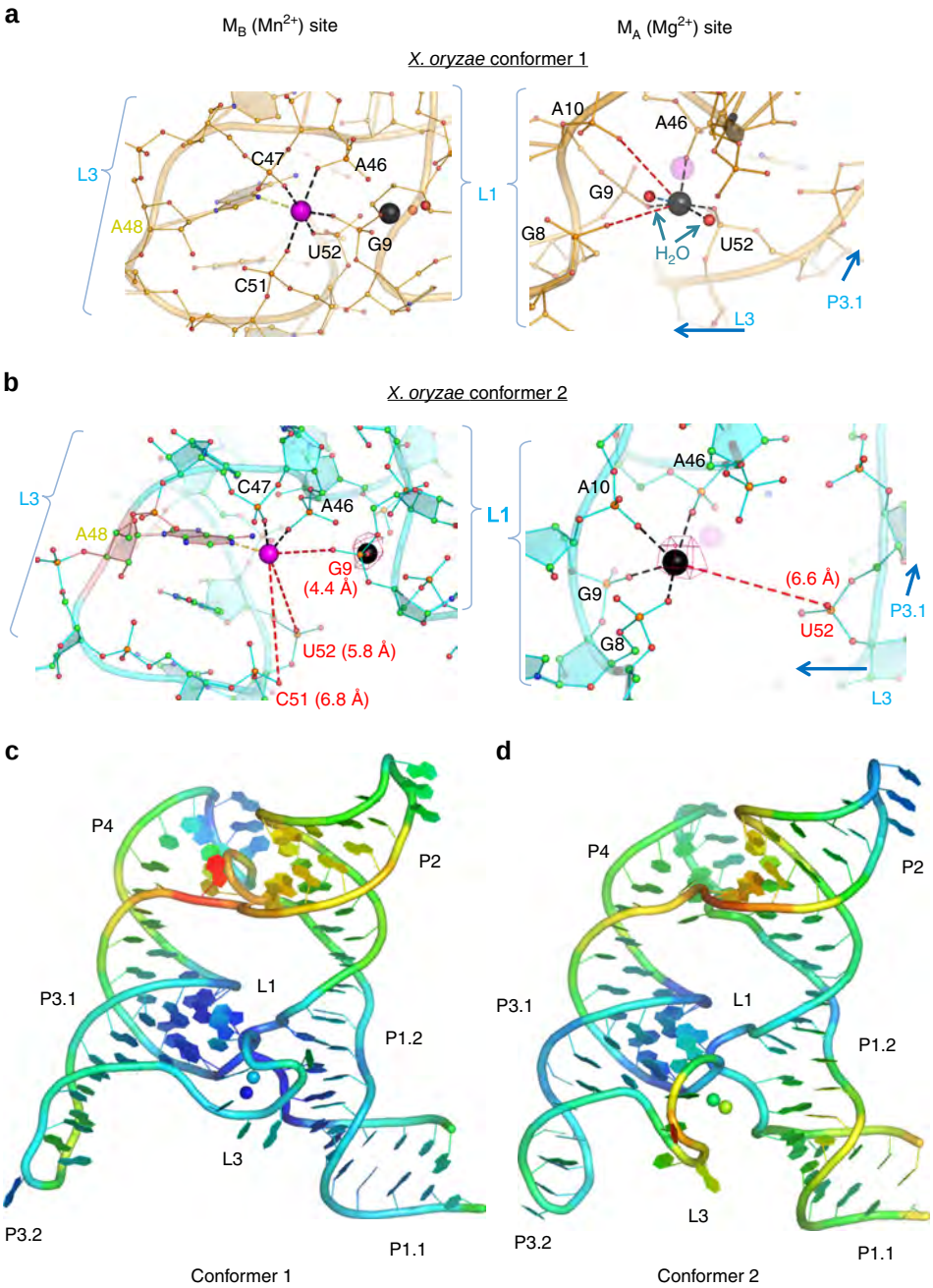

Fig. 2 Conformational differences in the metal ion binding sites and B-factors in the structures. Close-up view of the $M_{A,Mg}$ (black) and $M_{B,Mn}$ (purple) metal ion binding sites of **a** Conformer 1 and **b** Conformer 2 showing different contacts with surrounding L1 and L3 residues. Waters are shown as red spheres. The lost metal ion contacts are shown as red dashed lines with their distances. The anomalous difference map at 4σ (magenta mesh) shows that Sr^{2+} is not observed in Conformer 1 and weakly occupies the $M_{A,Mg}$ site but not the $M_{B,Mn}$ site in Conformer 2. The Llac-Mn structure is shown in Supplemental Fig. 5 in the same orientation for comparison. Overall *X. oryzae* Conformer 1 (**c**) and Conformer 2 (**d**) structures, colored by individual atomic temperature B-factors (range: 38–135 Å^2 for Conformer 1, 44–170 Å^2 for Conformer 2). Notice both are well-structured in L1 and in P3 around the binding site. However, Conformer 1 is much more tightly structured in L3 than is Conformer 2. Also, the metal ions in Conformer 1 are somewhat less variable. In both molecules, there is flexibility around the 4WJ

MD simulations of the segment consisting only of P1.1, P1.2, and L1. We started these undocked simulations from either of the two Xory-Mn Conformers and Llac-Mn structure (Supplementary Table 1), with the aim to reveal their structural dynamics in the absence of the L1–L3 docking contact. While the L1 loop in the context of the entire riboswitch with its docked L1–L3 interaction always populated the SRL-like conformation, two of our three undocked simulations lost this motif (Fig. 3f, g, Supplementary Fig. 22, and Supplementary Note 5). In particular, in one of the simulations we observed loss of the G9–G93 *trans* Watson–Crick/Hoogsteen and G8–A94 *trans* Sugar-Edge/Hoogsteen base pairing[24] as well as the S-turn[25] that forms part of the $M_{A,Mg}$ site (Fig. 3f, g). The former two base pairs are coaxially stacked on the P1.1 stem, suggesting that their loss may highlight the beginning of a transduction path by which P1.1 could become destabilized.

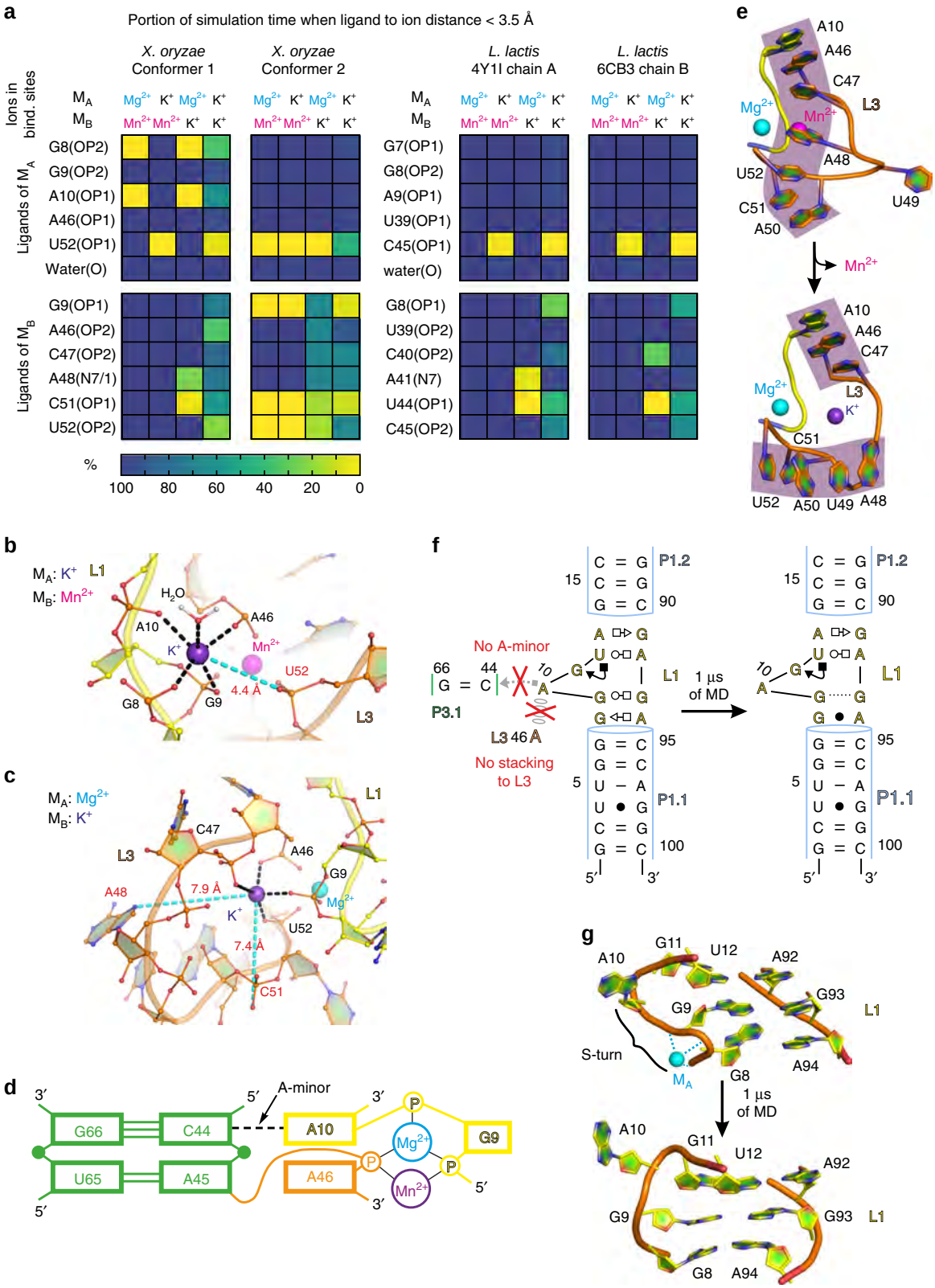

Fig. 3 Structural dynamics of inner-shell ligands of the $M_{A,Mg}$ and $M_{B,Mn}$ sites, L3 and L1 loops as revealed by MD simulations. **a** The population of native inner-shell contacts in the $M_{A,Mg}$ and $M_{B,Mn}$ sites in percent as a function of the type of ion in these sites. A representative structure of the **b** $M_{A,Mg}$ and **c** $M_{B,Mn}$ site as typically observed in MD simulations with a K^+ ion occupying the site. The most labile inner-shell contacts are depicted in cyan. **d** 2D representation of the most stable part of the L1–L3 tertiary interaction that is likely anchored by the A-minor interaction and related A10|A46 stacking. **e** Partial unfolding of the stacking pattern in the L3 loop observed upon replacement of Mn^{2+} with K^+ in the $M_{B,Mn}$ site. **f** The loss of native G9–G93 *trans* Watson-Crick/Hoogsteen and G8–A94 *trans* Sugar-Edge/Hoogsteen base pairing, and **g** loss of the S-turn backbone conformation involving a phosphate notch forming part of the $M_{A,Mg}$ ion binding site in response to loss of the L1–L3 tertiary interaction with its A10...G66 = C44 A-minor interaction

smFRET reveals an undocked state that docks upon Mg^{2+} addition. To probe the global structural dynamics in the presence of Mg^{2+} and Mn^{2+}, we used smFRET to monitor fluorophores positioned on the distal legs of the *Xory* riboswitch (Fig. 4a, Supplementary Fig. 23, and Methods). smFRET traces at 100 mM KCl in the absence of any divalent metal ions showed a stable low-FRET value of ~0.1 without global dynamics (Fig. 4b), with a population FRET histogram displaying a single peak centered on ~0.13 ± 0.10 (mean ± standard deviation) (Fig. 4c). The non-dynamic nature of the traces is also evident as an on-diagonal contour centered at ~0.13 in the transition occupancy density plot (TODP), which represents as a heat map the fraction of single molecule traces that exhibit any given specific initial-to-final FRET transition at least once (Fig. 4d and Methods)[26]. This FRET value corresponds to an estimated distance of ~74 Å between the two fluorophores and suggests an extended, stably undocked (SU) conformation where the two RNA legs are distal and do not interact, unlike the docked crystal structure (Fig. 1b).

Addition of Mg^{2+} up to 0.1 mM does not result in significant changes in the FRET histograms since almost all traces remain in the SU conformation, with ~3% of them showing brief excursions into a higher ~0.6 FRET state (Supplementary Fig. 24). Further raising the Mg^{2+} concentration results in more dynamic traces transiently adopting this high-FRET state, accompanied by a corresponding decrease in the population of SU traces (Fig. 4b–d and Supplementary Fig. 24). At a near-physiological concentration of 1 mM Mg^{2+}, the time- and population-averaged distribution between low- and high-FRET, with mean FRET values of ~0.15 ± 0.11 (49%) and 0.63 ± 0.14 (51%), respectively, became almost equal (Fig. 4c). A FRET value of 0.63 corresponds to a distance of ~49 Å between the two labeled RNA arms, similar to the distance observed in the crystal structures, suggesting adoption of the compact "docked" conformation. Reaching 10 mM Mg^{2+}, the fraction of docked conformation further increases and saturates at ~69%, with a sigmoidal Mg^{2+} concentration dependence that fit well with a Hill equation to yield a half-saturation point of $K_{1/2}$ ~ 0.6 mM and a cooperatively coefficient of $n = 1.7$ (Fig. 4e). These data demonstrate that the Mn^{2+} riboswitch adopts an extended SU conformation in the absence of divalents, which increasingly samples transient docked conformations upon a rise in Mg^{2+} concentration.

At a low-Mg^{2+} concentration of 0.1 mM, single-exponential kinetics are observed with a slow docking rate constant, k_{dock} ~ 0.56 s^{-1}, and a fast undocking rate constant, k_{undock} ~ 12.5 s^{-1} (Fig. 4f and Supplementary Fig. 25). Further increasing the Mg^{2+} concentration to 1 mM results in the emergence of double-exponential kinetics in both k_{dock} and k_{undock}. The docking kinetics exhibit k_{dock}^{fast} ~ 6.25 s^{-1} and k_{dock}^{slow} ~ 0.76 s^{-1}, while the undocking kinetics display k_{undock}^{fast} ~ 3.70 s^{-1} and k_{undock}^{slow} ~ 1.21 s^{-1} (Fig. 4f and Supplementary Fig. 25). The TODP further shows that a majority (82%) of traces are dynamically transitioning between the two FRET states, as highlighted by dominant off-diagonal contours, while only a small fraction (~18%) remains in the stable low-FRET state (Fig. 4d). The double-exponential kinetics arises from two distinct populations: dynamic docked (DD) and dynamic undocked (DU) traces corresponding to molecules residing largely in the docked and undocked states, respectively (Fig. 4g). Among the dynamic traces, ~65% were DD, while ~35% were DU traces. As observed for other RNAs that undergo docking of two adjacent helical arms[27–33], the heterogeneity observed in the population is largely static and molecular behaviors interconvert only rarely (<2% of traces) over the experimental timescale (5–10 min) (Fig. 4h). Interconversion between the DU and DD behaviors is observed more readily, however, when first chelating, then reintroducing Mg^{2+} (Fig. 4i), suggesting that they represent kinetically trapped conformations on a deeply rugged folding free energy landscape[34,35].

Submillimolar Mn^{2+} uniquely yields a SD riboswitch. We next asked what specific effect Mn^{2+} has on the folding of the riboswitch. In the presence of 1 mM Mg^{2+}, addition of 0.1 mM Mn^{2+} results in the appearance of a unique population of SD (~43%) traces residing in the high-FRET state for >30 s (k_{undock} < 0.03 s^{-1}) before photobleaching (Fig. 5a). Accordingly, the FRET histogram shows two peaks with mean FRET values of 0.17 ± 0.14 and 0.69 ± 0.12 and an increased ~68% population of the docked conformation (Fig. 5a). The SD population is evident in the TODP as a new on-diagonal contour centered on the ~0.7-FRET value (Fig. 5a). Double-exponential kinetics similar to the 1 mM Mg^{2+} alone condition are observed, with $k_{dock}^{fast} = 5.55\ s^{-1}$, $k_{dock}^{slow} = 0.46\ s^{-1}$, $k_{undock}^{fast} = 3.84\ s^{-1}$ and a ~5-fold slower k_{undock}^{slow} of 0.23 s^{-1}. Notably, in the presence of Mn^{2+}, most of the dynamic traces show DD character. These data demonstrate that Mn^{2+} binding stabilizes the docked conformation while uniquely enabling an SD state. FRET histograms further show that out of a variety of divalent metal ions tested, only Cd^{2+} is effective in promoting docked conformations over 1 mM Mg^{2+} alone; Ni^{2+}, Co^{2+}, Sr^{2+}, or Zn^{2+} had little effect (Fig. 5b and Supplementary Fig. 26). Interestingly, in the absence of Mg^{2+}, while 0.1 mM Mn^{2+} alone leads to the appearance of DD and SD traces with ~62% docked population (mean FRET 0.67 ± 0.12) (Fig. 5c), 0.1 mM of Ni^{2+}, Co^{2+}, Sr^{2+}, or Zn^{2+} does not affect SU traces and Cd^{2+} has only a small effect in promoting DD traces (Supplementary Note 6 and Supplementary Fig. 26). These results suggest that while the *Xory* riboswitch has some degree of plasticity in recognizing ligands in a background of Mg^{2+}, it preferentially recognizes Mn^{2+} and—to a lesser extent—Cd^{2+}.

To probe how the kinetically distinct SU, DU, and DD traces respond to Mn^{2+}, we observed the same set of molecules at 1 mM Mg^{2+}, before and after the addition of Mn^{2+}. We find that all three populations respond to Mn^{2+} and are capable of forming the stably docked (SD) population (Fig. 5d). In particular, the SU traces convert into DU, DD, and SD conformations with similar probabilities, suggesting that they are correctly folded with metal-sensing sites poised to bind ligand. By comparison, a majority of DD traces convert into SD traces, whereas DU traces adopt DD and SD behavior upon Mn^{2+} addition. Only a small fraction of traces show no response at low Mn^{2+} suggesting that they may be misfolded.

Mutation of A48 results in complete loss of SD conformation. The highly conserved discriminator base A48 in L3 is positioned to confer Mn^{2+} specificity via its N7 and also helps maintain L3 in a stacked conformation. We, therefore, tested the effect of a single A48U mutation on folding and Mn^{2+} sensing of the riboswitch. Similar to the WT, at 100 mM KCl without divalents, the mutant riboswitch shows SU population with a mean FRET value of 0.11 ± 0.12 (Fig. 6a). At 1 mM Mg^{2+}, we observe dynamic traces with excursions into the docked higher FRET states, and the FRET histogram shows a major (64%) 0.14 ± 0.11 low-FRET peak and a minor (36 %) broad 0.52 ± 0.21 mid-FRET peak that corresponds to more extended docked conformations (Fig. 6b). Of note, 100% of the dynamic mutant traces show DU character under this condition (Fig. 6b). As a result, we observe fast single-exponential kinetics with k_{undock} ~ 6.67 s^{-1}, while k_{dock} was double-exponential with a major $k_{dock}^{fast} = 3.70\ s^{-1}$ (95%) and a minor $k_{dock}^{slow} = 0.46\ s^{-1}$ (5%) (Supplementary Fig. 27). The TODPs show SU behavior in the absence of divalents, whereas both SU and DU behaviors are observed at 1 mM Mg^{2+} (Fig. 6a, b).

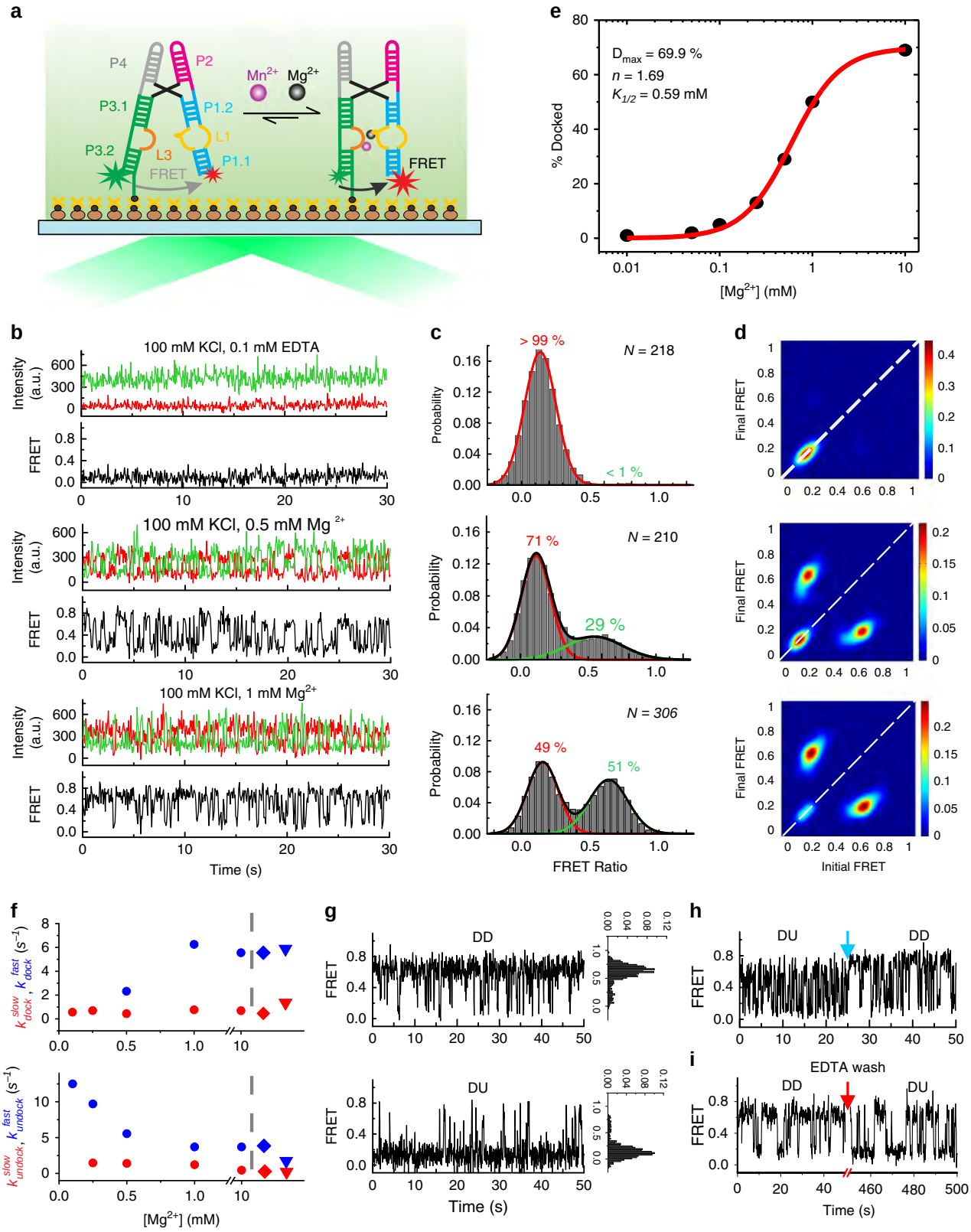

Next, we asked whether the mutant riboswitch can still respond to Mn^{2+}. In the presence of 1 mM Mg^{2+} and 0.1 mM Mn^{2+}, most smFRET traces show DD behavior, while only a small fraction remain in the SU state, similar to WT (Fig. 6c). FRET histograms show a similar ~0.14 ± 0.13 (57%) low-FRET undocked state but display a docked state now with a higher mean-FRET value of 0.63 ± 0.15 and a larger ~43% population, compared to the 1 mM Mg^{2+} only condition. The kinetics under these conditions are double-exponential with a $k_{dock}^{fast} = 6.67\ s^{-1}$ (89%), $k_{dock}^{slow} = 0.64\ s^{-1}$ (11%), $k_{undock}^{fast} = 3.10\ s^{-1}$ (94%), $k_{undock}^{slow} =$

Fig. 4 smFRET analysis of the WT *Xory* Mn^{2+} riboswitch. **a** Schematic of the smFRET experiment using TIRFM indicating the fluorophore labeling positions on the riboswitch. **b** Representative smFRET traces under different buffer conditions (top–bottom): no divalents (+0.1 mM EDTA), 0.5 mM Mg^{2+} and 1 mM Mg^{2+}, respectively. Green, Cy3; Red, Cy5; Black, FRET. **c** Population FRET histograms showing the equilibrium distribution of two FRET states under the conditions in panel (**b**). Gaussian peaks for the low- and high-FRET states are shown in red and green, respectively with the cumulative fit shown in black. Reported are the percentages of FRET states at equilibrium, as well as the number of molecules N analyzed. **d** TODPs showing the static and dynamic trances as "on-diagonal" and "off-diagonal" heat map contours, respectively. The color code indicates the fraction of each population. **e** Fraction of the high-FRET state as a function of Mg^{2+} concentration, fit with a standard Hill equation (red). **f** Kinetics of structural dynamics as a function of Mg^{2+} and Mn^{2+} concentration. The diamond symbols represent rates in 1 mM Mg^{2+} and 0.1 mM Mn^{2+} while the triangle symbols represent rates in 0.1 mM Mn^{2+} alone. **g** Exemplary dynamic docked (DD, top) and dynamic undocked (DU, bottom) traces in the presence of 1 mM Mg^{2+}. FRET histograms for the individual traces are shown on the right. **h** Rare examples of interconversion between different kinetic regimes showing dynamic heterogeneity. The blue arrow indicates the time of switching between the two kinetic regimes. **i** Exemplary trace showing conversion of a DU trace to DD trace upon chelation of Mg^{2+} with EDTA (indicated by the red arrow) and reintroducing 1 mM Mg^{2+}. Source data for panels (**e**) and (**f**) are provided as a Source Data file

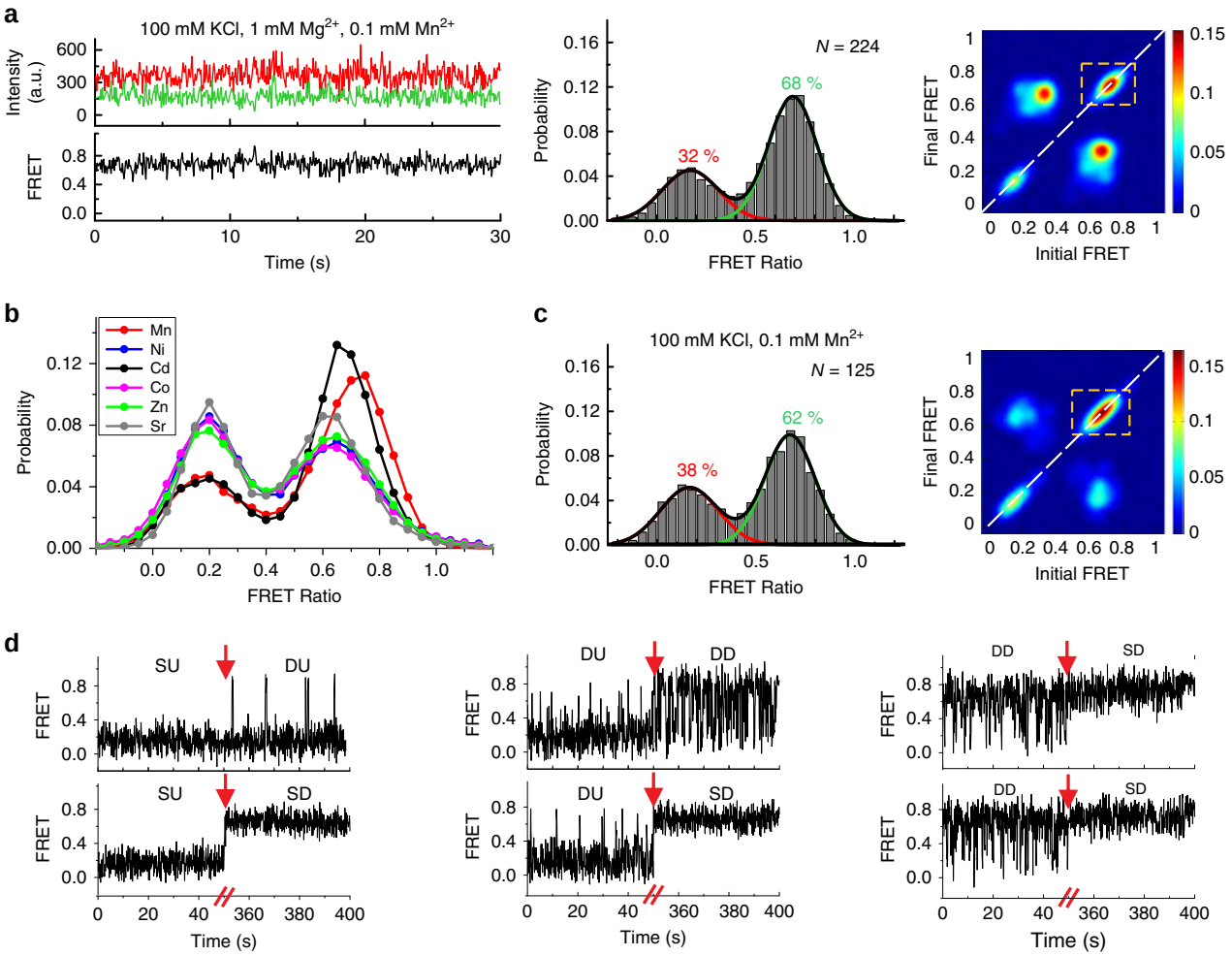

Fig. 5 Effect of Mn^{2+} on the folding of the riboswitch. **a** Representative smFRET trace, FRET histogram and TODP for the WT riboswitch in the presence of 0.1 mM Mn^{2+} and 1 mM Mg^{2+}. The stable docked (SD) conformation appears only in the presence of Mn^{2+}, as highlighted by the dashed yellow box in the TODP. **b** FRET histograms for the WT riboswitch at 0.1 mM concentration of different transition metals in the presence of 1 mM Mg^{2+}. Over 150 molecules were analyzed for each histogram. The corresponding TODPs are shown in Supplementary Fig. 26. **c** FRET histogram and TODP with SD population highlighted by dashed yellow box for the WT riboswitch in the presence of 0.1 mM Mn^{2+} alone. **d** Example smFRET traces for the WT riboswitch showing transitions between SU, DU, DD, and SD traces upon addition of 0.1 mM Mn^{2+}. The time of Mn^{2+} addition is indicated by the red arrow

$0.88\ s^{-1}$ (6%) (Supplementary Fig. 27). Importantly, the mutation causes a striking loss of SD traces, as evident from the complete absence of the on-diagonal ~0.7 FRET contour in the TODP (Fig. 6c), in stark contrast to the WT. In addition, the mutant interestingly loses the WT's ability to sample the docked conformations in the presence of 0.1 mM Mn^{2+} alone (Fig. 6d); almost all smFRET traces at 0.1 mM Mn^{2+} are in the SU conformation, with the histogram showing a major single peak around 0.19 ± 0.13 FRET, further corroborated by a single on-diagonal ~0.2 FRET contour in the TODP (Fig. 6d). These data demonstrate that the conserved discriminator A48 is essential for Mn^{2+} inducing a SD riboswitch conformation. The presence of Mg^{2+} partially rescues the loss of Mn^{2+} sensing by the mutant, yet does not restore its ability to form the SD conformation.

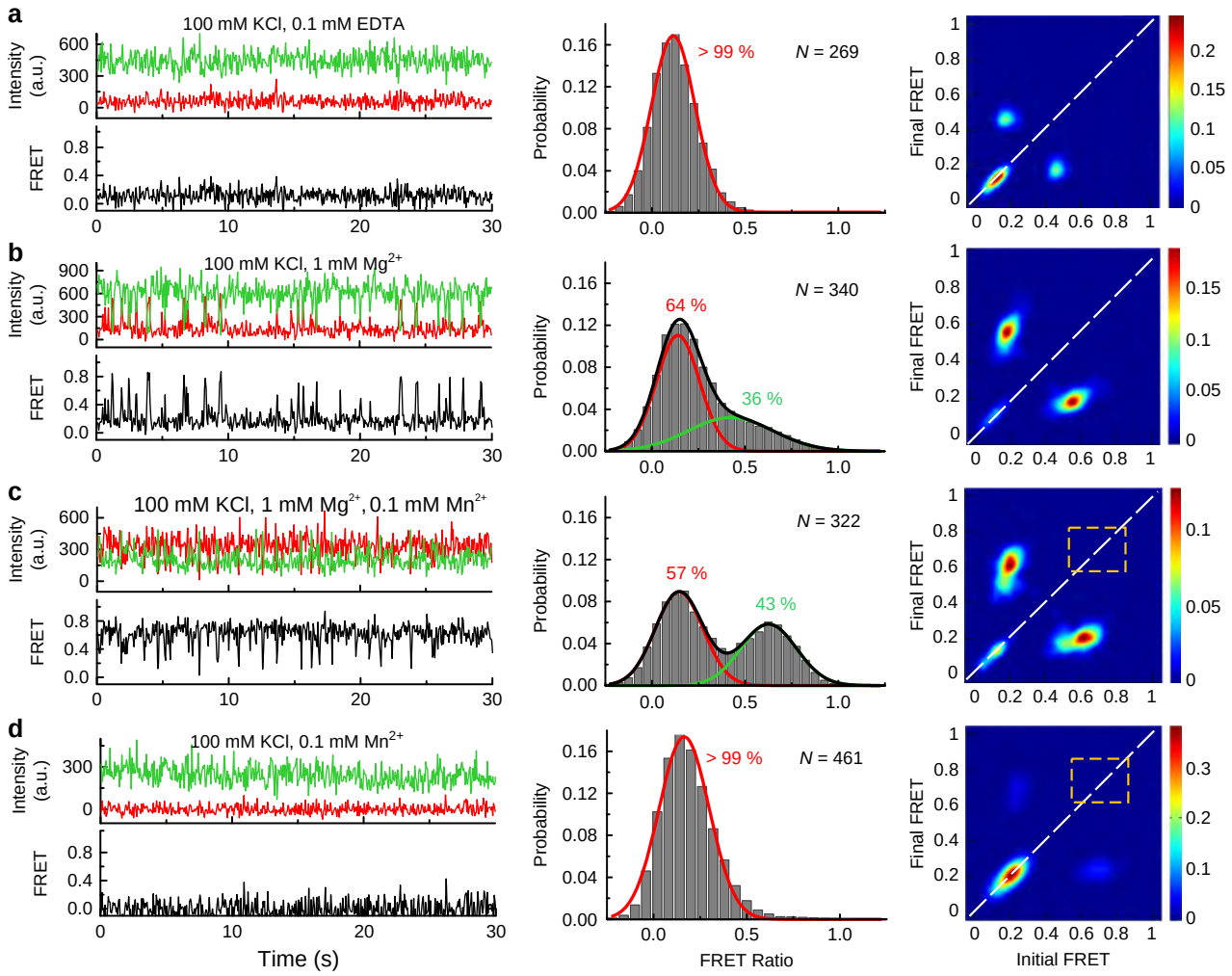

Fig. 6 Mutation of the Mn^{2+} sensing A48 leads to loss of the SD conformation. Representative smFRET traces, FRET histograms and TODPs for the A48U mutant riboswitch under: **a** no divalents (+0.1 mM EDTA), **b** 1 mM Mg^{2+} alone, **c** 1 mM Mg^{2+} and 0.1 mM Mn^{2+}, and **d** 0.1 mM Mn^{2+} alone. The dashed yellow box highlights the absence of SD conformations for the A48U riboswitch in the presence of Mn^{2+}, in contrast to the WT riboswitch

Possibly this reflects the ability of Mg^{2+} to bind at M_B in A48U, though with weaker affinity, via the uridine O4, as suggested in the A41U *L. lactis* structure[12].

Mn^{2+}-binding enhances the stability of switch helix P1.1. The proposed mechanism of transcription antitermination of the *yybP–ykoY* riboswitch, supported by our structural and dynamic data, involves Mn^{2+}-mediated stabilization of the inherently weak P1.1 switch helix. To more directly test this prevailing hypothesis, we probed the accessibility of the 3'-half of the P1.1 helix (last 12-nt) *in trans* by a complementary Cy5-labeled DNA oligonucleotide probe using our established single molecule kinetic analysis of RNA transient structure (SiM-KARTS) assay (Fig. 7a)[36]. In the current configuration, SiM-KARTS mimics the strand invasion by the downstream terminator sequence and reports on the stability of P1.1 helix at the single-molecule level. In the presence of 10 nM Cy5-labeled oligonucleotide and 1 mM Mg^{2+}, repeated short binding events are observed with a probe binding rate constant k_{on} of $9.67 \pm 1.24 \times 10^6\ M^{-1}\ s^{-1}$ and a dissociation rate constant k_{off} of $5.88 \pm 0.35\ s^{-1}$ for the WT riboswitch (Fig. 7b, c). Addition of increasing concentrations of Mn^{2+} results in a decrease in the frequency of binding events, with a k_{on} value significantly reduced by ~2.5-fold in the presence of 200 μM Mn^{2+} (Supplementary Figs. 28 and 29). These data report on a decreasing accessibility of the 3'-segment of the P1.1 helix and thus a more stable P1.1 duplex in the presence of Mn^{2+}. Interestingly, the k_{off} value also decreases with the addition of Mn^{2+}, consistent with the notion that the RNA can still sense Mn^{2+} via interaction of the free 5'-half of P1.1—extending into the L1 loop—with loop L3, resulting in a stable L1 and P1.2 that can stack on top of the RNA–DNA hybrid. Remarkably, the effect of Mn^{2+} is completely lost in the A48U mutant, where the k_{on} and k_{off} values remain essentially unchanged at $8.24 \pm 0.30 \times 10^6\ M^{-1}\ s^{-1}$ and $4.54 \pm 0.41\ s^{-1}$, respectively, even at high (500 μM) Mn^{2+} concentration, showing no change in the frequency of individual binding events (Fig. 7d, e and Supplementary Figs. 28 and 30). These data demonstrate that the stability of P1.1 is enhanced once the riboswitch encounters Mn^{2+}, an effect lost upon mutation of the Mn^{2+} sensing adenosine. These results thus provide a direct evidence for the prevailing mechanistic hypothesis of riboswitching by the *yybP–ykoY* RNA, wherein Mn^{2+} binding stabilizes the antiterminating P1.1 switch helix through long-range signal transduction from the metal ion sensing core, thereby preventing formation of the competing terminator hairpin.

Discussion

Using a combination of X-ray crystallography, MD simulations and smFRET, our work here sheds light on how the binding of a single Mn^{2+} ion at a distant site can modulate the stability of the

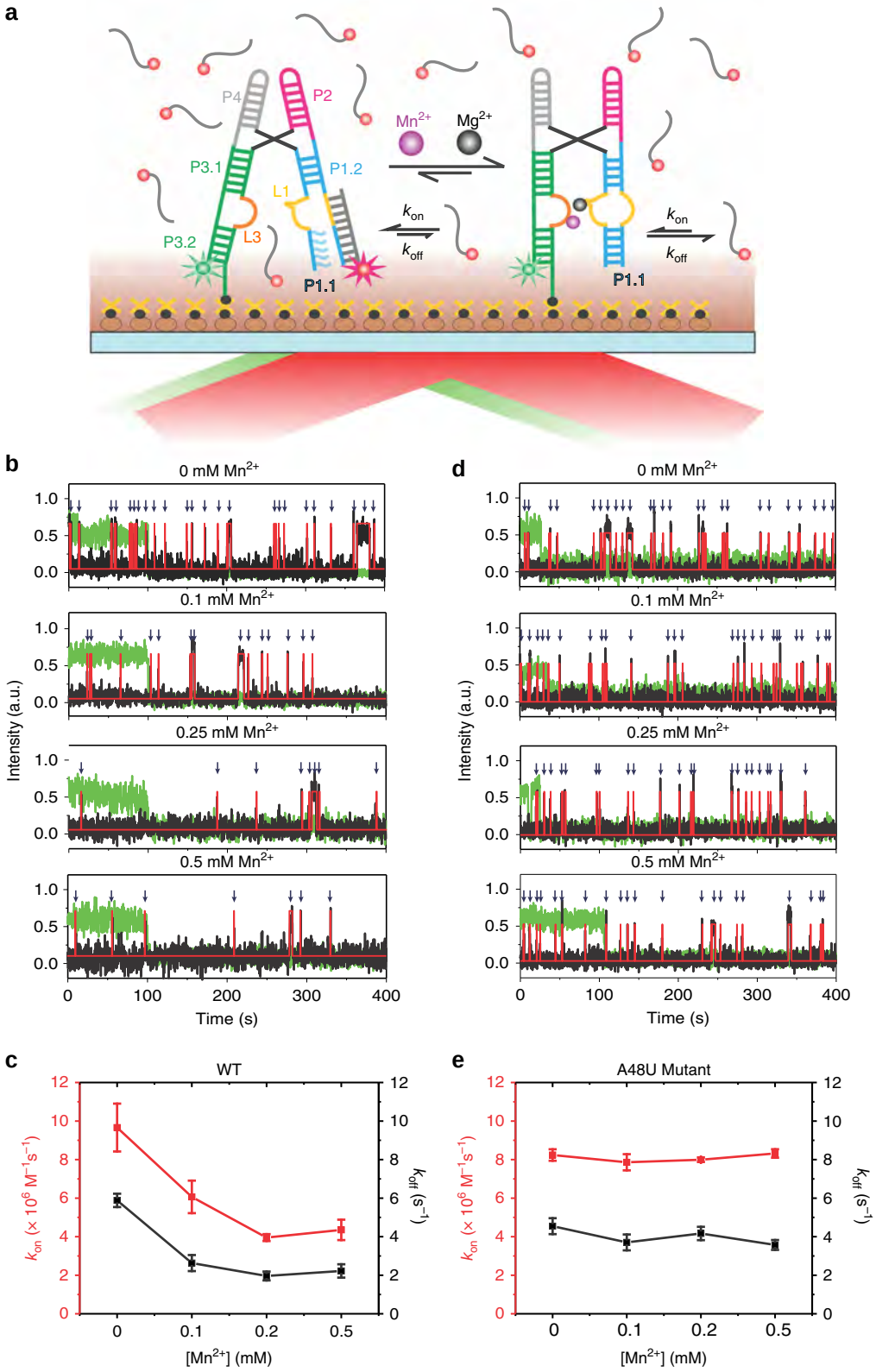

Fig. 7 Accessibility of switch helix P1.1 probed using a SiM-KARTS assay. **a** Schematic of our SiM-KARTS assay to probe the accessibility of switch helix P1.1 in the presence and absence of Mn^{2+}. **b** Representative SiM-KARTS traces at different Mn^{2+} concentrations show multiple binding events of the Cy5-labeled DNA oligonucleotide probe. Green, Cy3 intensity; black, Cy5 intensity; red, idealized Cy5 intensity fit to a two-state model. **c** The association (k_{on}, red) and dissociation (k_{off}, black) rate constants for binding of probe to P1.1 as a function of Mn^{2+} concentration for the WT riboswitch. The errors for the rate-constants are obtained using a boot-strapping program, as described in Methods. **d**, **e** Same as in (**b**) and (**c**), but for the A41U mutant riboswitch. Over 200 traces were analyzed for each condition to obtain reliable kinetic rate constants. The data for kinetic plots in (**c**) and (**e**) are provided in the Source Data file

switch helix through a conformational cascade that couples local with global structural dynamics. While previous structures revealed the local Mn^{2+} recognition mechanism of *yybP–ykoY* RNA[12,19], the structures reported here underscore the conformational plasticity around the metal ion binding core. Importantly, the structural differences observed between the two conformers in the crystal lead us to posit that Conformer 2 with L3 partially unfolded around $M_{B,Mn}$ is likely an intermediate between the fully Mn^{2+}-bound state and the empty $M_{B,Mn}$ state observed in the *E. coli* Mn^{2+}-free structures[12]. We hypothesize that the loss of phosphate contacts from C51, U52, and G9 to Mn^{2+} in Conformer 2 reflects their relative weakness as supported by MD simulations and likely represents a discrete step in Mn^{2+} binding/unbinding. Conversely, the variation in $M_{B,Mn}$ site coordination we observe could represent inherent flexibility at this site, allowing it to recognize Mn^{2+} even if the metal ion is not fully dehydrated. This flexibility is also seen in the recent Cd^{2+}-bound structures[19] (see Supplementary Discussion).

Our MD simulations show that the SRL-like motif in L1 is inherently unstable in the L1–L3 undocked state, but is stabilized by the tertiary A-minor interaction of A10 with P3.1. Similarly, L1–L3 docking stabilizes L3 in a stacked conformation by direct stacking of A10 on top of it. Thus, a stable conformation of L1 and therefore P1.1 is intimately linked to the stability of L3 and the tertiary A-minor interaction. We suggest that the SRL-like motif acts as a molecular switch that links the Mn^{2+}-dependent increase in docking observed by smFRET to stabilization of P1.1.

The observation of pairs of stably and dynamically docked and undocked states with double-exponential kinetics supports the existence of at least two undocked and docked dynamic (in addition to the static SU and SD) conformations, with similar FRET values and thus global folds, but likely different local conformations around the ligand sensing core. These conformations are possibly related to Conformers 1 and 2 in the crystal structure. We further find that SD conformations are formed only in the presence of submillimolar Mn^{2+} or the related soft transition metal ion Cd^{2+}, and lost upon a single mutation of the invariant Mn^{2+}-sensing adenine A48. While our work was in preparation, another smFRET study on the folding of a different *Llac* Mn^{2+} riboswitch became available. Using a similar labeling strategy, this *Llac* riboswitch showed two FRET states similar to the *Xory* riboswitch[37]. Interestingly, the kinetics of conformational dynamics for the *Llac* riboswitch were largely single-exponential, suggesting a two-state folding behavior, that agrees with a single conformation of the ligand-bound structure. This is in contrast to the *Xory* riboswitch studied here, which shows double-exponential kinetics, consistent with the two distinct conformations of the ligand-bound structure seen in our crystal structures. Such species-specific differences in the Mg^{2+} and Mn^{2+} mediated folding of the *yybP–ykoY* riboswitches likely enable bacteria to elicit a fine-tuned response to changes in their intracellular metal ion concentrations.

Our structural snapshots, MD simulations and smFRET data support the long-range structural signal transduction model shown in Fig. 8. In the absence of any divalent ions, the *Xory* riboswitch adopts an extended conformation in which the two legs are distal and rarely interact, as shown by smFRET. Under these conditions, the metal-ion binding sites are likely unstructured and their interaction only transiently formed by L1–L3 contacts, as suggested by rare smFRET transitions, MD simulations, as well as previous ligand-free structures[12]. MD simulations in particular show that the A-minor interaction formed by A10 of

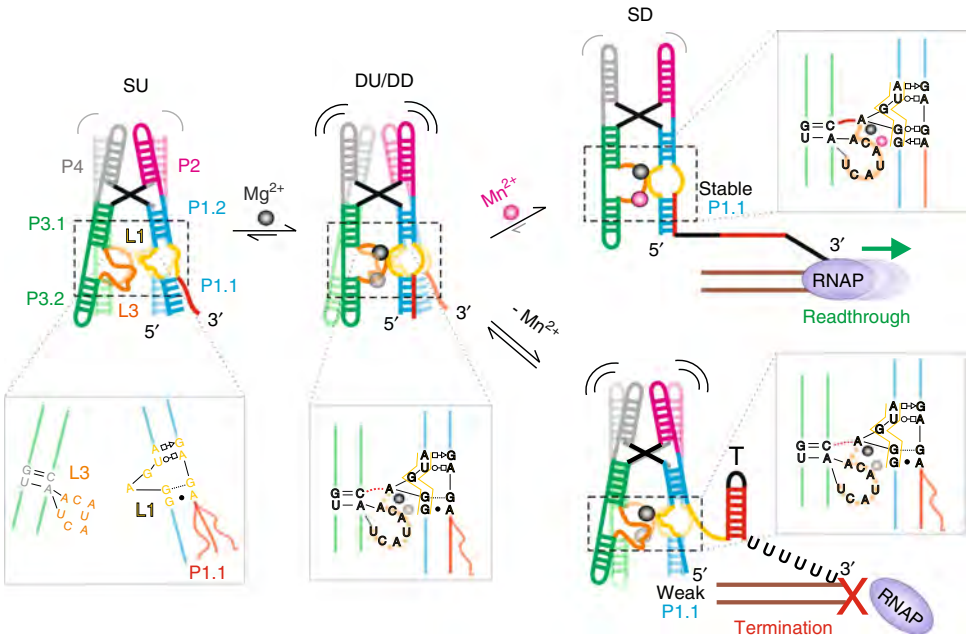

Fig. 8 Local-to-global signal transduction pathway in the core of the *Xory* Mn^{2+} sensing riboswitch. The *Xory* riboswitch exists in an "X-shaped" extended SU conformation in the absence of Mg^{2+}, with very rare transitions into docked "H-shaped" conformations. In the SU state, the legs are far apart in the absence of a stable A-minor tertiary interaction and loops L3 and L1 are less structured under these conditions. In the presence of physiological Mg^{2+} concentrations (mM), the riboswitch samples docked conformations with distinct kinetics, indicative of differences in L3 stacking as observed in our crystal structures. L1 adopts an S-turn conformation (as indicated by the yellow box in the inset) and L3 is partially stacked under these conditions, aided by the presence of Mg^{2+} ions in $M_{A,Mg}$ and transiently in $M_{B,Mn}$. In the presence of sufficient Mn^{2+}, binding of the metal ion by A48 reinforces L3 stacking and stability of the A-minor interaction. This maintains L1 in a rigid noncanonical SRL-like conformation that enables co-axial stacking between P1.2 and the switch helix P1.1. In turn, this cascade of interactions stabilizes P1.1, thereby preventing strand invasion to favor formation of the antiterminator required for transcriptional read-through

L1 loop with the G–C base pair of stem P3.1 can at least transiently form even in the absence of divalents. The formation of this A-minor interaction helps pre-organize the $M_{A,Mg}$ binding site. Under physiological (1 mM) concentrations of Mg^{2+}, this ion binds first at the $M_{A,Mg}$ site, allowing the riboswitch to sample dynamic folded conformations where the two legs are brought together via metal ion-mediated interaction between loops L1 and L3. These dynamic folded states then allow for local interactions mediated by L3, forming a pocket of high negative charge potential poised to sense Mn^{2+}. Mg^{2+} binding at $M_{A,Mg}$, therefore facilitates binding of Mn^{2+} at $M_{B,Mn}$ in cooperative fashion, as suggested by smFRET at the global level and further visualized by atomistic MD simulations. Capture of Mn^{2+} at site $M_{B,Mn}$ then acts as the final linchpin to hold the two legs together most stably. This compact docked conformation with a SRL-like fold of L1 and continuous coaxial stacking between P1.2, L1, and P1.1 stabilizes the remote P1.1 switch helix, as shown by our SiM-KARTS assay and MD simulations, that prevents the strand invasion required to form the terminator hairpin, instead promoting transcriptional read-through.

Contrasting with the Mn^{2+} riboswitch, the NiCo riboswitches, which cooperatively sense the transition metals Ni^{2+} or Co^{2+}, resemble the overall "H" shaped architecture of the Mn^{2+} riboswitch but with a tight 4WJ that lacks an analogous tertiary docking interface. Accordingly, the NiCo riboswitch appears to act through a distinct mechanism utilizing four bound metal ions to weave together a network of interactions between the interhelical residues that stabilize the 4WJ and so prevent formation of a terminator via strand invasion[38]. Similarly, the Mg^{2+} sensing M-box riboswitch adopts an architecture with three parallel coaxially stacked helices that are brought together by the binding of six Mg^{2+} ions, leading to formation of a terminator[39]. Therefore, both the NiCo and Mg^{2+} sensing riboswitches achieve gene regulation by employing multiple metal ions that directly interact with and stabilize the switch helix. In contrast, the Mn^{2+} riboswitch is unique in requiring only a single-metal ion that does not make any direct contacts with switch helix P1.1. By combining high-resolution structural information with insights into both atomistic and global dynamics, our study outlines the mechanism by which a ligand as small as a single divalent metal ion couples local with global structure to give Mn^{2+} the ability to influence RNA folding and fine-tune gene expression by cooperating with a high background of Mg^{2+}. The general lessons revealed here of how a ligand-binding signal can be transduced across an RNA are likely to become a recurring theme among riboswitches where the ligand represents a distal structural linchpin for the switch helix.

Methods

RNA preparation and crystallization. RNA was cloned, transcribed, purified, refolded with 2.5 mM Mn^{2+}, and screened for crystallization as previously described[12]. The *X. oryzae* aptamer domain sequence was modified to improve the chances of crystallization, including replacing the terminal loops in variable regions with GAAA tetraloops and adding a GG at the beginning of the sequence to increase T7 RNA polymerase efficiency[40]. We also removed a single unconserved U flip-out near the base of P1.1. In this construct, a native CA dinucleotide at the four-way junction was omitted from the sequence (Fig. 1a), possibly aiding crystallization. Initial crystal hits were obtained using the Nucleic Acid Mini-Screen (Hampton Research). This RNA crystallized at 0.2 mM in 10% MPD, 40 mM Na cacodylate (pH 7), 12 mM spermine tetrahydrochloride, 80 mM $SrCl_2$, and 20 mM $MgCl_2$ after 2–3 months at 18 °C.

X-ray data collection and structure building. A 2.96 Å resolution X-ray diffraction dataset was collected at NE-CAT beamline 24-ID-C at the Advanced Photon Source (Argonne, IL), at 0.769 Å wavelength in order to use the Strontium K-edge for phasing. An additional dataset was collected at a remote wavelength (0.7749 Å) for SIRAS. Datasets were processed by XDS[41] as part of NE-CAT's RAPD pipeline. An initial solution was achieved by molecular replacement using the central region of the *L. lactis* structure[12] followed by finding portions of external helices[42]. This partial solution was then used for MR-SAD in AutoSol in the Phenix suite[43,44] to find Sr sites and obtain an initial electron density map. Since this dataset was collected near the Sr K-edge wavelength (0.769 Å), we could observe anomalous signal from Sr^{2+} ions in the crystal. At 4σ (a relatively low threshold), there was modest signal at the Conformer 2 $M_{A,Mg}$ site, suggesting only partial occupancy by Sr^{2+} (Fig. 2b). However, there is no occupancy seen at any of the other $M_{A,Mg}$ or $M_{B,Mn}$ sites, despite there being external sites in the lattice with stronger anomalous signal (Supplementary Fig. 1). This suggests that the Conformer 2 $M_{B,Mn}$ site, despite lacking several contacts, can still distinguish between metals. It possibly discriminates by geometry; the Sr^{2+} ionic radius is 2.4 Å, compared to the smaller Mn^{2+} (2.2 Å) or Mg^{2+} (2.1 Å). Mg^{2+} cannot be differentiated from Mn^{2+} at the wavelength and resolution of this structure. Alternating rounds of building in Coot[45] and refinement with phenix.refine[46] and intermittent re-phasing and density modification in AutoSol were used to build the final model (Table 1).

Molecular dynamics simulations. The crystal structures of yybP-ykoY riboswitch from *X. oryzae* from this study (both Conformers 1 and 2) and from *L. lactis* (PDB ID 4Y1I[12] and PDB ID 6CB3[19]) were used as starting structures for MD simulations.

We aimed to study the effect of divalents in the metal ion binding sites on the structural dynamics of the riboswitch, so we prepared a set of starting structures containing different ions (Mn^{2+}, Mg^{2+}, and K^+) in the $M_{A,Mg}$ and $M_{B,Mn}$ sites (in case of the 6CB3 structure chain A, we considered also the ion in the third M_C ion binding site reported in this structure, see Supplementary Table 1). In addition, we probed both for syn- and anti-conformations of A48 in Conformer 2 from *Xory* to verify refinement of the corresponding electron density as a *syn*-oriented nucleotide. Starting structures of the SRL-like motif lacking tertiary interactions with the rest of the aptamer were prepared from the crystal structures but entailing only the P1.1, P1.2, and L1 segments without divalents.

All MD simulations were carried out using pmemd.cuda (GPU code of AMBER 14 program package)[47,48] with the ff99bsc0χ_{OL3} force field[49–51]. The simulation protocol was as follows. The structure with the RNA molecule and any ions in the $M_{A,Mg}$ and $M_{B,Mn}$ (and in case of 6CB3 chain A even the M_C) sites was immersed into a solvation box of SPC/E explicit water molecules[52]. We added KCl salt excess corresponding to 150 mM KCl. We used following ionic parameters: K^+ ($r = 1.593$ Å, $\varepsilon = 0.4297$ kcal/mol[53]), Mg^{2+} ($r = 1.5545$ Å, $\varepsilon = 0.00295$ kcal/mol[54]), Mn^{2+} ($r = 1.4060$ Å, $\varepsilon = 0.0167$ kcal/mol[55]), and Cl^- ($r = 2.711$ Å, $\varepsilon = 0.0127$ kcal/mol[53]). Where indicated, we replaced one or both divalent ions in the $M_{A,Mg}$ and $M_{B,Mn}$ sites by K^+ monovalents so that we probed for each specific starting structure four different ionic configurations in these ion binding sites (Supplementary Table 1). In the case of 6CB3 *L. lactis* structures we replaced the Cd^{2+} ions in the $M_{A,Mg}$, $M_{B,Mn}$, or M_C sites with K^+ monovalents or Mg^{2+} and Mn^{2+} divalents in similar manner (Supplementary Table 1). The solvated systems were equilibrated as follows. Geometrical optimization of hydrogen atoms was followed by optimization of waters and ions, while the position of the RNA molecule remained restrained. Subsequently, all RNA atoms were restrained and the solvent molecules with counter-ions were allowed to move during a 500-ps long MD run under NpT conditions ($p = 1$ atm, $T = 298.16$ K) to relax the total density of solvent surrounding the RNA. Next, the RNA molecule was relaxed by several minimization runs, with decreasing force constant of position restraints applied to the sugar-phosphate backbone. After full relaxation, the system was heated in two steps: The first step involved heating under NVT conditions for 100 ps, whereas the second step involved final density equilibration under NpT conditions for an additional 100 ps. The particle-Mesh Ewald method for treating electrostatic interactions was used, and simulation were performed under periodic boundary conditions in the NVT ensemble at 298.16 K using a weak coupling Berendsen thermostat with a coupling time of 0.2 ps. The SHAKE algorithm, with a tolerance of 10^{-5} Å, was used to fix the positions of all hydrogen atoms, and a 10.0 Å cut-off was applied to nonbonding interactions. The hydrogen mass repartitioning was used to change the mass of hydrogen and neighboring atoms to allow a 4 fs integration step. In the production runs of the isolated SRL-like motif (P1.2, L1, and P1.1 segments only) we applied upper-wall positional restraints to the hydrogen bonds of the terminal base pair of the P1.2 stem (i.e., the G16 = C89 base pair proximal to the P2 stem in the complete structure) to mimic the stabilization effect of coaxial stacking of this base pair on the P2 stem. A parabolic restraint potential was applied at heavy atom distances of the particular hydrogen bonds above 3.5 Å with a force constant of 2.5 kcal/mol/Å^2. The simulation time for each studied system was at least 2 µs (Supplementary Table 1).

Data analysis. All trajectories were analyzed with the Ptraj module of the AMBER package[48] and the simulations were visualized using VMD[56]. B-factors were calculated as average mass-weighted fluctuation of each residue over the entire trajectory aligned to the stem closest to the residue. This guarantees that the B-factors are not influenced by global motions and reflect local flexibilities only. The stacking interactions were detected using the G-vector of an eRMSD metric and were annotated using baRNAba[57].

RNA preparation for single-molecule FRET. The RNA for smFRET studies was annealed from two synthetic RNA oligonucleotides (Supplementary Fig. 23), ordered with the indicated modifications from IDT. The native CA dinucleotide omitted for crystallization was present in the smFRET RNA. Oligonucleotide 1 has a 5'-Cy5 and oligonucleotide 2 has 5'-Cy3 and 3' biotin-TEG. In this two-oligonucleotide design of the smFRET construct, the donor fluorophore Cy3 and biotin-TEG were placed on the 5' and 3' ends of stem P1.1 while the acceptor fluorophore Cy5 is attached to the 5' end of P3.2, positioning the fluorophores on either end of the distal arms that dock. For specifically probing the docking interaction, we extended the stem P1.1 to prevent end fraying. The biotin on the 3'-end of P1.1 was used for immobilization of the RNA onto a microscope quartz slide and subsequent prism-based total internal reflection fluorescence (TIRF) microscopy (Fig. 4a). Optimal refolding of the RNA was achieved with a mixture of 1 μM oligonucleotide 1 and 1.5 μM oligonucleotide 2 in 20 mM HEPES pH 7.0, 50 mM KCl. In PCR tubes, samples were heated to 70 °C for 2 min, then 2 mM $MgCl_2$ was added, samples were allowed to cool to RT for 10 min, then put on ice until further use. To check assembly, ~1 pmol of each oligonucleotide (1–2 μL) was added to 10 μL running buffer supplemented with 10% glycerol and loaded onto a non-denaturing 8% polyacrylamide gel run at 4 °C. A buffer of 0.5× TBE supplemented with 2 mM $Mg(OAc)_2$ and 50 mM KCl was used in the gel and as the running buffer.

smFRET data acquisition and analysis. A small microfluidic channel was made by sandwiching a cleaned quartz slide and a glass coverslip using double-side tape. Beforehand, two holes were drilled into the quartz slide and afterwards tubing was attached to them to act as inlet and outlet ports that were used for flowing buffer and introducing the RNA. The two RNA oligonucleotides containing the Cy3, Cy5 and biotin modifications were mixed at a concentration of 2 μM each in 50 mM HEPES, pH 7.2, 100 mM KCl (1× buffer). The RNA was heated at 90 °C for 2 min, left at RT for 30 s to cool down, followed by addition of 2 mM $MgCl_2$ and slow cooling down to RT over 15 min. This annealed RNA stock was used for carrying out smFRET experiments, for which a 15–25 pM RNA solution was made by diluting the 2 μM annealed stock using 1× buffer.

Totally, 100 μL of diluted RNA solution was flowed onto the quartz slide coated with biotinylated-bovine serum albumin and streptavidin for immobilization and incubated for 2 min. Any unbound RNA was washed off using 1× buffer. This step also washes off small (low nM) amounts of residual Mg^{2+} present in the stock. For experiments in the absence of divalents, 0.1 mM EDTA was included in the 1× buffer to chelate any contaminating divalent ions. Mg^{2+} titration experiments were performed on the same slide after washing off the EDTA using 1× buffer. We included an enzymatic oxygen scavenging system (OSS) containing 50 nM protocatechuate-3,4-dioxygenase and 5 mM protocatechuic acid in 1× buffer to prolong the longevity of the fluorophores. In addition, 2 mM Trolox (6-Hydroxy-2,5,7,8-tetramethylchromane-2-carboxylic acid) was included in the imaging buffer to suppress photoblinking of the dyes.

All smFRET movies were acquired at ~16 Hz, unless otherwise specified, using a prism-based TIRF microscope with an intensified CCD (I-Pentamax, Princeton Instruments) or sCMOS camera (Hamamatsu ORCA-Flash4.0 V3), essentially as previously described[58,59]. Cy3 on the RNA was excited using a 532 nm laser and the emission from both Cy3 (donor) and Cy5 (acceptor) were simultaneously detected side-by-side on the camera. Toward the end of all movies, the Cy5 was directly excited using a 640 nm laser to check for the presence of the acceptor (Cy5) fluorophore. This helps in distinguishing the low-FRET (~0.1 FRET) states we observe from ~0 FRET states due to the absence or photobleaching of Cy5 in Cy3-labeled molecules. Raw movies were analyzed using IDL (Research Systems) to extract the time traces for all spots in Cy3 and Cy5 channels. Single molecule traces were then visualized using Matlab and only those with a minimum combined intensity (Cy3 + Cy5 intensity) of 300, showing single-step photobleaching of the dyes, a signal-to-noise ratio of >3, and longer than 6 s were selected for further analysis. Selected traces were then background-subtracted to correct for cross-talk and (minimal) bleed-through. We calculated the FRET ratio as $I_A/(I_A + I_D)$, where I_A and I_D are the background corrected intensities of acceptor (Cy5) and donor (Cy3), respectively. FRET histograms were made using the first 50 frames (3 s) of all traces (at least 200) in a given condition and fit with a sum of Gaussians using OriginPro 8.5. For kinetic analysis, traces were idealized with a two-state model corresponding to undocked (low-FRET) and docked (high-FRET) states using the segmental k-means algorithm in QuB software as previously described[26,60]. Cumulative dwell-time histograms were plotted from all extracted dwell times and fit with single- or double-exponential functions using OriginPro 8.5 to obtain the lifetimes in the undocked (τ_{undock}) and docked (τ_{dock}) states. Rate constants of docking and undocking were then calculated as $k_{dock} = 1/\tau_{undock}$ and $k_{undock} = 1/\tau_{dock}$. For the double-exponential fits, kinetics were calculated similarly using both the short and long dwell lifetimes to obtain the fast and slow rate constants, respectively. The idealized smFRET traces were used for creating TODPs, which show the fraction of traces/molecules that exhibit a given type of transition at least once[26]. In TODPs, dynamic traces showing a FRET transition (regardless of the number of transitions in that trace) and static traces (with no transitions over the entire trace) are weighted equally, avoiding over-representation of the traces with fast transitions. This feature is distinct from traditional transition density plots that show all FRET transitions in a population as off-diagonal contours in the heat map, which leads to the visual dominance of rapid, frequent transitions. By contrast, TODPs are meant to show the fractions of different kinds of molecular behaviors and highlight slow or rare transitions found to be representing a large subpopulation of traces. In addition, the TODPs shown here also include static traces that appear as on-diagonal contours and are often critical in understanding the molecular mechanisms of riboswitches[61,62]. The on-diagonal contours in these TODPs (at ~0.2 and ~0.7 FRET values) thus do not represent any transitions, but rather highlight static traces that lack any FRET transitions over their entire observation length and are counted exactly once in the TODP heatmap.

SiM-KARTS assay. The SiM-KARTS assay to probe P1.1 accessibility was performed on a prism-based TIRF microscope[36]. Totally, 20 pM of the riboswitch was bound to the slide and the Cy5 on the riboswitch was first photobleached by excitation with a red laser. Kinetic measurements of P1.1 accessibility was performed in the presence of 10 nM of a Cy5-labeled DNA oligonucleotide and under varying concentrations of the metal ions in the 1× buffer with OSS also used for smFRET. The 5' Cy5-labeled DNA oligonucleotide is complementary to the 12-nt sequence (5'-GAGACCAGGGAU-3') of the 3'-half of L1 and P1.1 in the smFRET RNA construct (Supplementary Fig. 23). Movies were acquired at 100 ms time resolution under dual excitation with both a green and red laser to localize the Cy3-labeled surface-bound riboswitch molecules and to image the short binding events of the Cy5-labeled oligonucleotide probe, respectively. The Cy5 versus intensity time traces were idealized to a two-state model using the segmental *k*-means algorithm implemented in QuB to obtain the bound and unbound dwell times. The unbound and bound lifetimes were obtained by single-exponential fits to the cumulative dwell time distributions, the inverse of which gives the rate constants k_{on} and k_{off}, respectively. The errors of the rate constants were estimated using a bootstrapping algorithm by taking three random subsets from all the traces in a condition and calculating the rate constants. The means and standard deviations from the three calculated rates are reported in Fig. 7.

Reporting summary. Further information on research design is available in the Nature Research Reporting Summary linked to this article.

Data availability

A reporting summary for this Article is available as a Supplementary Information file. Atomic coordinates and structure factors for the reported crystal structure have been deposited with the Protein Data Bank under accession number 6N2V. The source data underlying Figs. 4e, h and 7c, e are provided as a Source Data file. The data supporting the findings of this study are available from the corresponding authors upon reasonable request.

Code availability

Custom scripts used to analyze the smFRET and MD simulations data can be made available upon request.

Received: 30 April 2019 Accepted: 28 August 2019
Published online: 20 September 2019

References

1. Mandal, M. & Breaker, R. R. Gene regulation by riboswitches. *Nat. Rev. Mol. Cell Biol.* **5**, 451–463 (2004).
2. Serganov, A. & Nudler, E. A decade of riboswitches. *Cell* **152**, 17–24 (2013).
3. McCown, P. J., Corbino, K. A., Stav, S., Sherlock, M. E. & Breaker, R. R. Riboswitch diversity and distribution. *RNA* **23**, 995–1011 (2017).
4. Grundy, F. J. & Henkin, T. M. The S box regulon: a new global transcription termination control system for methionine and cysteine biosynthesis genes in Gram-positive bacteria. *Mol. Microbiol* **30**, 737–749 (1998).
5. Winkler, W., Nahvi, A. & Breaker, R. R. Thiamine derivatives bind messenger RNAs directly to regulate bacterial gene expression. *Nature* **419**, 952–956 (2002).
6. Smith, K. D. et al. Structural basis of ligand binding by a c-di-GMP riboswitch. *Nat. Struct. Mol. Biol.* **16**, 1218–1223 (2009).
7. Nelson, J. W. et al. Riboswitches in eubacteria sense the second messenger c-di-AMP. *Nat. Chem. Biol.* **9**, 834–839 (2013).
8. Sudarsan, N. et al. Riboswitches in eubacteria sense the second messenger cyclic Di-GMP. *Science* **321**, 411–413 (2008).
9. Green, N. J., Grundy, F. J. & Henkin, T. M. The T box mechanism: tRNA as a regulatory molecule. *FEBS Lett.* **584**, 318–324 (2010).
10. Dann, C. E. III et al. Structure and mechanism of a metal-sensing regulatory RNA. *Cell* **130**, 878–892 (2007).

11. Wedekind, J. E., Dutta, D., Belashov, I. A. & Jenkins, J. L. Metalloriboswitches: RNA-based inorganic ion sensors that regulate genes. *J. Biol. Chem.* **292**, 9441–9450 (2017).
12. Price, I. R., Gaballa, A., Ding, F., Helmann, J. D. & Ke, A. Mn(2+)-sensing mechanisms of yybP-ykoY orphan riboswitches. *Mol. Cell* **57**, 1110–1123 (2015).
13. Suddala, K. C. & Walter, N. G. Riboswitch structure and dynamics by smFRET microscopy. *Methods Enzymol.* **549**, 343–373 (2014).
14. Jones, C. P. & Ferre-D'Amare, A. R. Long-range interactions in riboswitch control of gene expression. *Annu Rev. Biophys.* **46**, 455–481 (2017).
15. Barrick, J. C. K., Winkler, W. C., Nahvi, A., Mandal, M., Collins, J., Lee, M., Roth, A., Sudarsan, N., Jona, I., Wickiser, J. K. & Breaker, R. R. New RNA motifs suggest an expanded scope for riboswitches in bacterial genetic control. *Proc. Natl Acad. Sci. USA* **101**, 6421–6426 (2004).
16. Argaman, L. et al. Novel small RNA-encoding genes in the intergenic regions of *Escherichia coli*. *Curr. Biol.* **11**, 941–950 (2001).
17. Breaker, R.R. Riboswitches and the RNA world. *Cold Spring Harb. Perspect. Biol.* **4**, a003566 (2012).
18. Dambach, M. et al. The ubiquitous yybP-ykoY riboswitch is a manganese-responsive regulatory element. *Mol. Cell* **57**, 1099–1109 (2015).
19. Bachas, S. T. & Ferre-D'Amare, A. R. Convergent use of heptacoordination for cation selectivity by RNA and protein metalloregulators. *Cell Chem. Biol.* **25**, 962–973, e5 (2018).
20. Liang, H. et al. Identification and functional characterization of small non-coding RNAs in *Xanthomonas oryzae* pathovar oryzae. *BMC Genomics* **12**, 87 (2011).
21. Li, C., Tao, J., Mao, D. & He, C. A novel manganese efflux system, YebN, is required for virulence by *Xanthomonas oryzae* pv. oryzae. *PLoS One* **6**, e21983 (2011).
22. Sponer, J. et al. RNA structural dynamics as captured by molecular simulations: a comprehensive overview. *Chem. Rev.* **118**, 4177–4338 (2018).
23. Ditzler, M. A., Otyepka, M., Sponer, J. & Walter, N. G. Molecular dynamics and quantum mechanics of RNA: conformational and chemical change we can believe. *Acc. Chem. Res.* **43**, 40–47 (2010).
24. Leontis, N. B., Stombaugh, J. & Westhof, E. The non-Watson-Crick base pairs and their associated isostericity matrices. *Nucleic Acids Res.* **30**, 3497–3531 (2002).
25. Duarte, C. M., Wadley, L. M. & Pyle, A. M. RNA structure comparison, motif search and discovery using a reduced representation of RNA conformational space. *Nucleic Acids Res.* **31**, 4755–4761 (2003).
26. Blanco, M. & Walter, N. G. Analysis of complex single-molecule FRET time trajectories. *Methods Enzymol.* **472**, 153–178 (2010).
27. Zhuang, X. et al. Correlating structural dynamics and function in single ribozyme molecules. *Science* **296**, 1473–1476 (2002).
28. Rueda, D. et al. Single-molecule enzymology of RNA: essential functional groups impact catalysis from a distance. *Proc. Ntl. Acad. Sci. USA* **101**, 10066–10071 (2004).
29. Okumus, B., Wilson, T. J., Lilley, D. M. & Ha, T. Vesicle encapsulation studies reveal that single molecule ribozyme heterogeneities are intrinsic. *Biophys. J.* **87**, 2798–2806 (2004).
30. Ditzler, M. A., Rueda, D., Mo, J., Hakansson, K. & Walter, N. G. A rugged free energy landscape separates multiple functional RNA folds throughout denaturation. *Nucleic acids Res.* **36**, 7088–7099 (2008).
31. Fiore, J. L., Kraemer, B., Koberling, F., Edmann, R. & Nesbitt, D. J. Enthalpy-driven RNA folding: single-molecule thermodynamics of tetraloop-receptor tertiary interaction. *Biochemistry* **48**, 2550–2558 (2009).
32. Greenfeld, M., Solomatin, S. V. & Herschlag, D. Removal of covalent heterogeneity reveals simple folding behavior for P4-P6 RNA. *J. Biol. Chem.* **286**, 19872–19879 (2011).
33. Solomatin, S. V., Greenfeld, M. & Herschlag, D. Implications of molecular heterogeneity for the cooperativity of biological macromolecules. *Nat. Struct. Mol. Biol.* **18**, 732–734 (2011).
34. Solomatin, S. V., Greenfeld, M., Chu, S. & Herschlag, D. Multiple native states reveal persistent ruggedness of an RNA folding landscape. *Nature* **463**, 681–684 (2010).
35. Marek, M. S., Johnson-Buck, A. & Walter, N. G. The shape-shifting quasispecies of RNA: one sequence, many functional folds. *Phys. Chem. Chem. Phys.* **13**, 11524–11537 (2011).
36. Rinaldi, A. J., Lund, P. E., Blanco, M. R. & Walter, N. G. The Shine-Dalgarno sequence of riboswitch-regulated single mRNAs shows ligand-dependent accessibility bursts. *Nat. Commun.* **7**, 8976 (2016).
37. Sung, H. L. & Nesbitt, D. J. Single-molecule FRET kinetics of the Mn(2+) riboswitch: evidence for allosteric Mg(2+) control of "Induced-Fit" vs "Conformational Selection" folding pathways. *J. Phys. Chem. B* **123**, 2005–2015 (2019).
38. Furukawa, K. et al. Bacterial riboswitches cooperatively bind Ni(2+) or Co(2+) ions and control expression of heavy metal transporters. *Mol. Cell* **57**, 1088–1098 (2015).
39. Wakeman, C. A., Ramesh, A. & Winkler, W. C. Multiple metal-binding cores are required for metalloregulation by M-box riboswitch RNAs. *J. Mol. Biol.* **392**, 723–735 (2009).
40. Pleiss, J. A., Derrick, M. L. & Uhlenbeck, O. C. T7 RNA polymerase produces 5' end heterogeneity during in vitro transcription from certain templates. *RNA* **4**, 1313–1317 (1988).
41. Kabsch, W. XDS. *Acta Cryst.* **D66**, 125–132 (2010).
42. Robertson, M. P., Chi, Y.-I. & Scott, W. G. Solving novel RNA structures using only secondary structural fragments. *Methods* **52**, 168–172 (2010).
43. Adams, P. D. et al. PHENIX: a comprehensive Python-based system for macromolecular structure solution. *Acta Crystallogr. D Biol. Crystallogr.* **66**, 213–221 (2010).
44. Terwilliger, T. C. et al. Decision-making in structure solution using Bayesian estimates of map quality: the PHENIX AutoSol wizard. *Acta Crystallogr. D Biol. Crystallogr.* **65**, 582–601 (2009).
45. Emsley, P., Lohkamp, B., Scott, W. G. & Cowtan, K. Features and development of Coot. *Acta Crystallogr. D Biol. Crystallogr.* **66**, 486–501 (2010).
46. Afonine, P. V. et al. Towards automated crystallographic structure refinement with phenix.refine. *Acta Crystallogr. D Biol. Crystallogr.* **68**, 352–367 (2012).
47. Salomon-Ferrer, R., Gotz, A. W., Poole, D., Le Grand, S. & Walker, R. C. Routine microsecond molecular dynamics simulations with AMBER on GPUs. 2. Explicit solvent particle Mesh Ewald. *J. Chem. Theory Comput.* **9**, 3878–3888 (2013).
48. Case, D. A. et al. *AMBER 2016*. (University of California San Francisco, San Francisco, 2016).
49. Banáš, P. et al. Performance of molecular mechanics force fields For RNA simulations: stability of UUCG and GNRA hairpins. *J. Chem. Theory Comput.* **6**, 3836–3849 (2010).
50. Perez, A. et al. Refinement of the AMBER force field for nucleic acids: improving the description of alpha/gamma conformers. *Biophys. J.* **92**, 3817–3829 (2007).
51. Zgarbova, M. et al. Refinement of the Cornell et al. Nucleic acids force field based on reference quantum chemical calculations of glycosidic torsion profiles. *J. Chem. Theory Comput.* **7**, 2886–2902 (2011).
52. Berendsen, H. J. C., Grigera, J. R. & Straatsma, T. P. The missing term in effective pair potentials. *J. Phys. Chem.* **91**, 6269–6271 (1987).
53. Joung, I. S. & Cheatham, T. E. III Determination of alkali and halide monovalent ion parameters for use in explicitly solvated biomolecular simulations. *J. Phys. Chem. B* **112**, 9020–9041 (2008).
54. Allnér, O., Nilsson, L. & Villa, A. Magnesium ion–water coordination and exchange in biomolecular simulations. *J. Chem. Theory Comput.* **8**, 1493–1502 (2012).
55. Li, P., Roberts, B. P., Chakravorty, D. K. & Merz, K. M. Rational design of particle Mesh Ewald compatible Lennard-Jones parameters for +2 metal cations in explicit solvent. *J. Chem. Theory Comput.* **9**, 2733–2748 (2013).
56. Humphrey, W., Dalke, A. & Schulten, K. VMD: visual molecular dynamics. *J. Mol. Graph.* **14**, 33–38 (1996).
57. Bottaro, S., Di Palma, F. & Bussi, G. The role of nucleobase interactions in RNA structure and dynamics. *Nucleic Acids Res.* **42**, 13306–13314 (2014).
58. Michelotti, N., de Silva, C., Johnson-Buck, A. E., Manzo, A. J. & Walter, N. G. A bird's eye view tracking slow nanometer-scale movements of single molecular nano-assemblies. *Methods Enzymol.* **475**, 121–148 (2010).
59. Juette, M. F. et al. Single-molecule imaging of non-equilibrium molecular ensembles on the millisecond timescale. *Nat. Methods* **13**, 341–344 (2016).
60. Qin, F. & Li, L. Model-based fitting of single-channel dwell-time distributions. *Biophys. J.* **87**, 1657–1671 (2004).
61. Liberman, J.A. et al. Structural analysis of a class III preQ1 riboswitch reveals an aptamer distant from a ribosome-binding site regulated by fast dynamics. *Proc. Natl. Acad. Sci.* **112**, E3485–E3494 (2015).
62. Warhaut, S. et al. Ligand-modulated folding of the full-length adenine riboswitch probed by NMR and single-molecule FRET spectroscopy. *Nucleic Acids Res.* **45**, 5512–5522 (2017).

Acknowledgements

This work was supported by NIH R01 grants GM062357 and GM118524 to N.G.W., by NIH R35 grant GM118174 to A.K., by project SYMBIT reg. number CZ.02.1.01/0.0/0.0/15_003/0000477 funded by the ERDF (M.J. and J.S.), by grant 18-25349S (P.B. and P.K.) from the Grant Agency of the Czech Republic, and a student project of Palacky University Olomouc IGA_PrF_2019_031 (M.J.). We thank Qian Hou for help with some experiments. This work included research conducted at NE-CAT beamlines, which are funded by the National Institute of General Medical Sciences from the National Institutes of Health (P30 GM124165). The Pilatus 6M detector on 24-ID-C beam line is funded by a NIH-ORIP HEI grant (S10 RR029205). This research used resources of the Advanced Photon Source, a U.S. Department of Energy (DOE) Office of Science User Facility operated for the DOE Office of Science by Argonne National Laboratory under Contract No. DE-AC02-06CH11357.

Author contributions

K.C.S., I.R.P., S.S.D., A.K. and N.G.W. designed the experiments; P.B. and J.Š. designed the MD simulations; K.C.S. and S.S.D. performed the single-molecule experiments and analyzed the data; I.R.P. and A.K. performed the X-ray crystallography experiments and analyzed the data; M.J., P.K. and P.B. performed and analyzed the MD simulations; K.C.S., I.R.P., A.K., P.B. and N.G.W. wrote the bulk of the paper. All authors read and commented on the paper.

Additional information

Supplementary Information accompanies this paper at https://doi.org/10.1038/s41467-019-12230-5.

Competing interests: The authors declare no competing interests.

Reprints and permission information is available online at http://npg.nature.com/reprintsandpermissions/

Peer review information *Nature Communications* thanks Timothy Craggs, Garrett Soukup, and other anonymous reviewer(s) for their contribution to the peer review of this work. Peer reviewer reports are available.

Supplementary Information for

Local-to-global signal transduction at the core of a Mn^{2+} sensing riboswitch

Krishna C. Suddala[1]*, Ian R. Price[2]*, Shiba S. Dandpat[1], Michal Janeček[3,5], Petra Kührová[4,5], Jiří Šponer[3,4], Pavel Banáš[3,4,5], Ailong Ke[2], Nils G. Walter[1]

*These authors contributed equally

Correspondence and requests for materials should be addressed to A.K. (email: ailong.ke@cornell.edu) or to N.G.W. (email: nwalter@umich.edu)

Supplementary Figure 1

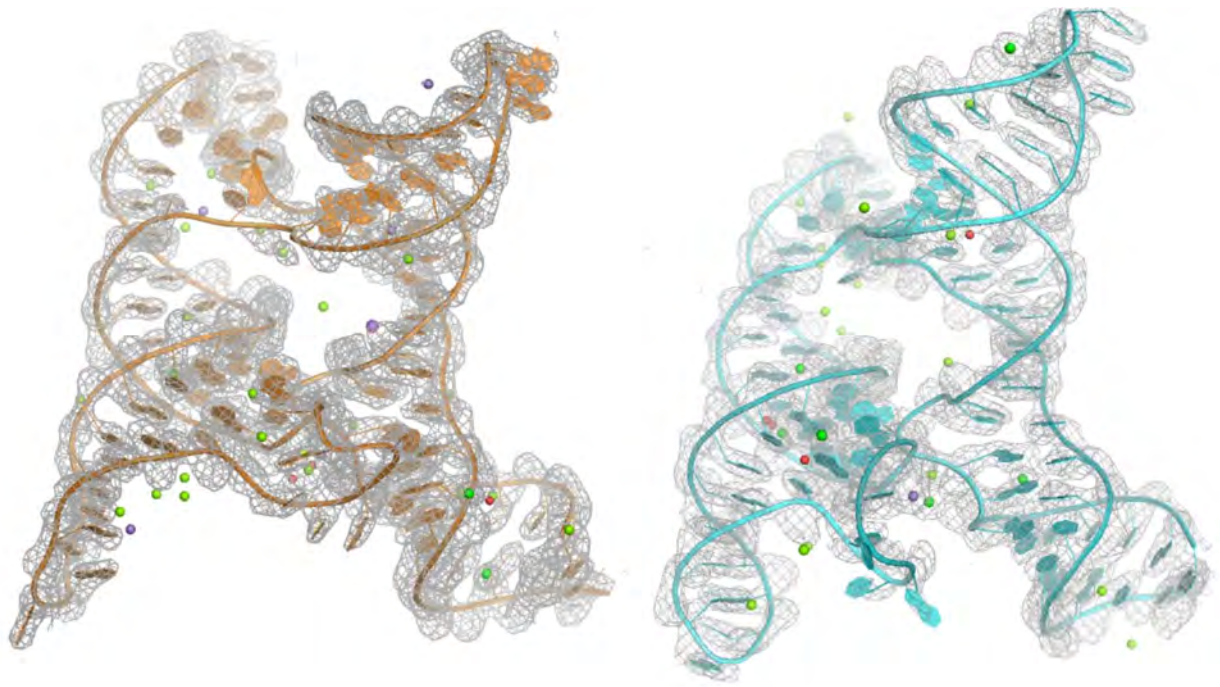

Supplementary Figure 1| *Xory* conformers 1 (orange) and 2 (cyan) with 2Fo-Fc electron density maps at the 1.5 sigma level.

.

Supplementary Figure 2

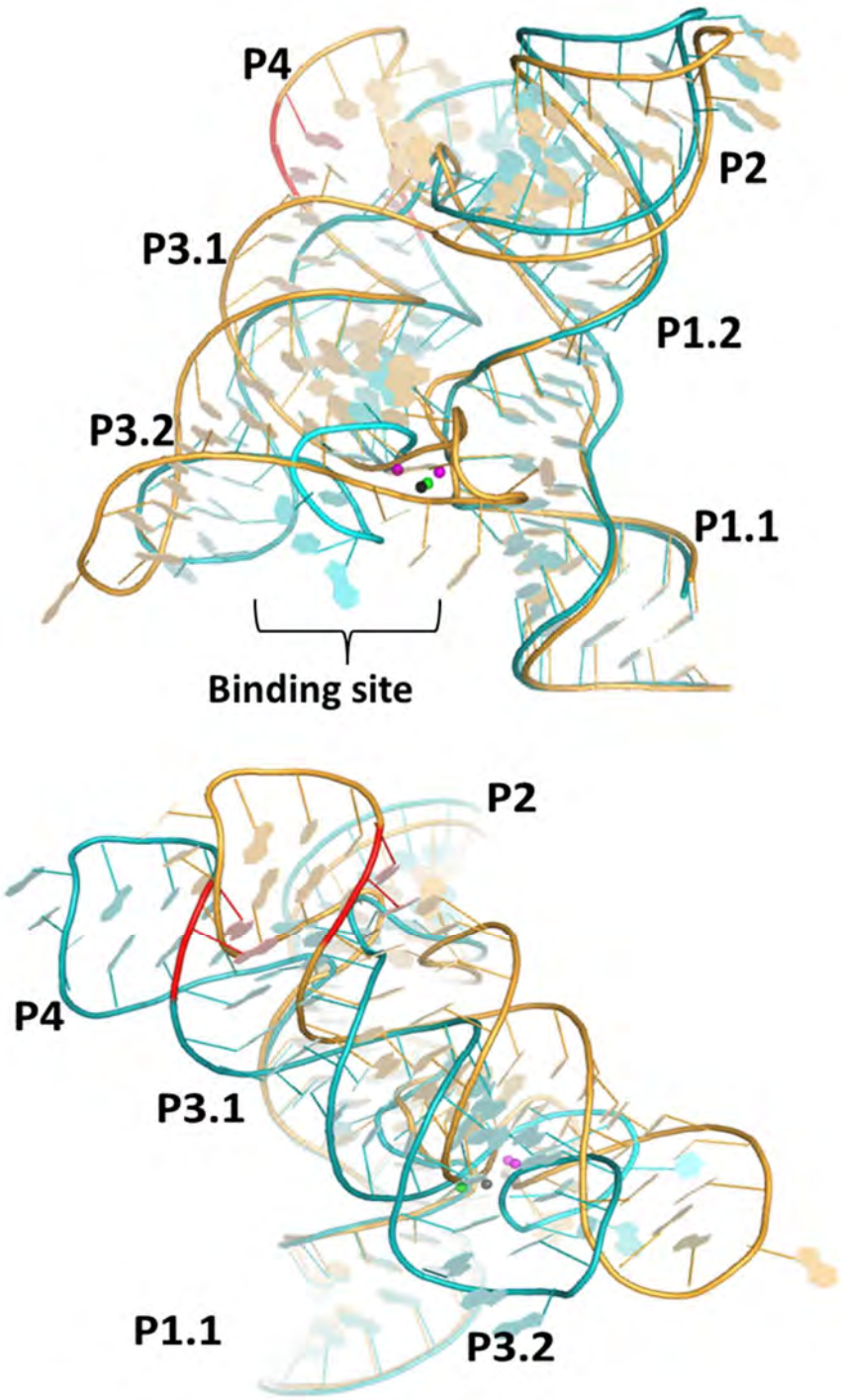

Supplementary Figure 2| Overall comparison of Conformers 1 and 2. When aligned by L1, there is also a shift of the P3/P4 helical stack between Conformers 1 (orange) and 2 (cyan). The *L. lactis* structure (not shown) is intermediate but more similar to Conformer 1 when aligned this way.

Supplementary Figure 3

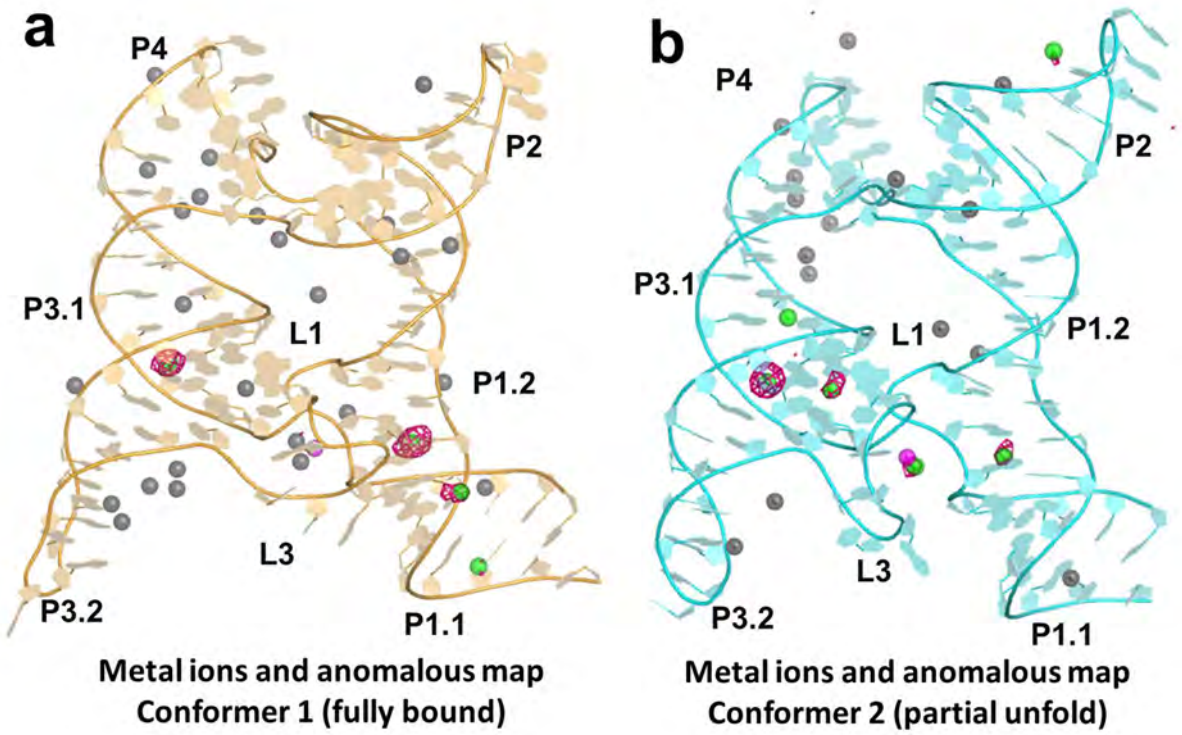

Supplementary Figure 3| Overall ions and anomalous sites for the *X. oryzae yybP-ykoY* riboswitch crystal construct. **a)** Conformer 1 (orange) and **b)** Conformer 2 (cyan). Total ions within 5 Å of A chain include 2 Mn^{2+} (magenta), 45 Mg^{2+} (or Mn^{2+}) (black), and 9 Sr^{2+} (green). The anomalous difference map, collected at 0.769 Å, is shown in pink mesh at level 4 σ. Placement of Sr^{2+} ions was determined by anomalous map and/or high electron density. Since Mn^{2+} has minimal anomalous signal at this wavelength and it is similar in ionic radius to Mg^{2+}, it could not be differentiated from Mg^{2+}. Thus, Mn^{2+} (2.5 mM in the crystal) could partially or fully occupy sites denoted as Mg^{2+} (30 mM in the crystal). Binding site Mn^{2+} were predicted to be so based on previous analysis of the *L. lactis* structure, but were not confirmed by this structure.

Supplementary Figure 4

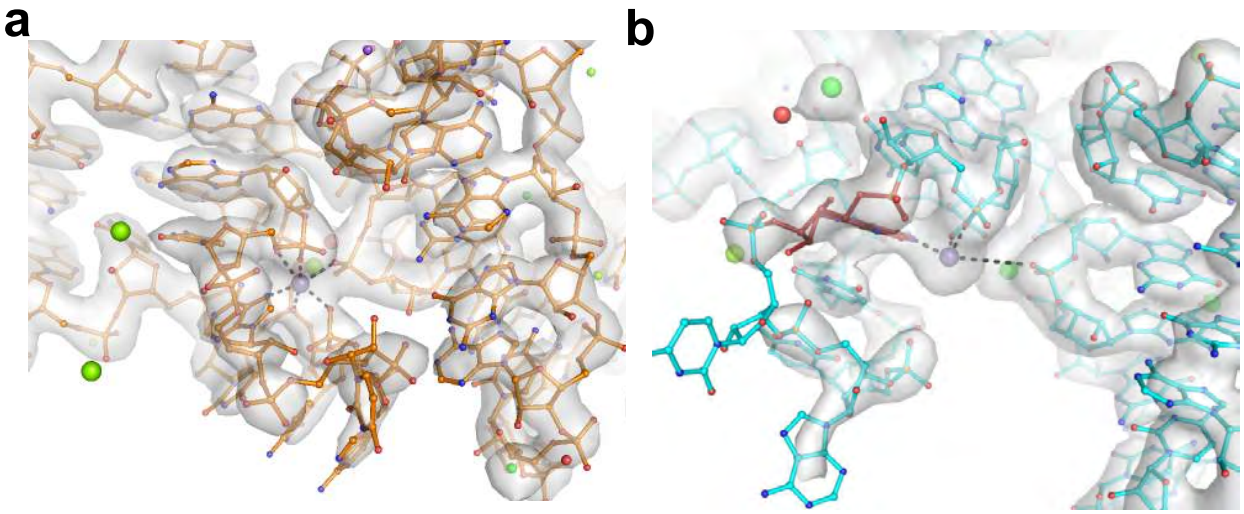

Supplementary Figure 4| $2F_o$-F_c electron density maps of the Mn^{2+}-binding regions of conformers 1 **(a)** and 2 **(b)**. Maps (gray surfaces) are shown at 1.5 and 1.3 sigma level, respectively

Supplementary Figure 5

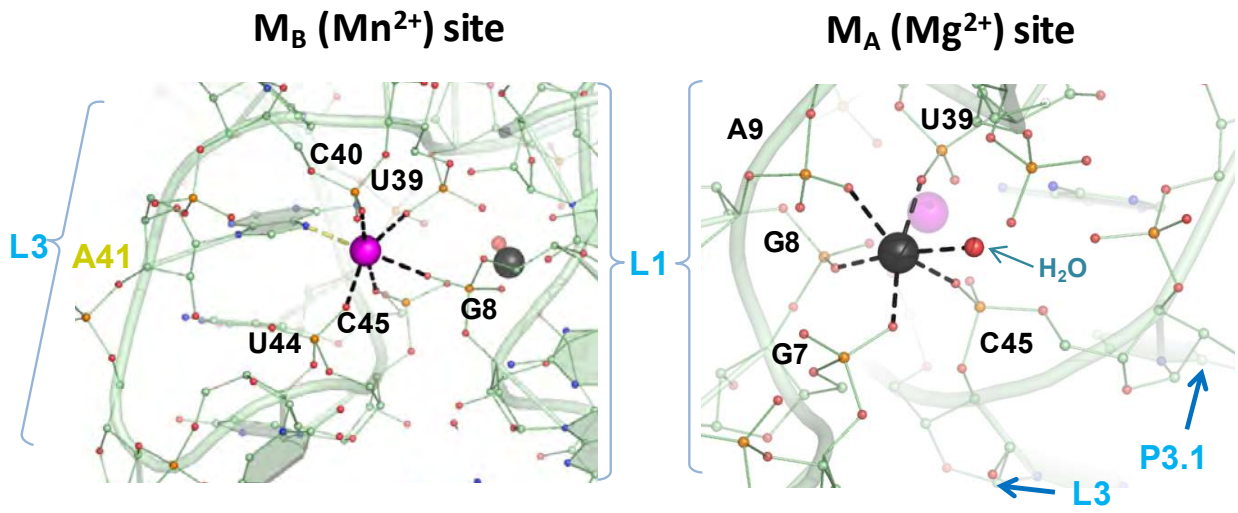

Supplementary Figure 5| Metal binding sites in the *L. lactis yybP-ykoY* structure. Close-up view of the $M_{B,Mn}$ (purple) and $M_{A,Mg}$ (black) metal binding sites showing different contacts with surrounding L3 and L1 residues. The oxygen atoms of water molecules are shown as red spheres.

Supplementary Figure 6

A

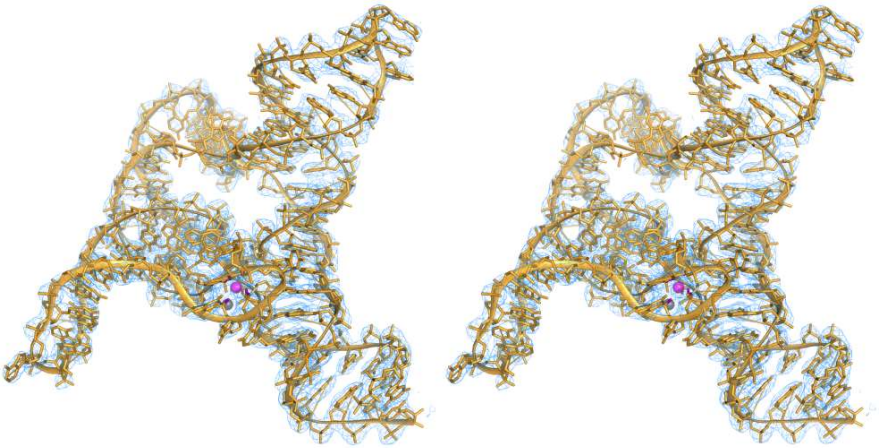

B

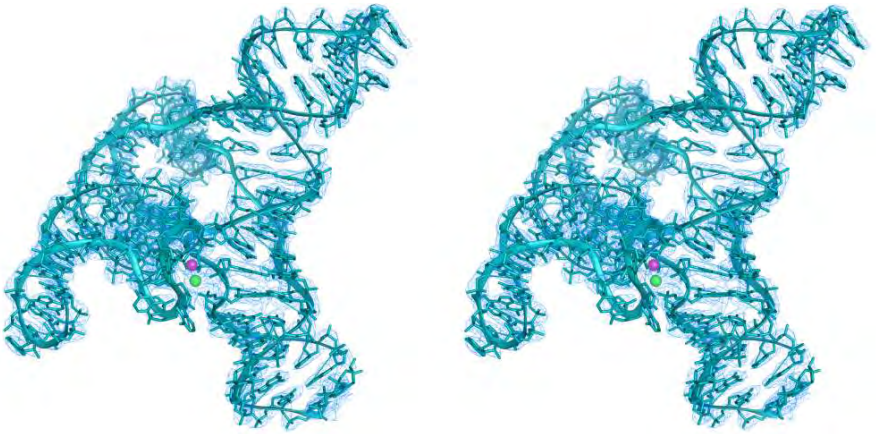

C

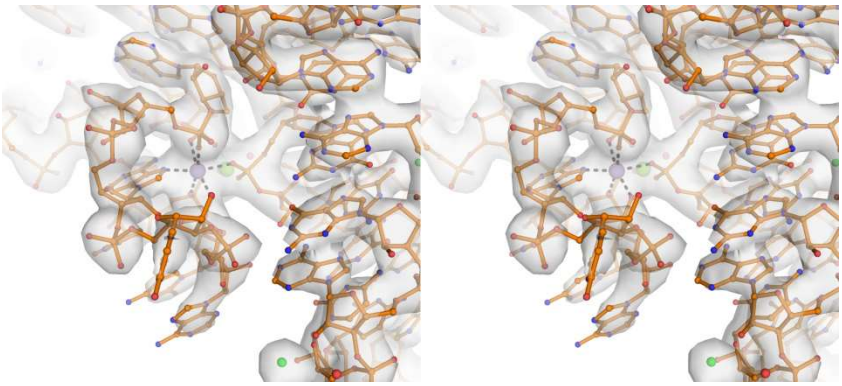

D

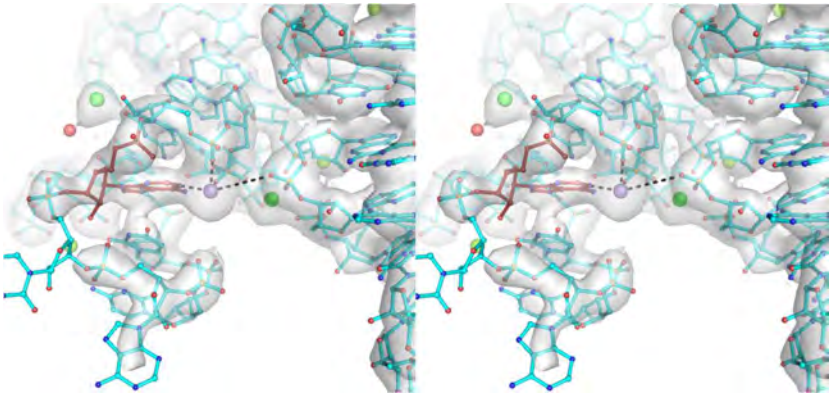

Supplementary Figure 6| Stereoscopic images of the X. *oryzae* riboswitch structure. The overall structures of conformers 1 (A) and 2 (B) are shown. Closer images of the Mn2+-binding regions for conformers 1 and 2 are shown in C and D, respectively. $2F_O$-F_C electron density maps are shown on all at 1.5-sigma level.

Supplementary Table 1. List of 43 MD simulations comprising a cumulative 113 µs simulation time

Organism	PDB ID	Structure	Chain	Ions in active site			solvent box	Length
				$M_{A,Mg}$	$M_{B,Mn}$	M_C		
L. lactis	4Y1I	complete	A	Mg^{2+}	Mn^{2+}	-	rect.	Each 3 µs
				Mg^{2+}	K^+	-		
				K^+	Mn^{2+}	-		
				K^+	K^+	-		
		P1.2|L1|P1.1	A	-	-	-	rect.	3 µs
	6CB3	complete	A with canonical U44	Mg^{2+}	Mn^{2+}	Mg^{2+}	rect.	Each 3 µs
				Mg^{2+}	K^+	Mg^{2+}		
				K^+	Mn^{2+}	Mg^{2+}		
				K^+	K^+	Mg^{2+}		
				Mg^{2+}	Mn^{2+}	K^+		
				Mg^{2+}	K^+	K^+		
				K^+	Mn^{2+}	K^+		
				K^+	K^+	K^+		
			A with deprotonated $U44^-$	Mg^{2+}	Mn^{2+}	Mg^{2+}		
				Mg^{2+}	K^+	Mg^{2+}		
				K^+	Mn^{2+}	Mg^{2+}		
				K^+	K^+	Mg^{2+}		
				Mg^{2+}	Mn^{2+}	K^+		
				Mg^{2+}	K^+	K^+		
				K^+	Mn^{2+}	K^+		
				K^+	K^+	K^+		
			B	Mg^{2+}	Mn^{2+}	-		
				Mg^{2+}	K^+	-		
				K^+	Mn^{2+}	-		
				K^+	K^+	-		
X. oryzae	This study	complete	Conformer 2 with *anti* A48	Mg^{2+}	Mn^{2+}	-	oct.	Each 2 µs
				Mg^{2+}	K^+	-		
				K^+	Mn^{2+}	-		
				K^+	K^+	-		
			Conformer 2 with *syn* A48	Mg^{2+}	Mn^{2+}	-		
				Mg^{2+}	K^+	-		
				K^+	Mn^{2+}	-		
				K^+	K^+	-		
		P1.2|L1|P1.1	Conformer 2	-	-	-	rect.	3 µs
		complete	Conformer 1	Mg^{2+}	Mn^{2+}	-	oct.	Each twice 2 µs
				Mg^{2+}	K^+	-		
				K^+	Mn^{2+}	-		
				K^+	K^+	-		

		P1.2|L1|P1.1	Conformer 1	-	-	-	rect.	3 µs

Supplementary Figure 7

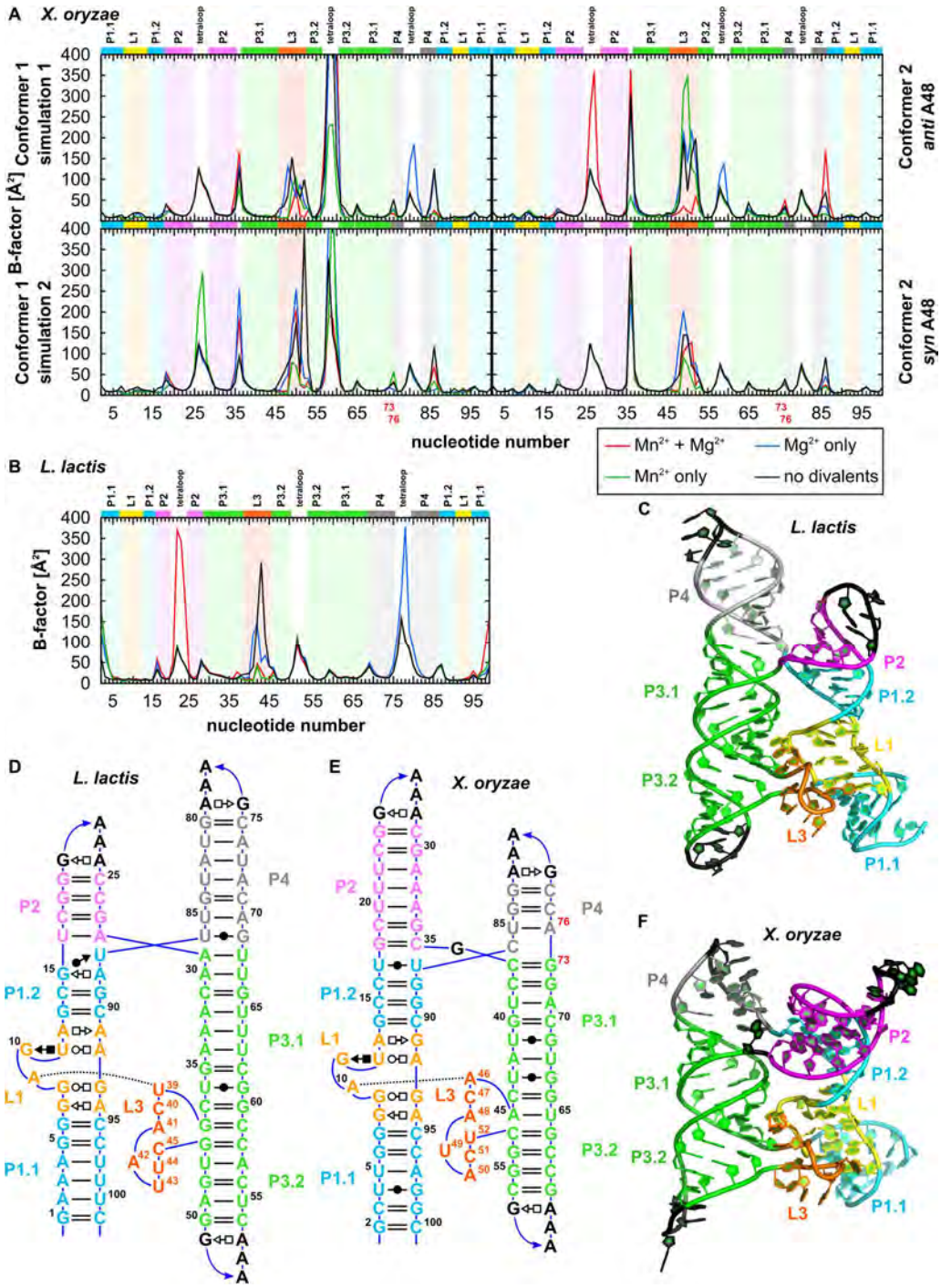

Supplementary Figure 7| The average mass-weighted B-factor as a function of residue number obtained in MD simulations of Mn^{2+} sensing riboswitch from A) *Xanthomonas oryzae* or B) *Lactococcus lactis* (see **Supplementary Table 1** in the main text for full list of the simulations). The colors of background bars correspond to the regions in the secondary and 3D structures shown on panels C-F.

Supplementary Figure 8

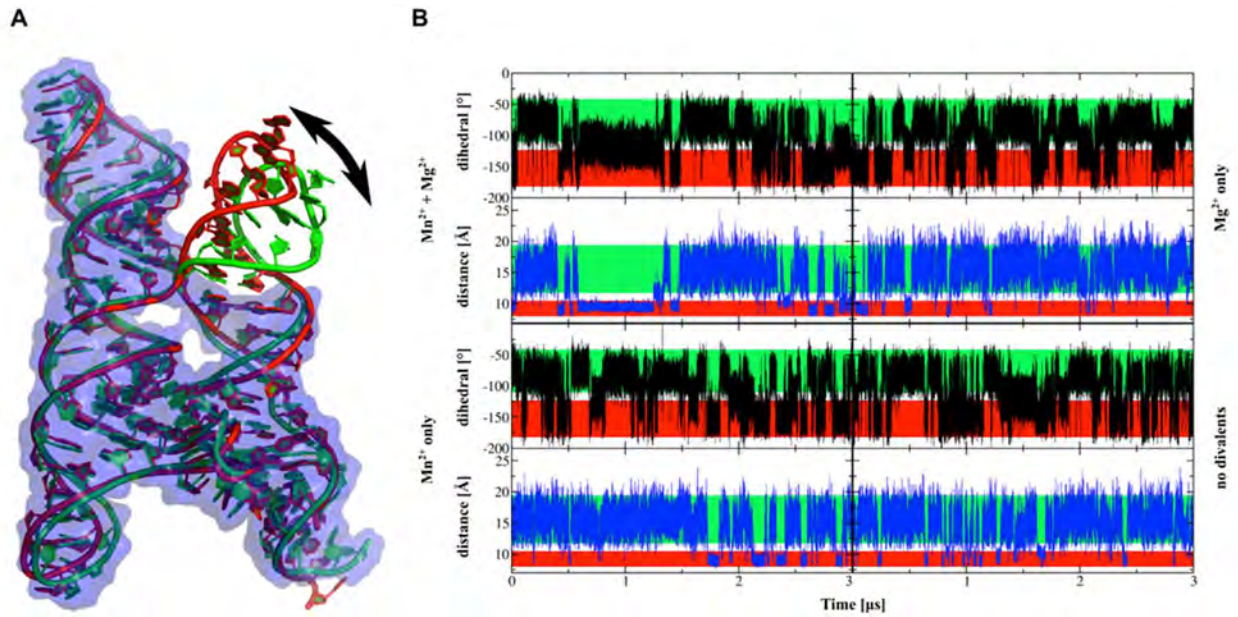

Supplementary Figure 8| A) Superposition of the open and closed conformation (in green and red, respectively) observed in MD simulation of the aptamer from *L. lactis*. B) Time dependence of ε dihedral angle of A28 (black line) and distance between P2 (center of mass of C17-G20 backbone) and P4 (center of mass of C71-A72 backbone) stems (blue line). The green and the red strips on the background correspond to the open (native crystal-like) and closed conformation, respectively.

Supplementary Figure 9

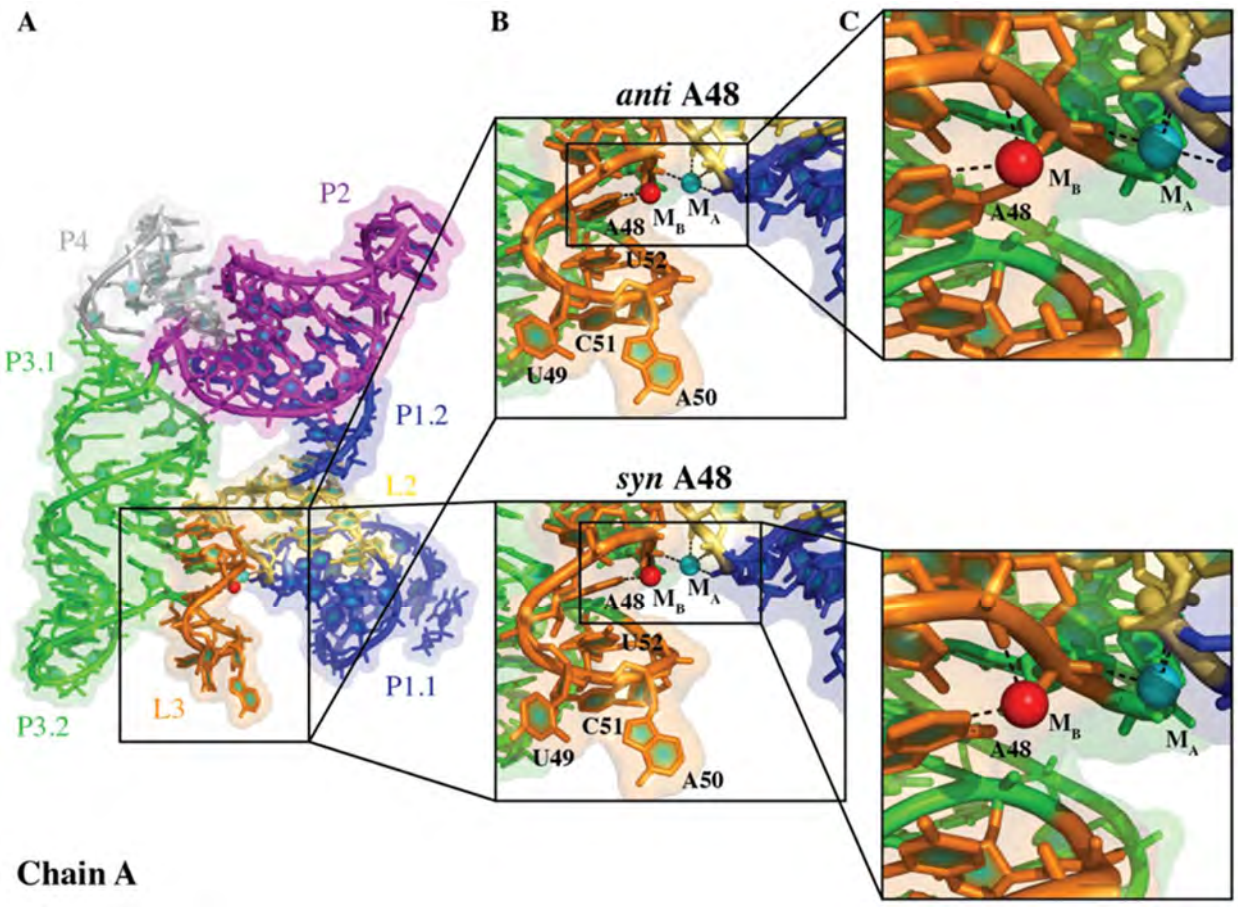

Supplementary Figure 9| Structure of *X. oryzae* aptamer domain of conformer 2 showing alternative *syn* and *anti*-orientations of A48.

Supplementary Figure 10

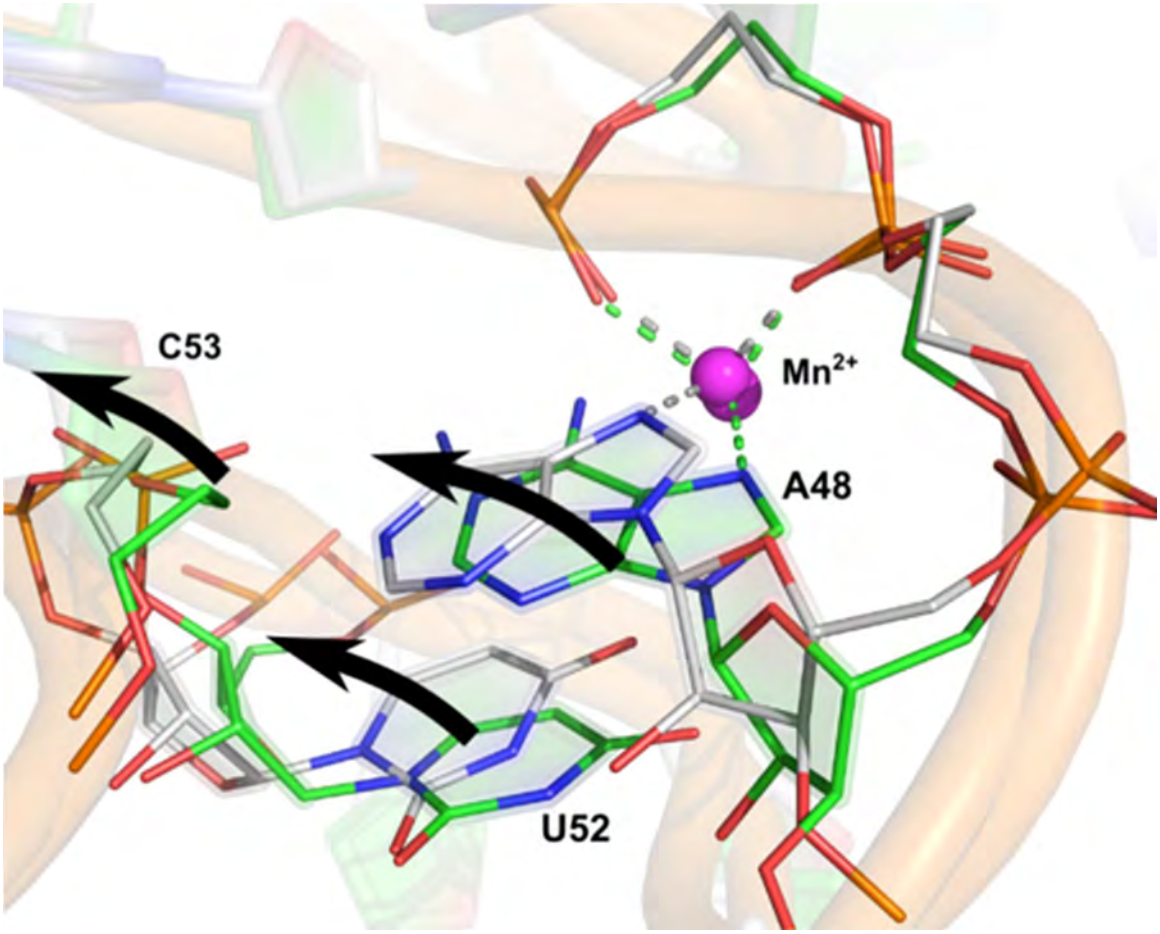

Supplementary Figure 10| Structural changes observed during early stages of the MD simulations of *X. oryzae* conformer 2 with *anti*-orientation of A48. Green structure corresponds to crystal structure, while the silver refers to the structure after initial rearrangements during these early stages.

Supplementary Figure 11

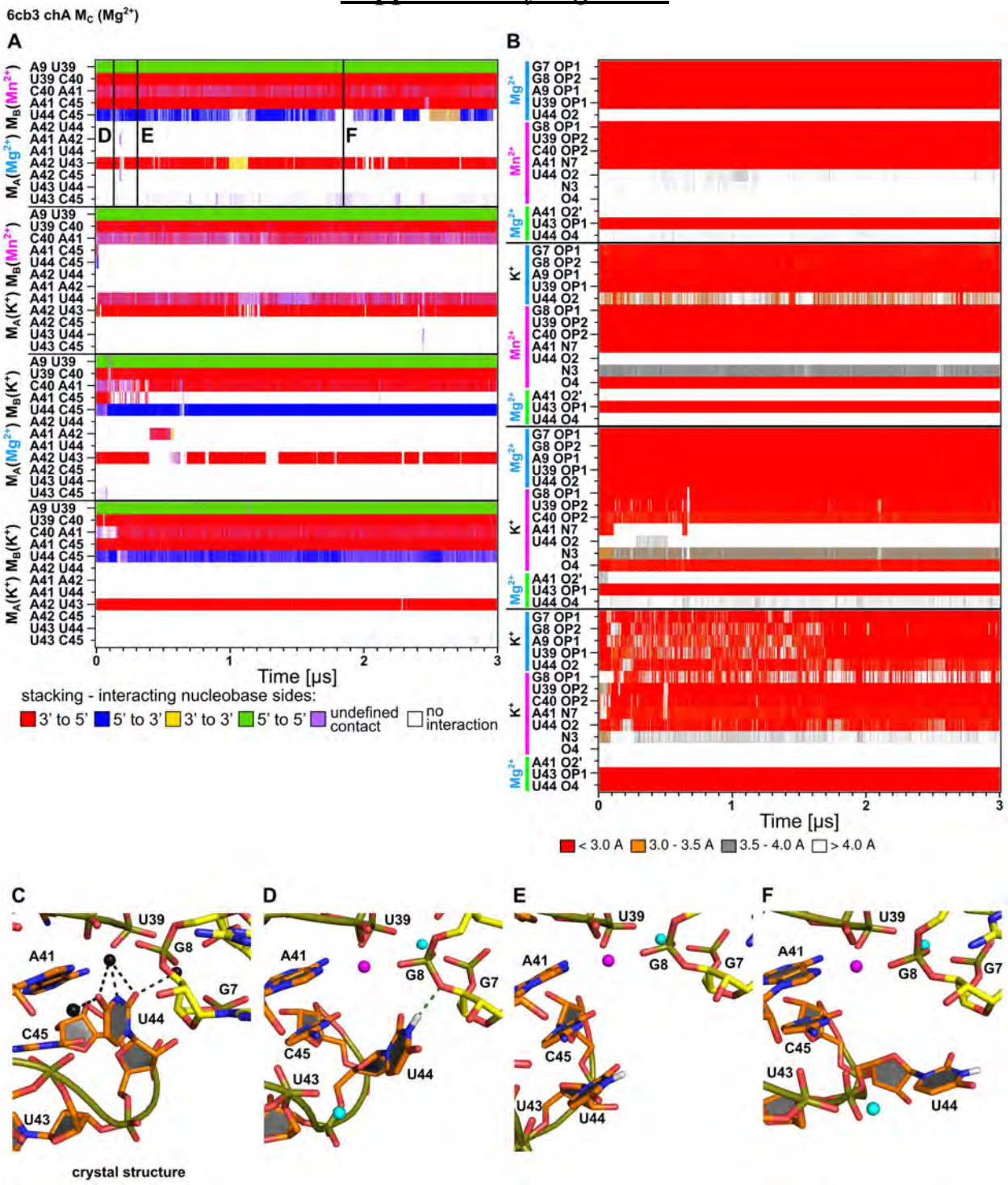

Supplementary Figure 11| Conformational behavior of the L3 loop and the M_A, M_B and M_C ion binding sites in MD simulations of the *L. lactis* riboswitch starting from the chain A of the 6CB3 structure with the M_C site occupied by a Mg^{2+} ion. (**A**) Time evolution of the stacking pattern of the loop; the colors correspond to different mutual orientations of nucleobases in stacking

interactions indicated by the corresponding faces (3'-face and 5'-face) involved in the interaction. (**B**) Time evolution of ligand-ion interactions in the ion binding sites. (**C**) Unusual arrangement of the ion binding sites in the crystal structure involving three Cd^{2+} ions. (**D-F**) Snapshots from the MD simulations (indicated by black vertical lines in panel A), documenting different conformations that the canonical U44 sampled after its ejection from the ion binding site.

Supplementary Figure 12

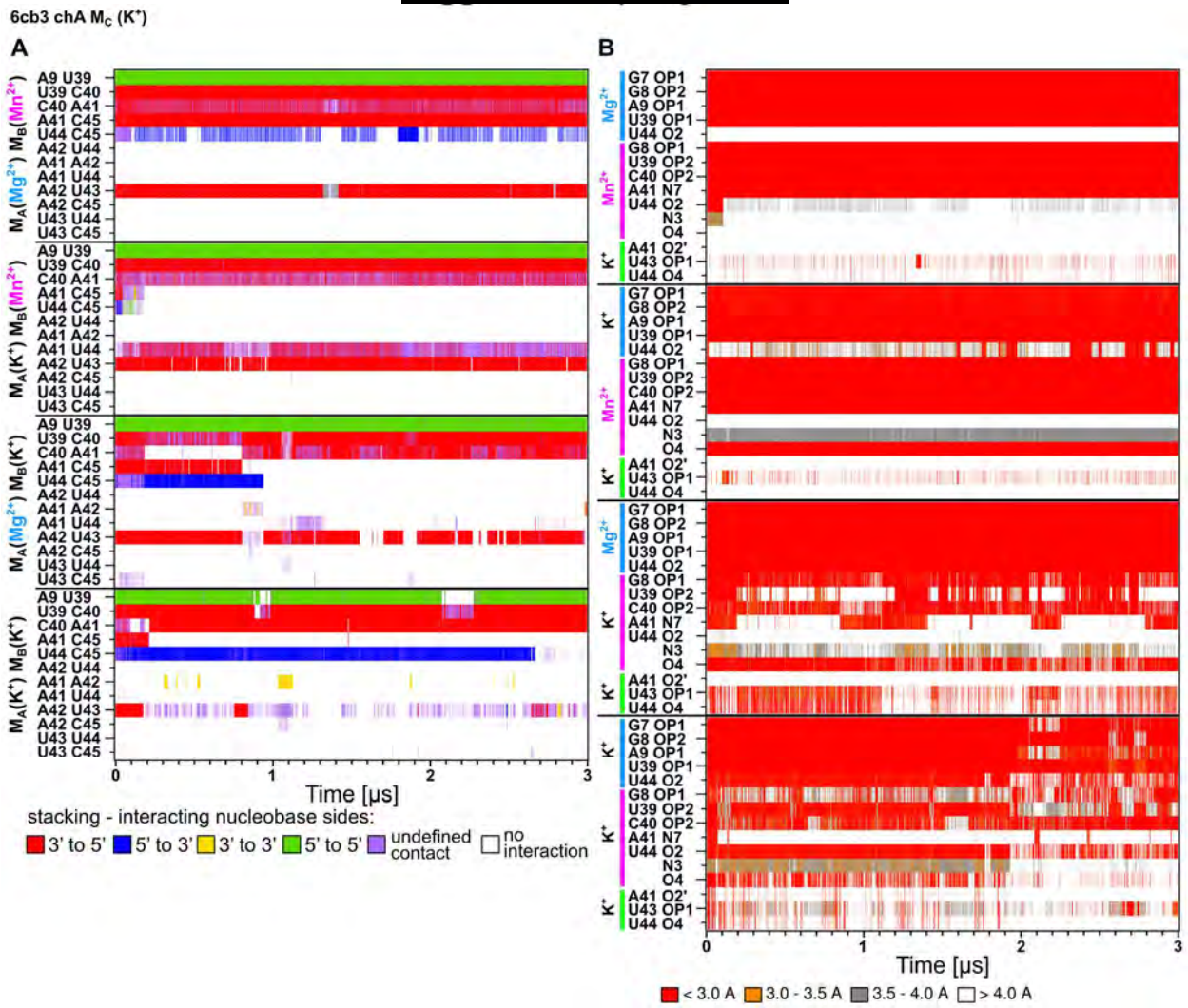

Supplementary Figure 12| Conformational behavior of the L3 loop and the M_A, M_B and M_C ion binding sites in MD simulations of the *L. lactis* riboswitch starting from chain A of the 6CB3 structure with the M_C site occupied by a K^+ ion. (**A**) Time evolution of the stacking pattern of the loop; the colors correspond to different mutual orientations of nucleobases in stacking interactions indicated by the corresponding faces (3'-face and 5'-face) involved in the interaction. (**B**) Time evolution of ligand-ion interactions in the ion binding sites.

Supplementary Figure 13

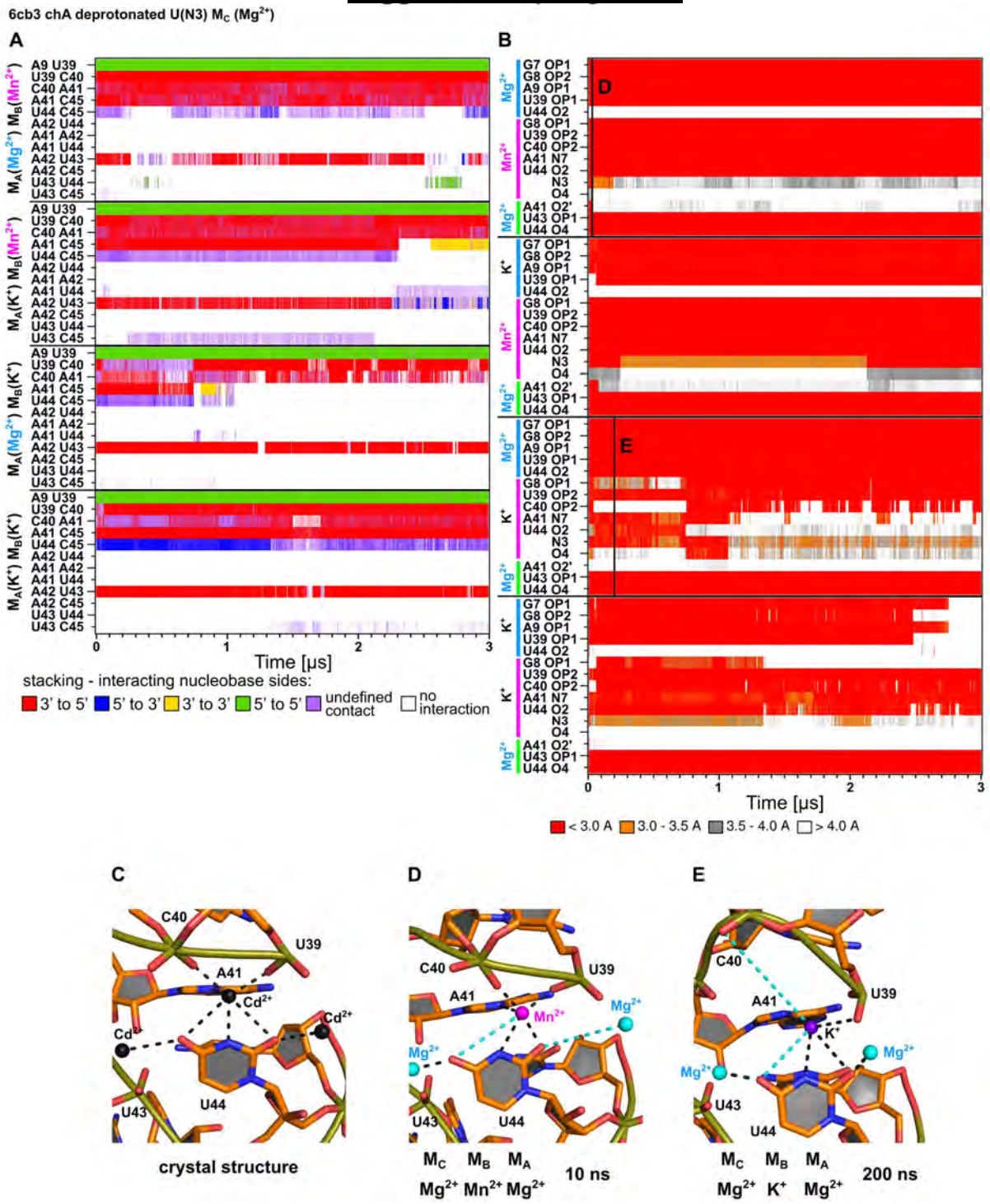

Supplementary Figure 13| Conformational behavior of the L3 loop and the M_A, M_B and M_C ion binding sites in MD simulations of the *L. lactis* riboswitch starting from chain A of the 6CB3 structure with the M_C site occupied by a Mg^{2+} ion and with an N3-deprotonated U44. (**A**) Time evolution of the stacking pattern of the loop; the colors correspond to different mutual orientations of nucleobases in stacking interactions indicated by the corresponding faces (3'-face

and 5'-face) involved in the interaction. (**B**) Time evolution of ligand-ion interactions in the ion binding sites. (**C**) Unusual arrangement of the ion binding sites in the crystal structure involving three Cd^{2+} ions. (**D-E**) Snapshots from the MD simulations (indicated by black vertical lines in panel B) documenting modest shifts of N3-deprotonated $U44^{-}$ within the binding site as observed in MD simulations. The stable and broken contacts are depicted by black and cyan dashed lines, respectively.

Supplementary Figure 14

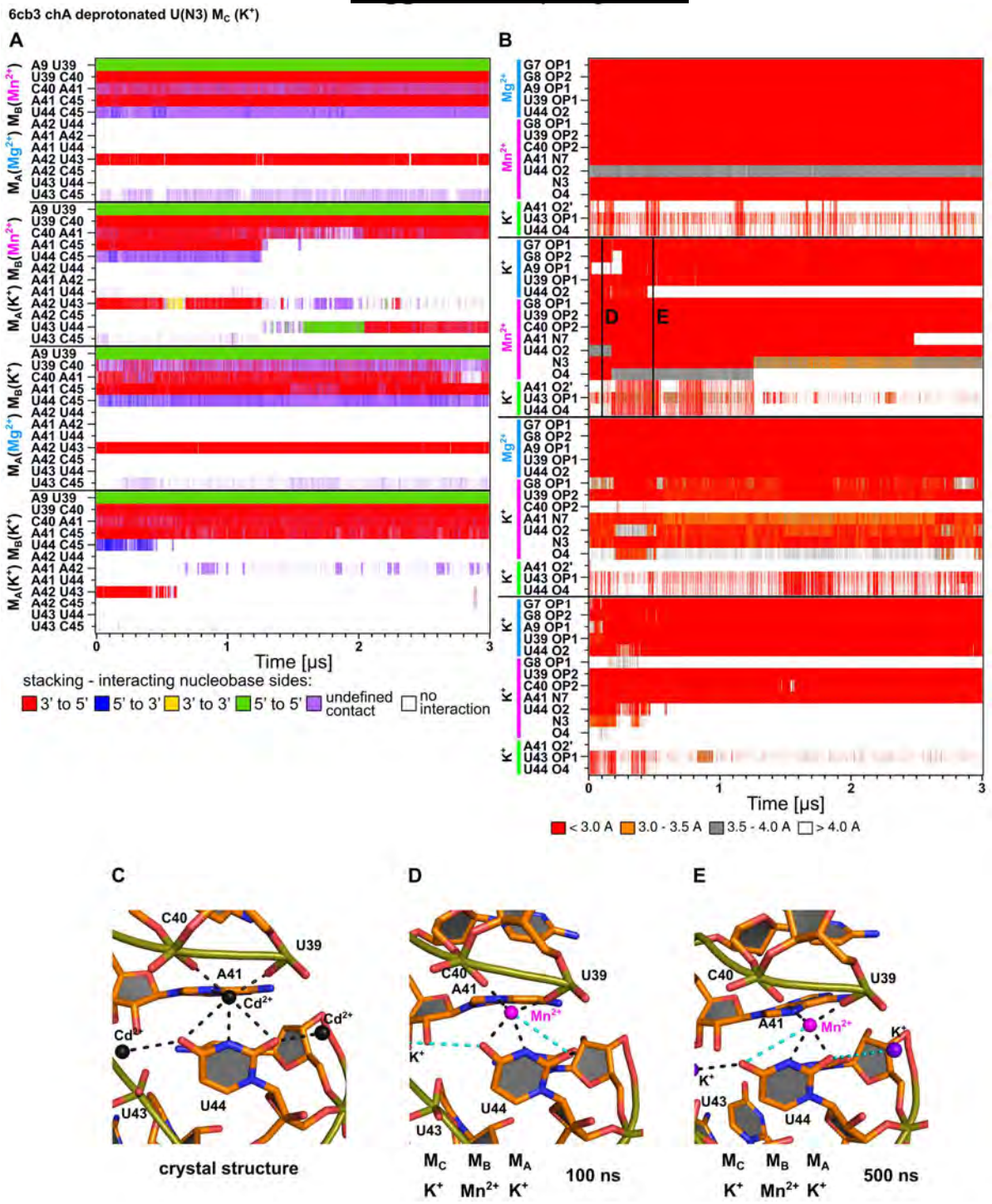

Supplementary Figure 14| Conformational behavior of the L3 loop and the M_A, M_B and M_C ion binding sites in MD simulation of the *L. lactis* riboswitch starting from chain A of the 6CB3 structure with the M_C site occupied by a K^+ ion and with an N3-deprotonated U44. (**A**) Time evolution of the stacking pattern of the loop; the colors correspond to different mutual orientations of nucleobases in stacking interactions indicated by the corresponding faces (3'-face

and 5'-face) involved in the interaction. (**B**) Time evolution of ligand-ion interactions in the ion binding sites. (**C**) Unusual arrangement of the ion binding sites in the crystal structure involving three Cd^{2+} ions. (**D-E**) Snapshots from the MD simulations (indicated by black vertical lines in panel B) documenting modest shifts of the N3-deprotonated $U44^{-}$ within the binding site as observed in MD simulations. The stable and broken contacts are depicted by black and cyan dashed lines, respectively.

Supplementary Table 2: Percentage of native stacking preserved in the L3 loop during MD simulation (based on annotations calculated by the baRNAba software[1]) and a percentage of ion occupancy in the ion binding sites. 4Y1I_chA and 6CB3_chB correspond to simulations of the *L. lactis* riboswitch starting from the 4Y1I chain A and 6CB3 chain B structures, respectively. Xory_cf1_1, X.ory_cf1_2 and X.ory_cf2_syn signify two independent simulations of *X. oryzae* Conformer 1 structure and one simulation of Conformer 2 with *syn*-oriented A48, respectively (see **Supplementary Table 1**).

	Ions		**Stacking interactions [%]**						**Occupancy of M_A [%]**					**Occupancy of M_B [%]**					
	M_A	**M_B**	**A9 U39**	**U39 C40**	**C40 A41**	**A41 C45**	**U44 C45**	**A42 U44**	**G7 OP1**	**G8 OP2**	**A9 OP1**	**U39 OP1**	**C45 OP1**	**G8 OP1**	**U39 OP2**	**C40 OP2**	**A41 N7**	**U44 OP1**	**C45 OP2**
4Y1I_chA	Mg^{2+}	Mn^{2+}	100	98	77	98	92	76	100	100	100	100	100	100	100	100	100	100	100
	K^+	Mn^{2+}	99	99	78	96	65	83	100	100	100	100	2	100	100	100	100	100	100
	Mg^{2+}	K^+	99	99	2	4	5	6	100	100	100	100	100	100	100	98	6	0	100
	K^+	K^+	100	93	64	88	36	42	95	98	95	100	0	27	99	78	97	42	67
6CB3_chB	Mg^{2+}	Mn^{2+}	100	98	78	98	94	58	100	100	100	100	100	100	100	100	100	100	100
	K^+	Mn^{2+}	98	100	81	96	66	92	100	100	100	100	2	100	100	100	100	100	100
	Mg^{2+}	K^+	99	53	43	20	1	0	100	100	100	100	100	99	100	30	100	0	99
	K^+	K^+	99	98	58	97	23	37	98	99	98	100	0	52	100	95	97	52	64
			A10 A46	**A46 C47**	**C47 A48**	**A48 U52**	**C51 U52**	**A50 C51**	**G8 OP2**	**G9 OP2**	**A10 OP1**	**A46 OP1**	**U52 OP1**	**G9 OP1**	**A46 OP2**	**C47 OP2**	**A48 N7/1**	**C51 OP1**	**U52 OP2**
X.ory_cf2_syn	Mg^{2+}	Mn^{2+}	100	100	100	66	61	63	100	100	100	100	0	0	100	100	100	0	0
	K^+	Mn^{2+}	91	100	100	81	86	89	99	99	100	100	0	0	100	100	100	0	0
	Mg^{2+}	K^+	100	99	87	69	82	89	100	100	100	100	0	65	68	67	68	17	17
	K^+	K^+	96	99	89	70	90	67	95	98	98	98	45	6	90	67	68	10	67
X.ory_cf1_1	Mg^{2+}	Mn^{2+}	100	100	54	92	84	11	0	100	0	100	100	100	100	100	100	100	100
	K^+	Mn^{2+}	98	96	70	75	70	47	99	100	100	100	1	100	100	100	100	100	100
	Mg^{2+}	K^+	99	86	5	1	5	2	0	100	0	100	100	25	24	21	6	5	24
	K^+	K^+	97	99	76	69	78	86	79	85	79	92	11	20	85	74	82	19	38
X.ory_cf1_2	Mg^{2+}	Mn^{2+}	100	99	57	90	86	3	0	100	0	100	100	100	100	100	100	100	100
	K^+	Mn^{2+}	93	97	82	45	86	11	99	100	99	100	1	100	100	100	100	100	100
	Mg^{2+}	K^+	100	99	84	2	15	24	0	100	0	100	100	99	99	100	25	4	100
	K^+	K^+	87	95	54	37	47	60	35	94	62	97	5	72	34	83	76	59	23

Supplementary Table 2 Continuation: 6CB3_chA_U44canonic and 6CB3_chA_U44_N3-deprot signify simulations starting from the 6CB3 chain A structure with canonical and N3-deprotonated U44, respectively (see **Supplementary Table 1**).

	Ions			Stacking interactions [%]						Occupancy of M_A [%]					Occupancy of M_B [%]							M_C [%]		
	M_A	M_B	M_C	A9 U39	U39 C40	C40 A41	A41 C45	U44 C45	A42 U43	G7 OP1	G8 OP2	A9 OP1	U39 OP1	U44 O2	G8 OP1	U39 OP2	C40 OP2	A41 N7	U44 O2	N3	O4	A41 O2'	U43 OP1	U44 O4
6CB3 chA **U44 canonic**	Mg^{2+}	Mn^{2+}	Mg^{2+}	100	98	66	99	55	86	100	100	100	100	0	100	100	100	100	0	0	0	0	100	0
	K^+	Mn^{2+}	Mg^{2+}	100	94	41	0	0	94	100	100	100	100	29	100	100	100	100	0	0	100	0	100	0
	Mg^{2+}	K^+	Mg^{2+}	100	96	81	5	97	83	100	100	100	100	100	99	96	97	5	0	16	99	0	100	0
	K^+	K^+	Mg^{2+}	99	96	73	97	55	98	94	85	85	83	89	48	97	96	98	89	2	0	0	100	100
	Mg^{2+}	Mn^{2+}	K^+	100	99	59	100	39	93	100	100	100	100	0	100	100	100	100	3	1	0	0	10	4
	K^+	Mn^{2+}	K^+	100	96	44	1	1	95	100	100	100	100	25	100	100	100	100	0	0	100	0	13	0
	Mg^{2+}	K^+	K^+	98	86	56	24	25	78	100	100	100	100	100	90	44	85	38	0	15	83	0	47	38
	K^+	K^+	K^+	89	93	93	7	78	11	95	97	91	100	82	46	71	80	5	82	19	40	6	19	10
6CB3 chA **U44 N3-deprot**	Mg^{2+}	Mn^{2+}	Mg^{2+}	100	98	75	71	6	55	100	100	100	100	0	100	100	100	100	100	6	0	1	100	100
	K^+	Mn^{2+}	Mg^{2+}	100	85	74	75	1	61	100	100	100	98	0	100	100	100	100	100	85	0	2	100	100
	Mg^{2+}	K^+	Mg^{2+}	98	72	49	23	3	93	100	100	100	100	100	84	99	57	43	24	62	18	0	100	100
	K^+	K^+	Mg^{2+}	99	94	53	98	46	94	91	81	91	83	0	38	100	96	99	92	32	0	0	100	100
	Mg^{2+}	Mn^{2+}	K^+	100	99	44	98	3	95	100	100	100	100	100	100	100	100	100	0	100	100	9	43	24
	K^+	Mn^{2+}	K^+	100	98	71	40	4	34	100	98	92	100	14	100	100	100	83	94	68	6	16	32	19
	Mg^{2+}	K^+	K^+	99	23	75	92	13	98	100	100	100	100	100	87	100	0	92	89	99	11	0	43	33
	K^+	K^+	K^+	100	96	84	85	7	17	99	100	98	100	98	1	100	99	100	13	8	0	0	16	6

Supplementary Figure 15

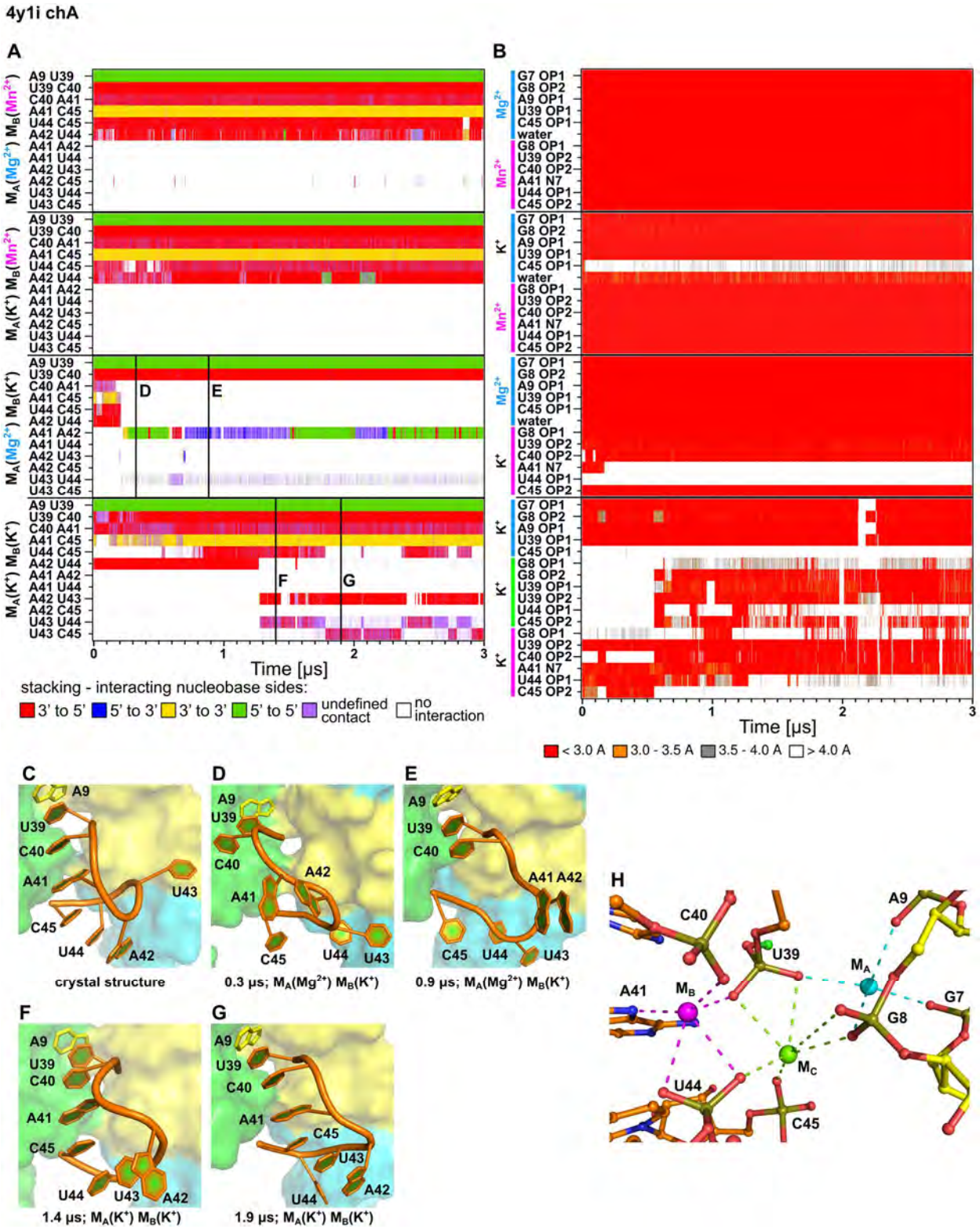

Supplementary Figure 15| Conformational behavior of the L3 loop and the M_A and M_B ion binding sites in MD simulations of the *L. lactis* riboswitch (4Y1I chain A). (**A**) Time evolution of the stacking pattern of the loop; the colors correspond to different mutual orientations of nucleobases in stacking interactions indicated by the corresponding faces (3'-face and 5'-face) involved in the interaction. (**B**) Time evolution of ligand-ion interactions in the ion binding sites. (**C-G**) Close view of the stacking patterns; panel C corresponds to the crystal structure while the other panels depict structures observed in MD simulations at the times indicated by vertical bars in the panel A. (**H**) New ion binding sites appear in simulations where both divalents were replaced by K^+ (the colors of the ions match the colors of the bars in panel B, helping to identify the particular binding sites).

Supplementary Figure 16

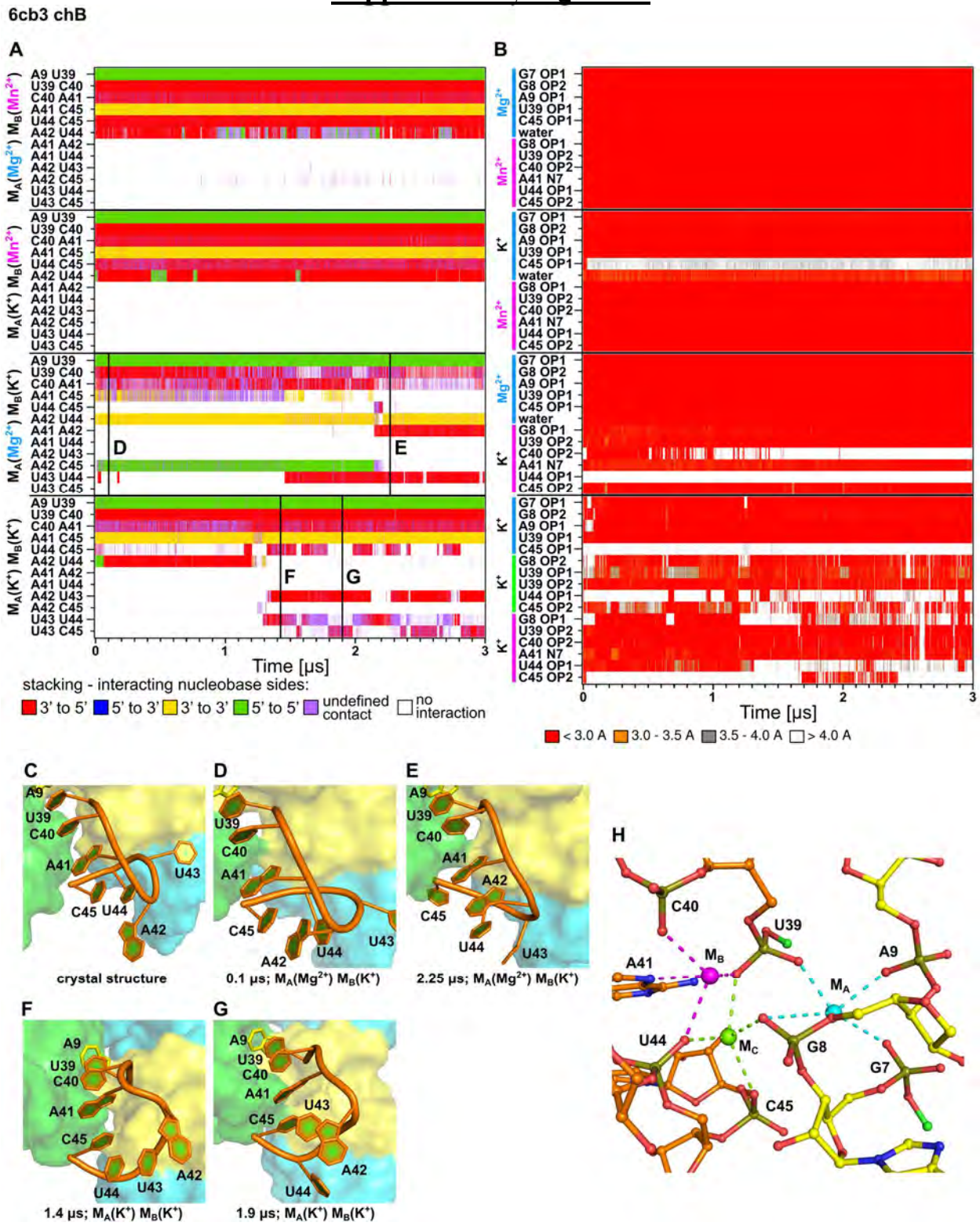

Supplementary Figure 16| Conformational behavior of the L3 loop and the M_A and M_B ion binding sites in MD simulations of the *L. lactis* ribozyme (6CB3 chain B). (**A**) Time evolution of

the stacking pattern of the loop; the colors correspond to different mutual orientations of nucleobases in stacking interactions indicated by the corresponding faces (3'-face and 5'-face) exposed to the interaction. (**B**) Time evolution of ligand-ion interactions in the ion binding sites. (**C-G**) Close view on the stacking pattern; panel C corresponds to the crystal structure while the others depict structures observed in MD simulations at the times indicated by vertical bars in panel A. (**H**) New ion binding sites appear in simulations where both divalents were replaced by K^+ (the colors of the ions match the colors of the bars in panel B, helping to indicate the particular binding site).

Supplementary Figure 17

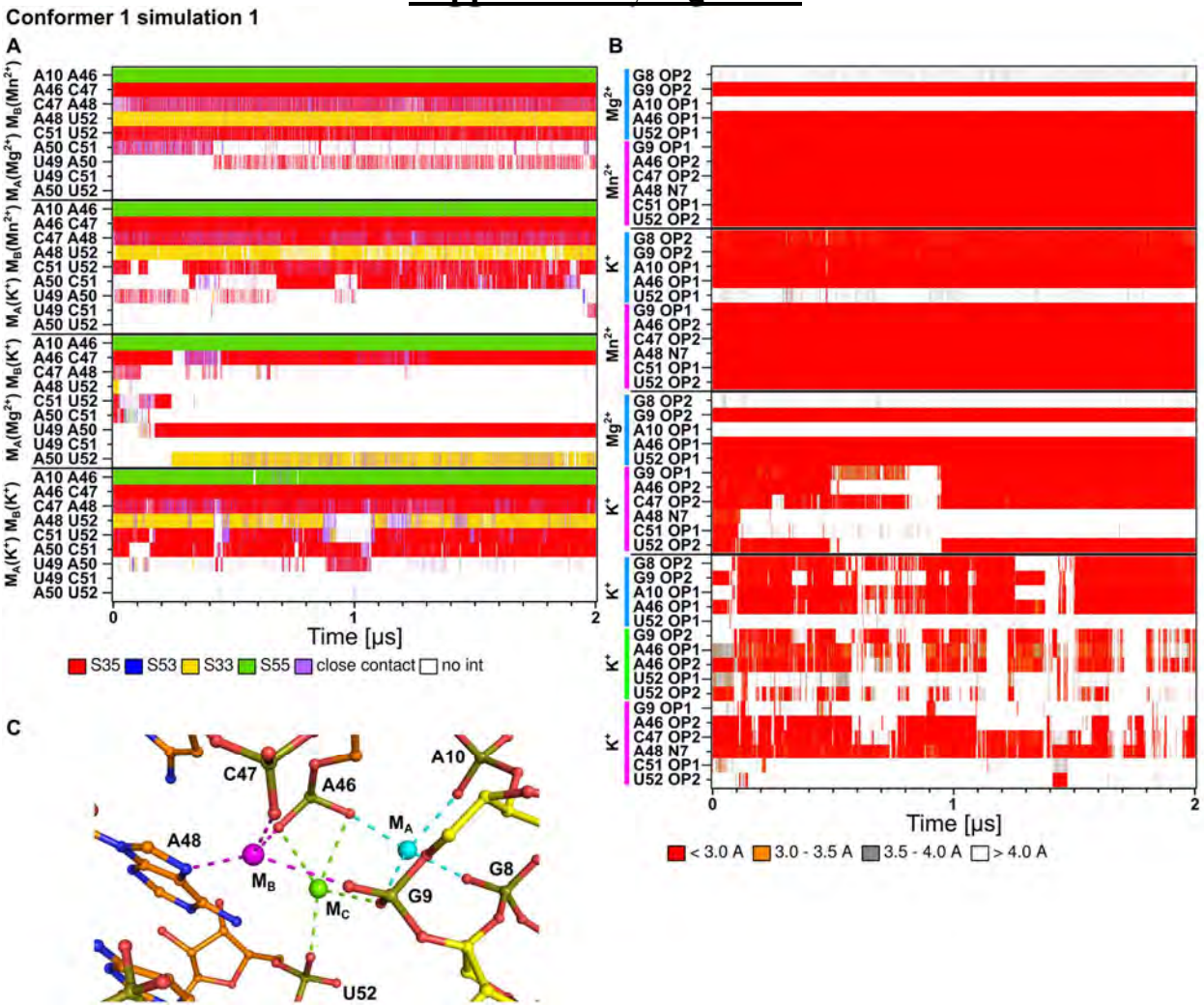

Supplementary Figure 17| Conformational behavior of the L3 loop and M_A and M_B ion binding sites in MD simulations of the *X. oryzae* riboswitch. (**A**) Time evolution of the stacking pattern of the loop; the colors correspond to different mutual orientations of nucleobases in stacking interactions indicated by the corresponding faces (3'-face and 5'-face) involved in the interaction. (**B**) Time evolution of ligand-ion interactions in the ion binding sites. (**C**) New ion binding sites appear in simulations where both divalents were replaced by K^+ (the colors of the ions match the colors of the bars in panel B, helping to indicate the particular binding site). Here only the data from the *X. oryzae* Conformer 1 simulation 1 are shown, while the data from other simulations are presented below.

Supplementary Figure 18

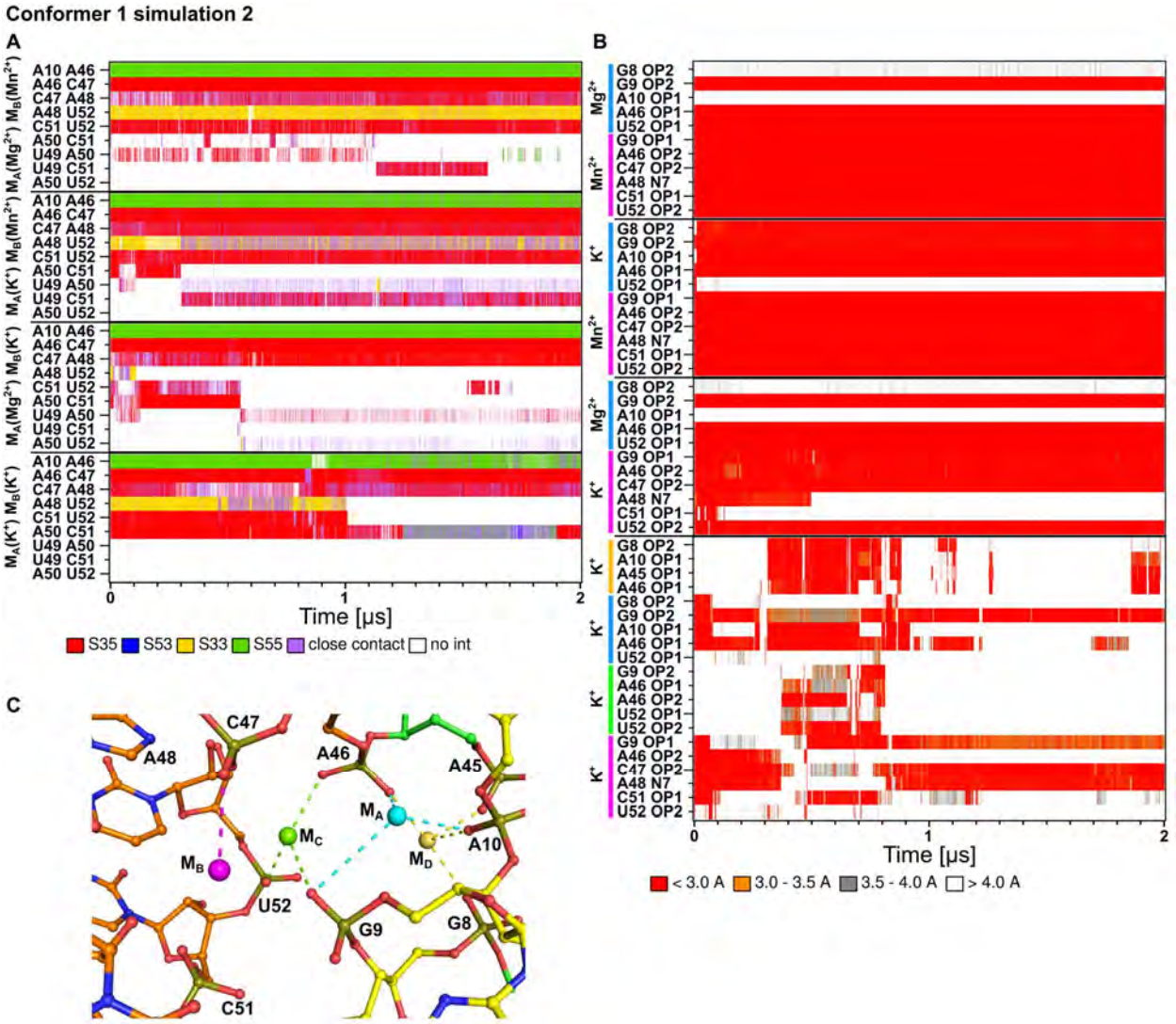

Supplementary Figure 18| Continuation of panels A-C for the data from *X. oryzae* Conformer 1 simulation 2.

Supplementary Figure 19

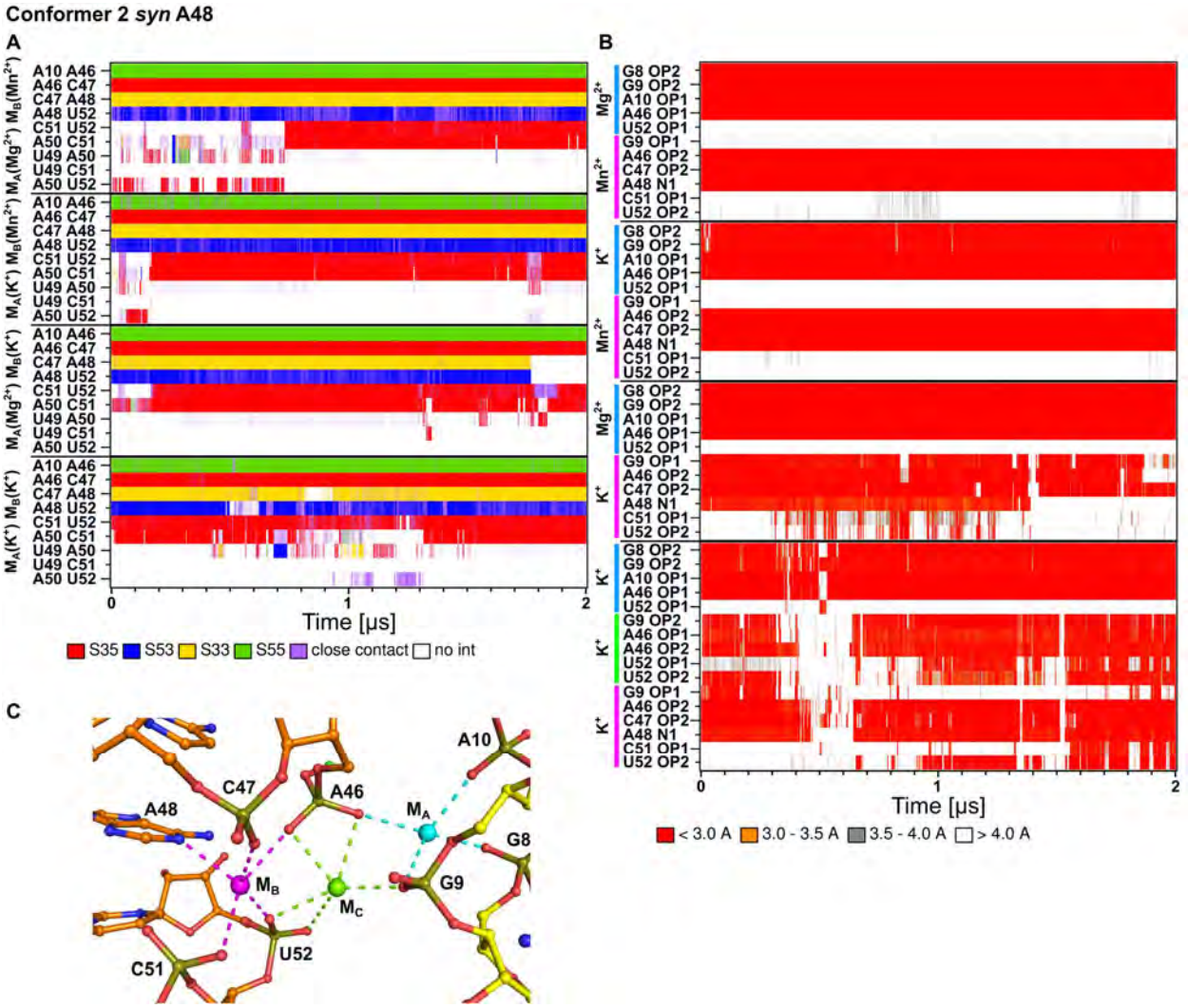

Supplementary Figure 19| Continuation of panels A-C for the data from *X. oryzae* Conformer 2 (the simulation with *syn*-oriented A48, see **Supplementary Table 1**)

Supplementary Figure 20

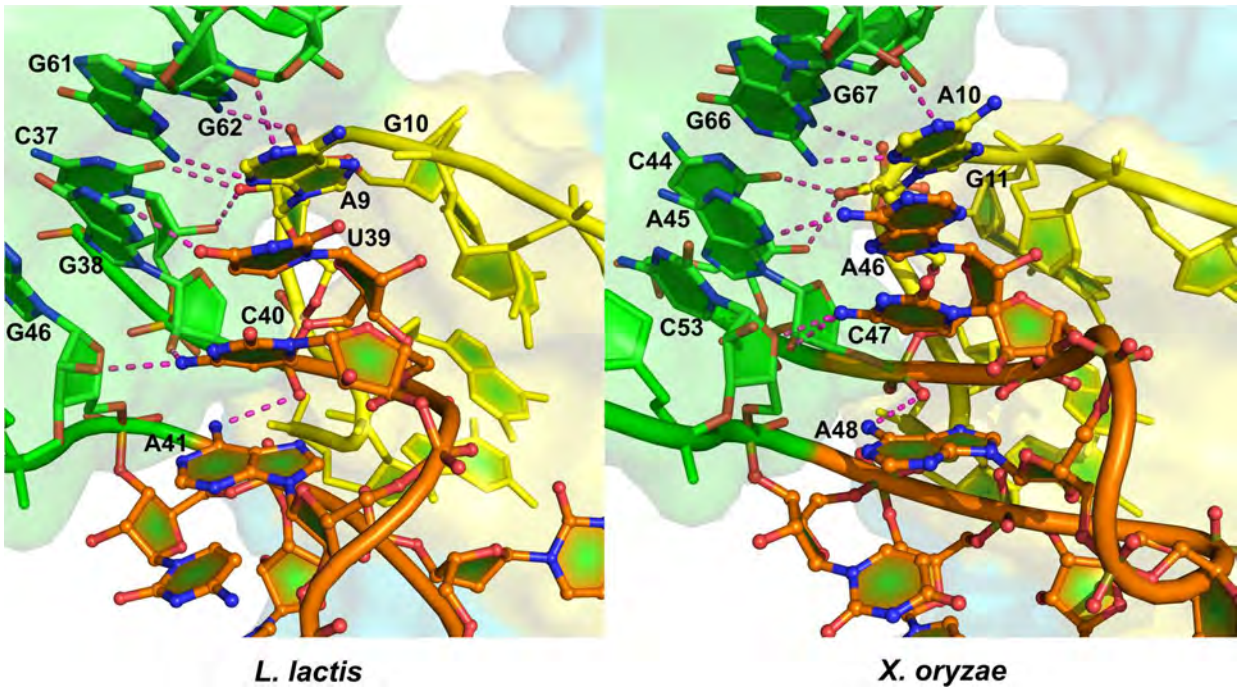

Supplementary Figure 20| The stacking pattern formed by A10 (A9 according to numbering of *L. lactis*) and nucleobases of loop L3 with depicted tertiary interactions (see **Supplementary Figure 21** for their structural stabilities in MD simulations).

Supplementary Figure 21

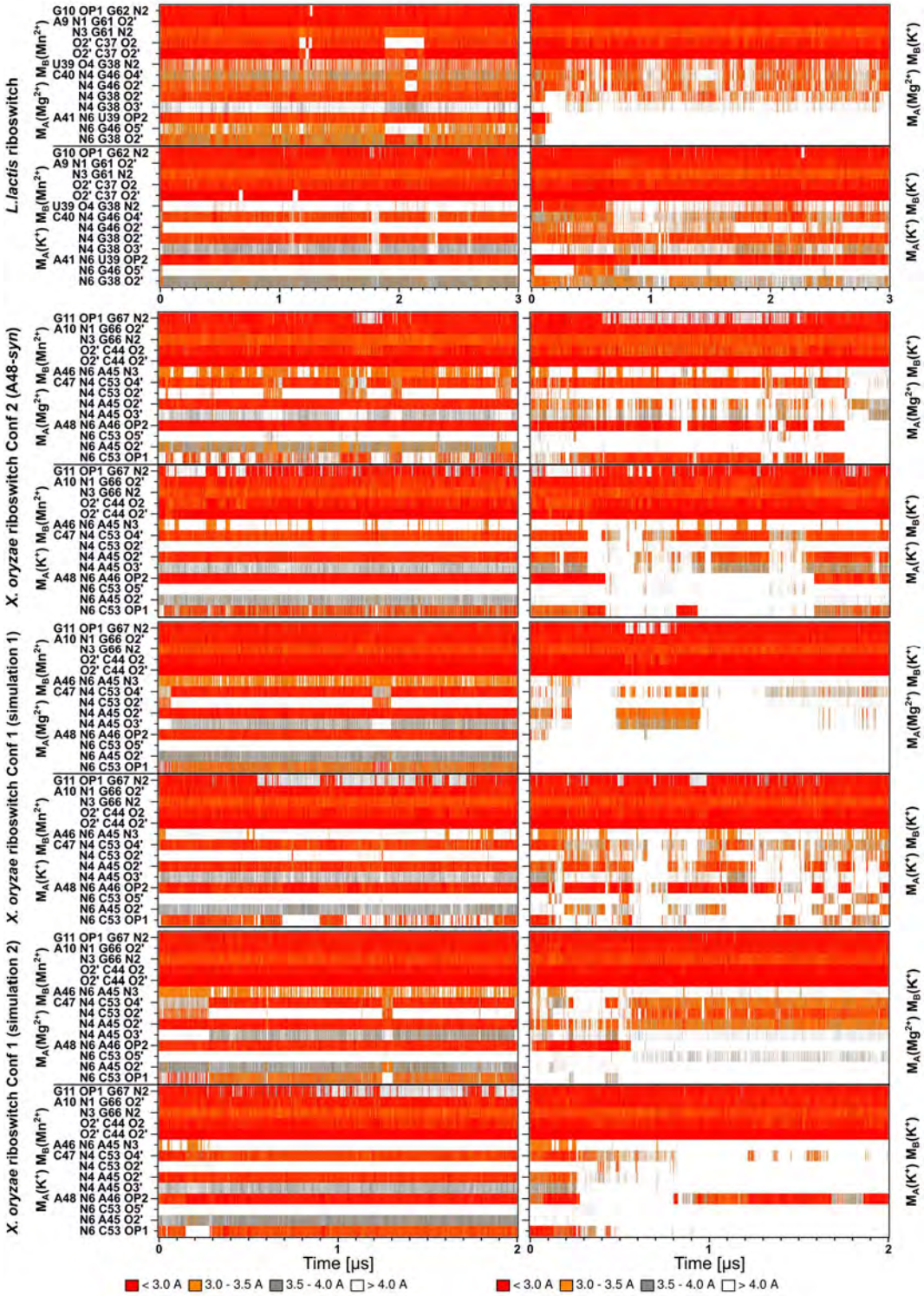

Supplementary Figure 21| Time evolution of tertiary interactions of nucleotides included in the stacking pattern of L3 loop (see **Supplementary Figure 20** for structural view of these tertiary contacts).

Supplementary Figure 22

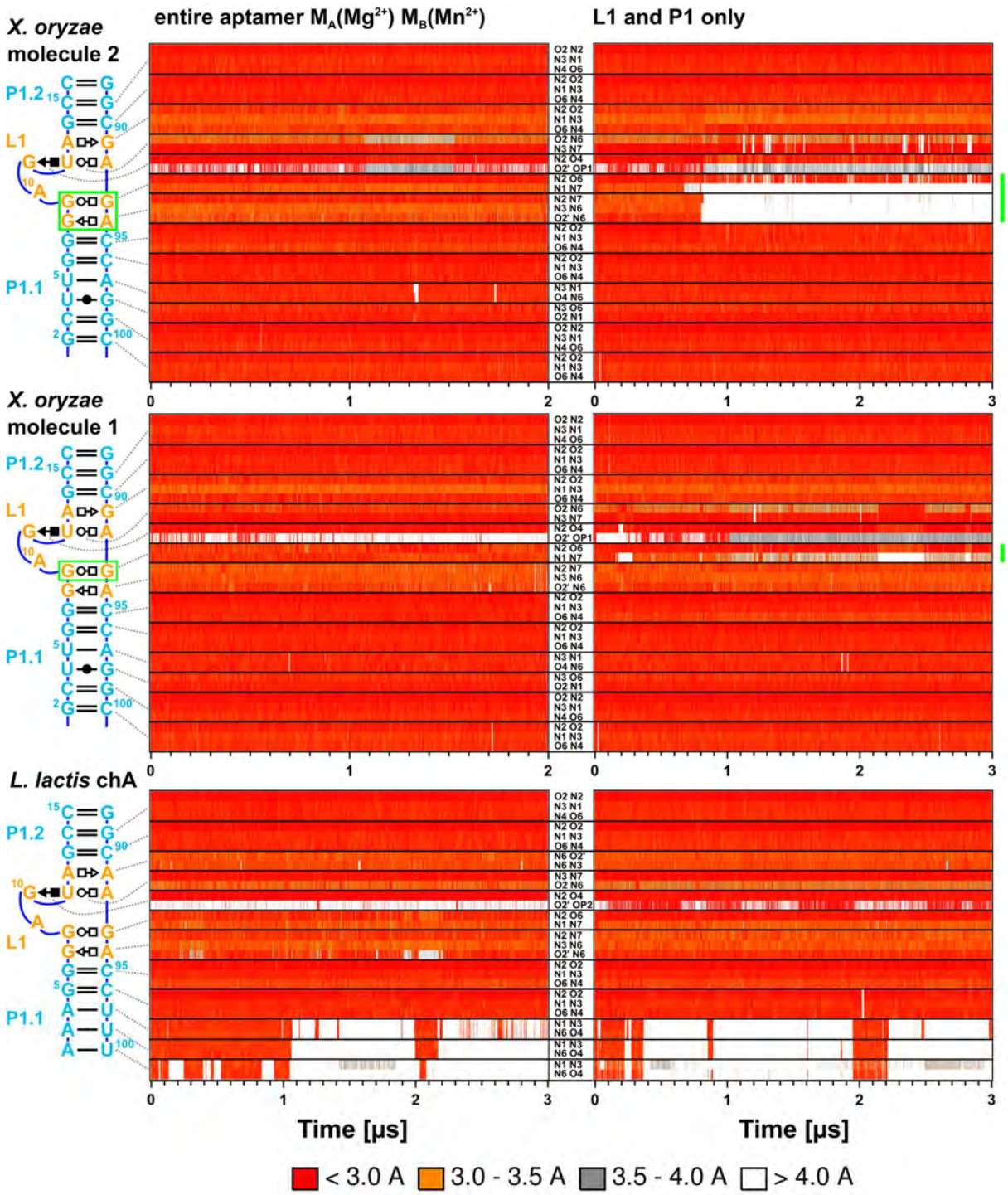

Supplementary Figure 22. Time evolution of native base pairing interactions of SRL-like motif of L1 in entire aptamer and in model structure (consisting only of P1.1, P1.2 and L1 and thus lacking A-minor interaction of A10 in *X. oryzae* and A9 in *L. lactis*, to L3 loop and P3 stem). The most labile interactions are highlighted in green.

Supplementary Figure 23

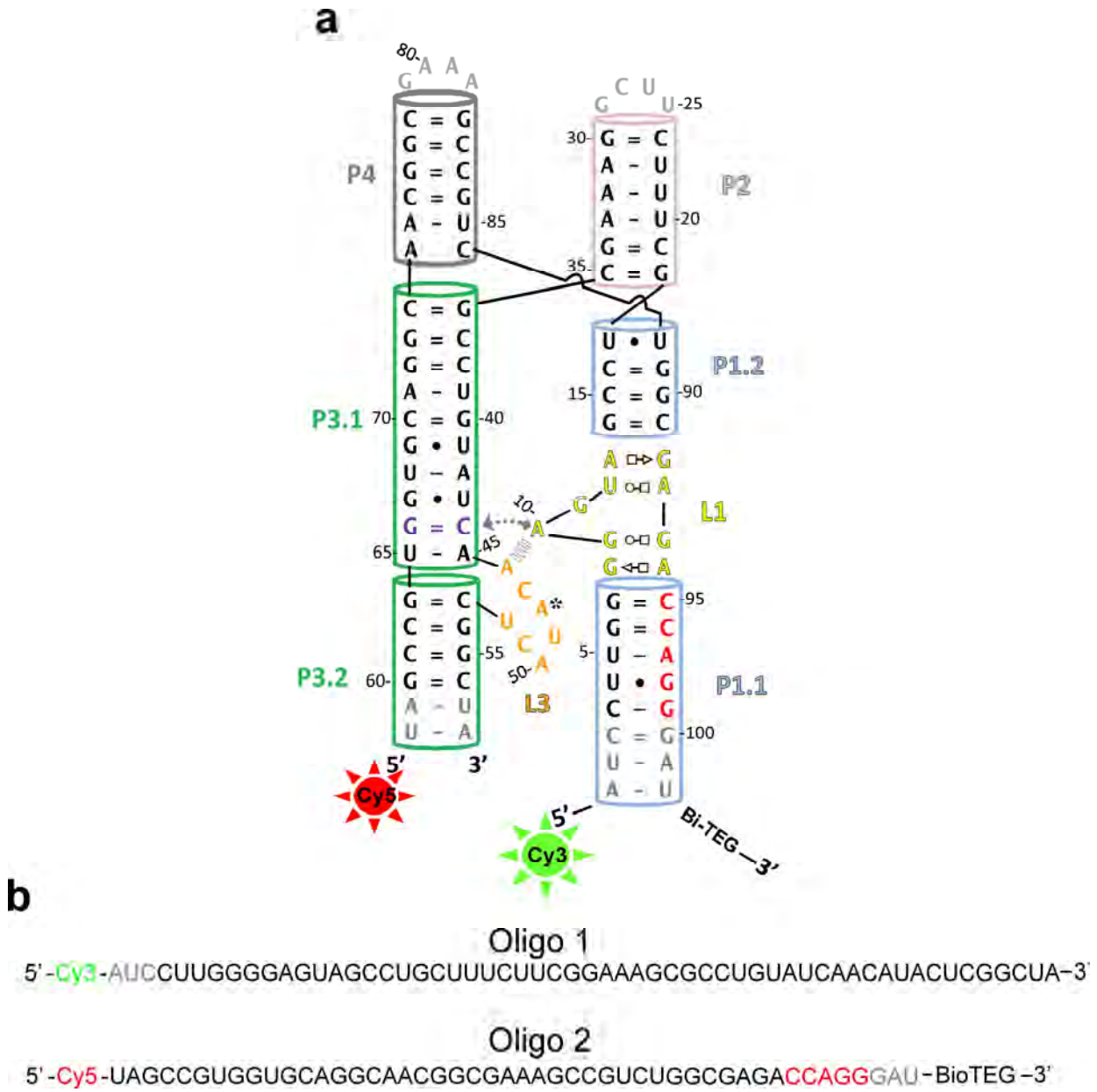

Supplementary Figure 23| smFRET construct design. (**a**) Sequence and secondary structure of the *Xory yybP-ykoY* riboswitch construct used for smFRET. The numbering of residues is kept consistent with the crystal construct of the RNA in Fig. 1a. The construct was made was hybridizing two chemically synthesized RNA oligonucleotides modifications at their 5' and 3' ends with Cy3, Cy5 fluorophores and Biotin-TEG. (**b**) Sequences of the two oligonucleotides with modifications used for the smFRET construct shown in (a)

Supplementary Figure 24

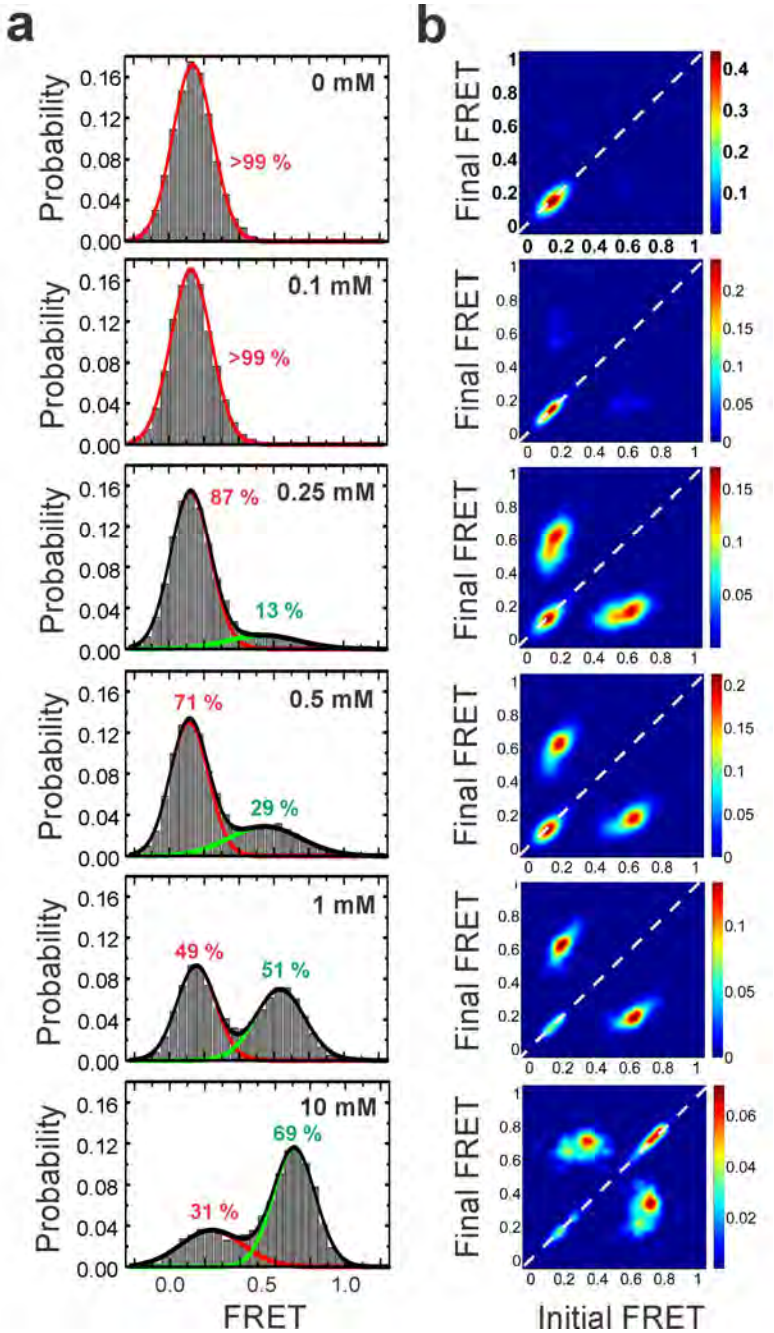

Supplementary Figure 24| Mg^{2+} titration of the WT *Xory* riboswitch. (a) FRET histograms showing the distribution of the two FRET states under various Mg^{2+} concentrations, fit to a sum of Gaussian functions. The Gaussian peaks for the low- and high-FRET states are shown in red and green, respectively, while the cumulative fit is shown in black. The histograms under 0 mM and 0.1 mM contain very low populations of the high-FRET state and were fit to a single Gaussian function. (**b**) TODPs under different Mg^{2+} concentrations showing the fraction of static 'on-diagonal' and dynamic 'off-diagonal' molecules. The SD populations under the high, 10 mM Mg^{2+} is evident in the TODP.

Supplementary Figure 25

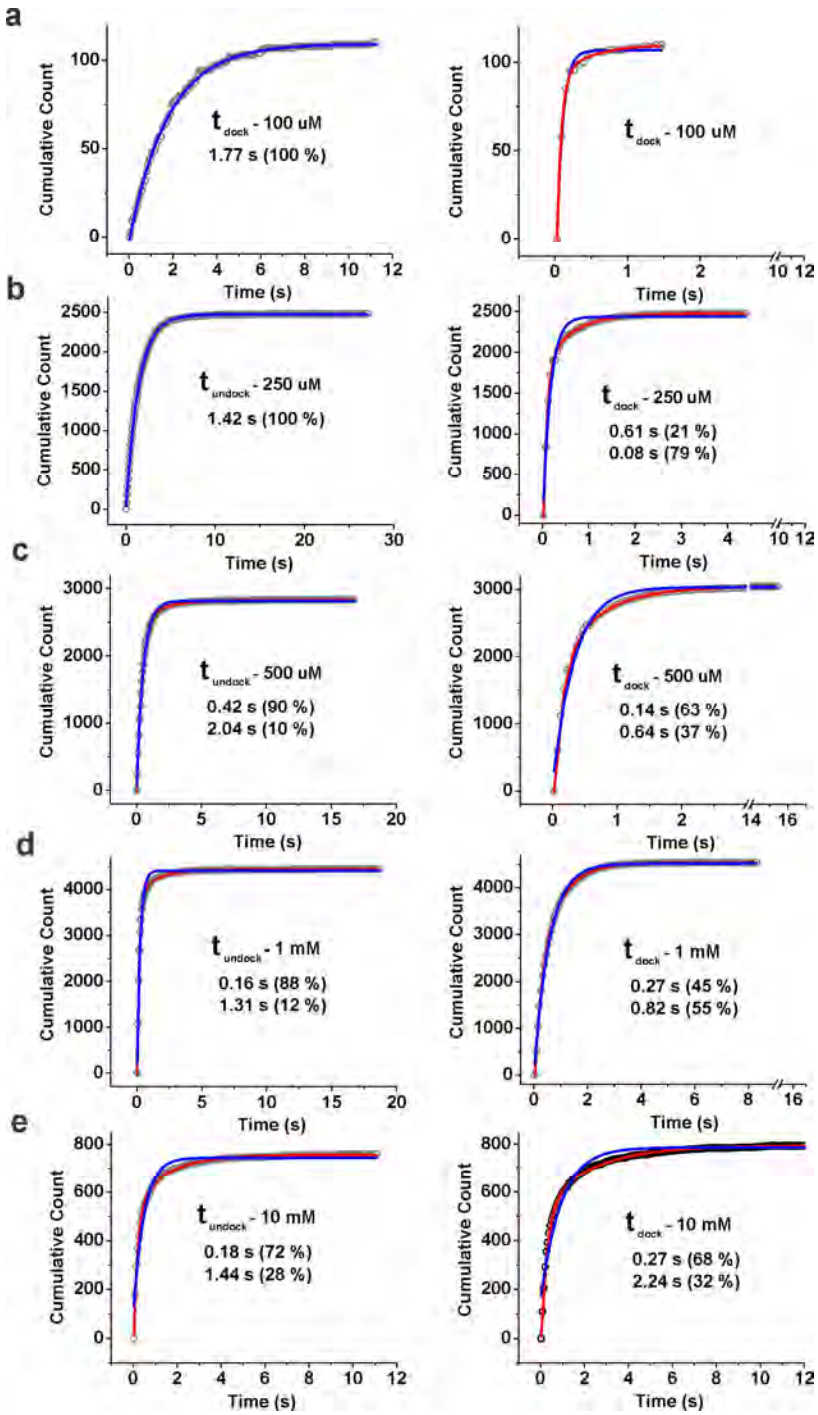

Supplementary Figure S25| Kinetics of WT *Xory* Mn^{2+} sensing riboswitch. (a) Cumulative dwell-time distributions of t_{undock} and t_{dock} in the presence of 0.1 mM $MgCl_2$ fit to single (blue) and double-exponential (red) are shown. The life-times and amplitudes of slow and fast components are also shown. In case of double-exponential fits, fit to single exponential function is also shown for comparison. **(b-e)** Same as in (a) but in the presence of 0.25 mM, 0.5 mM, 1 mM and 10 mM $MgCl_2$, respectively.

Supplementary Figure 26

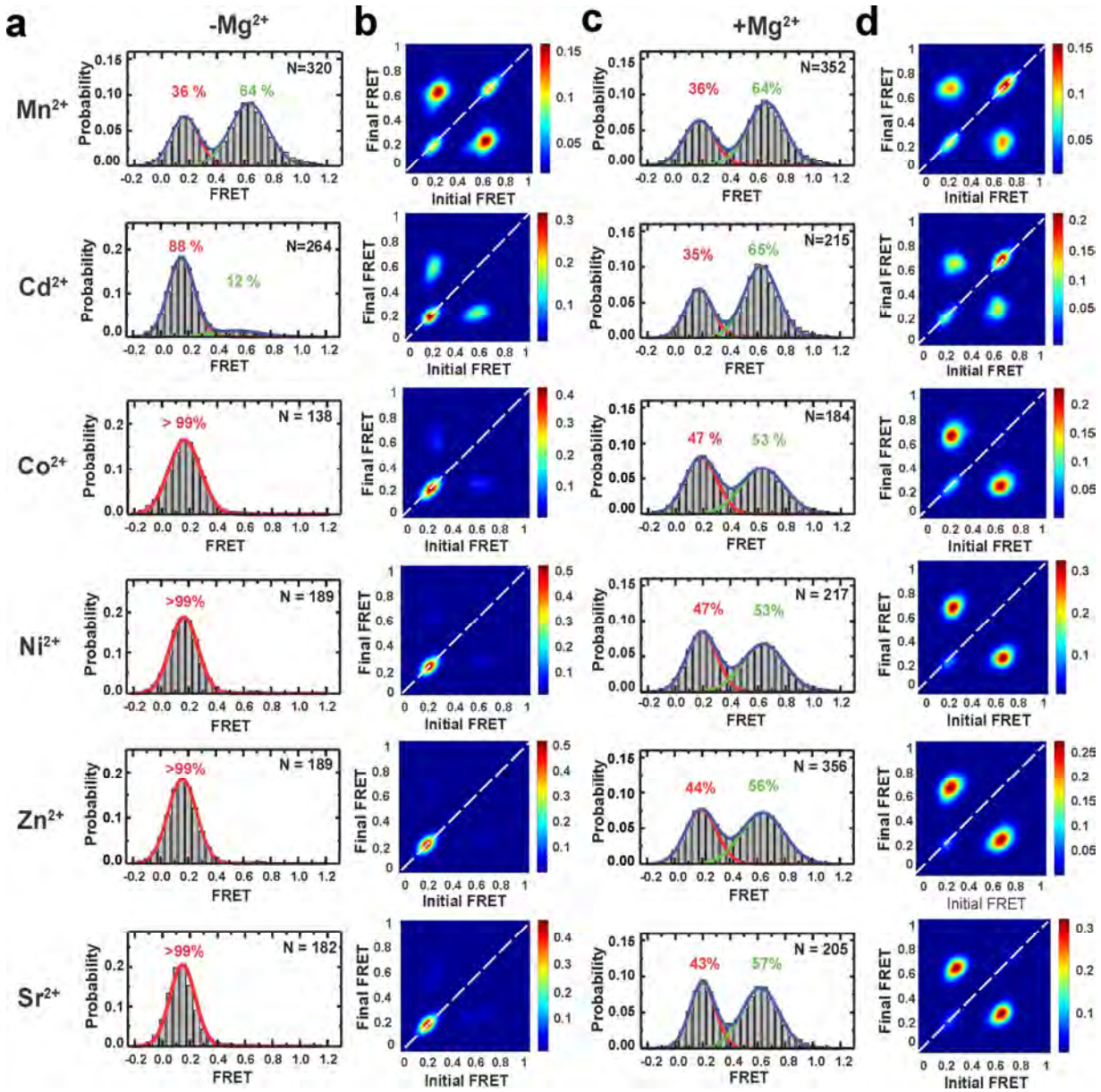

Supplementary Figure S26| Effect of different metal ions on the WT *Xory* riboswitch. (a) FRET histograms showing equilibrium distribution of docked and undocked conformations of the WT riboswitch at 0.1 mM concentration of different transition metal ions alone (i.e., in the absence of 1 mM $MgCl_2$). Gaussian fits to the docked, undocked are shown as green and red curves, while the cumulative fit is shown in blue. The number of molecules, N, for each condition analyzed and the % of docked and undocked conformations in each condition are indicated. **(b)** TODPs corresponding to the histograms in (a). **(c)** FRET histograms and **(d)** TODPs at 0.1 mM concentration of different metal ions in the presence of of 1 mM $MgCl_2$. For the different metal ions tested, except Mn^{2+} and Cd^{2+}, almost all the traces remained in SU conformation, with >95 % in the low-FRET (~0.1) undocked conformation, in the absence of Mg^{2+}.

Supplementary Figure 27

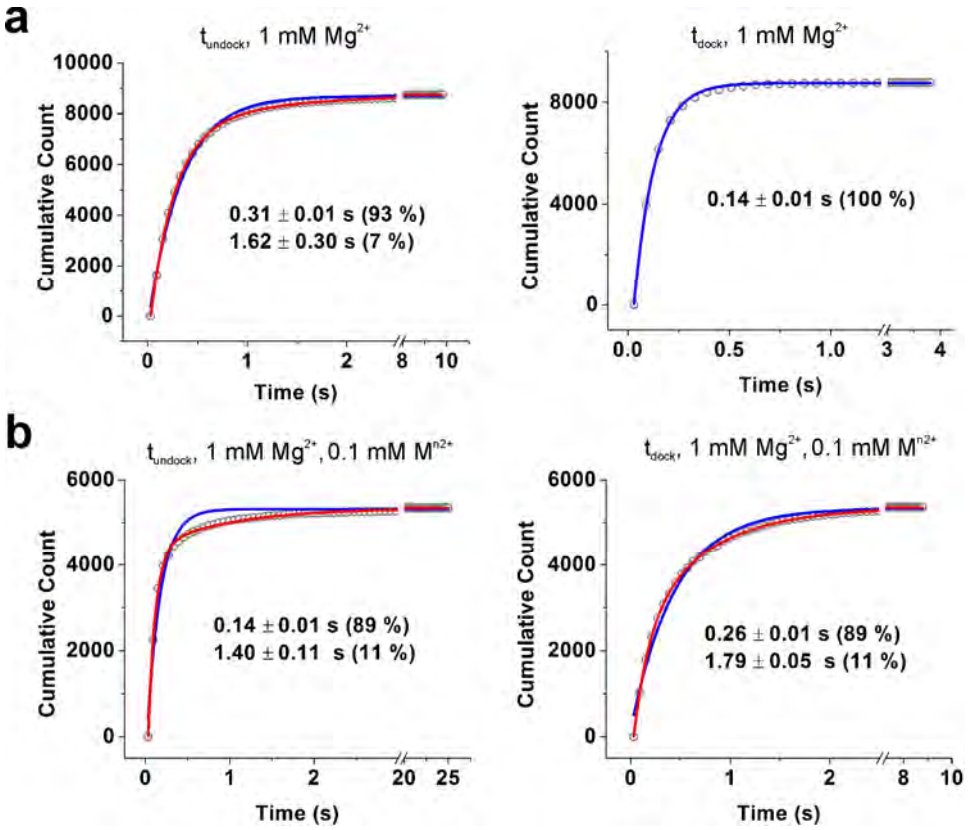

Supplementary Figure 27| Kinetics of the *Xory* riboswitch A48U mutant. (a) Cumulative dwell-time distributions of t_{undock} and t_{dock} in the presence of 1 mM $MgCl_2$ fit with single (blue) and double-exponential (red) functions. The life-times and amplitudes of slow and fast components are also shown. In the case of double-exponential fits, fit to single exponential is also shown for comparison. **(b)** Same as in (a) but in the presence of 1 mM $MgCl_2$ and 0.1 mM $MnCl_2$.

Supplementary Figure 28

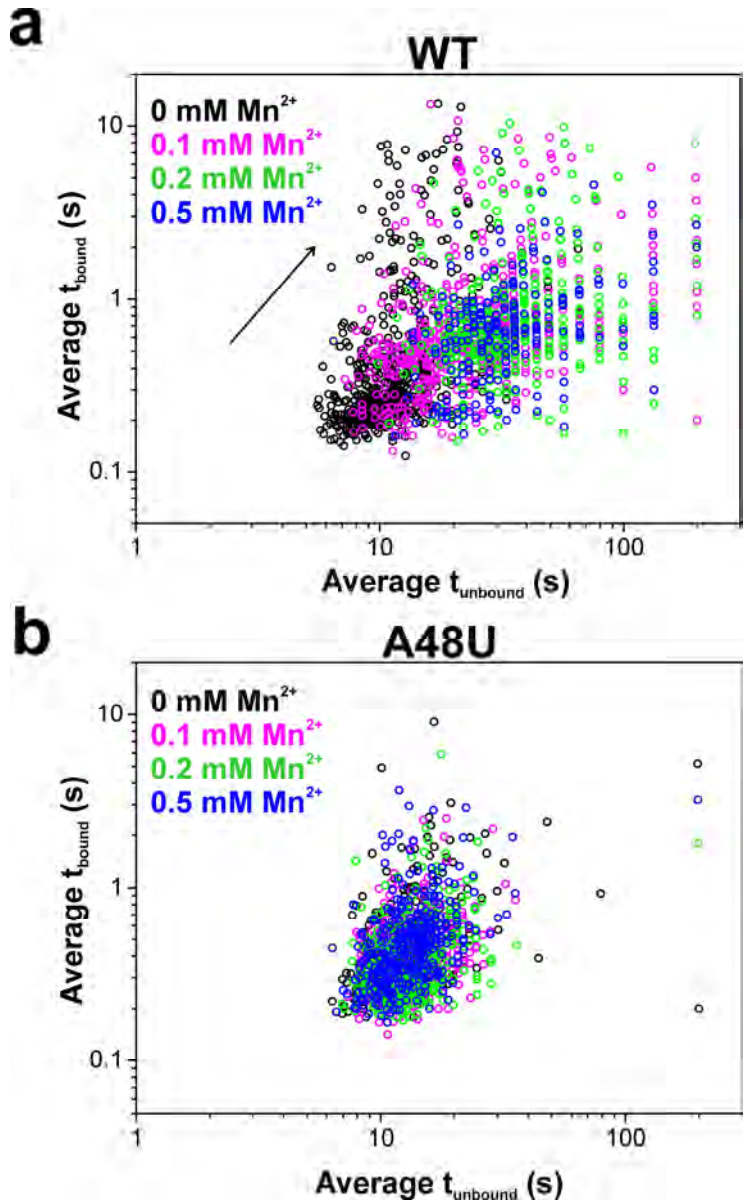

Supplementary Figure 28| Scatter plots of average bound and unbound times for the DNA oligo. (a) Scatter plot of average $t_{unbound}$ *vs* average t_{bound} of the DNA oligo to the WT riboswitch in the presence of 1 mM Mg^{2+} and different Mn^{2+} concentrations. For every condition, over 200 single-molecule binding traces, each containing multiple binding events are analyzed and the average $t_{unbound}$ and t_{bound} for individual traces are shown. The distribution shifts diagonally upwards and to the right indicating increasing average $t_{unbound}$ and t_{bound}, under increasing [Mn^{2+}] showing decreasing k_{on} ($1/t_{unbound}$) and k_{off} ($1/t_{bound}$). (**b**) Same as in (a) but for the A48U mutant riboswitch. The distribution remains similar overall under increasing [Mn^{2+}], showing little change in k_{on} and k_{off}.

Supplementary Figure 29

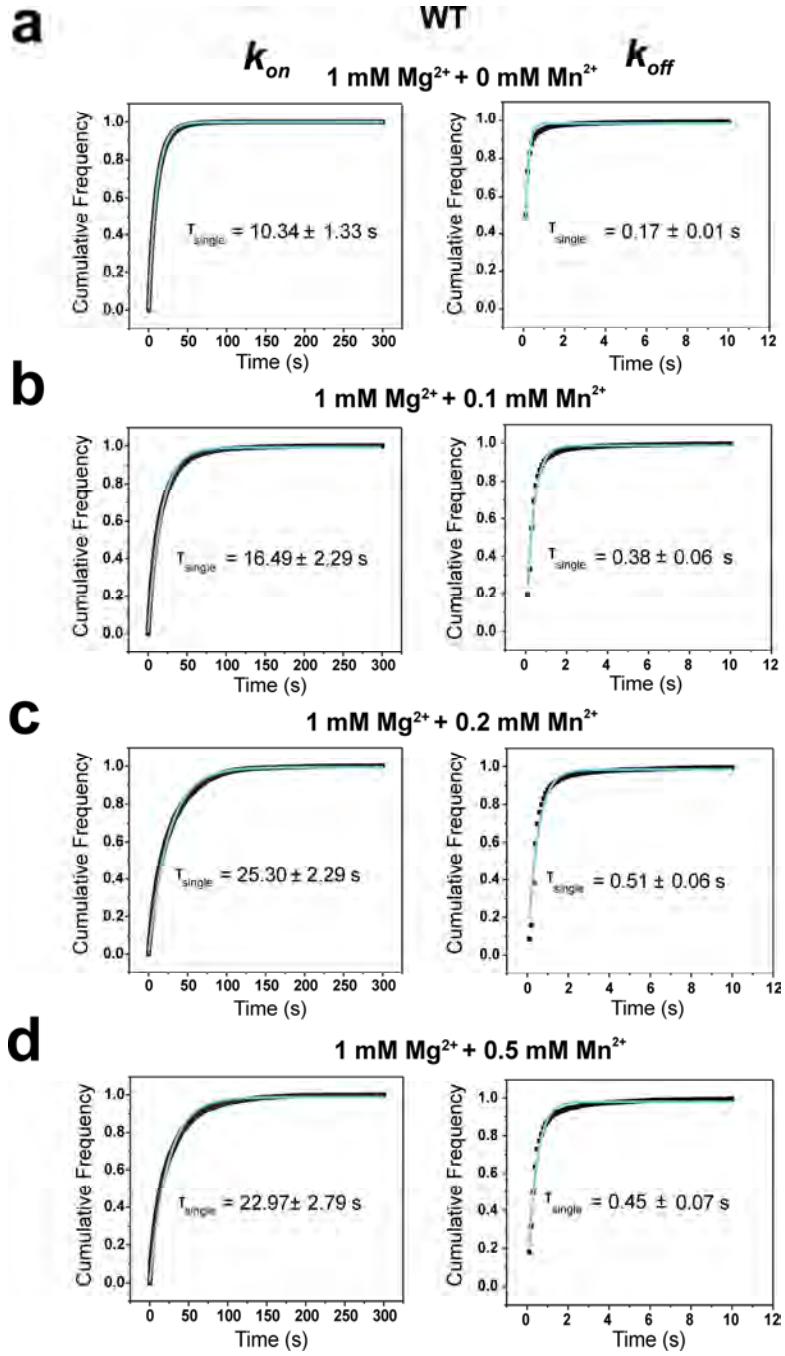

Supplementary Figure 29| Kinetics fits of SiM-KARTS data for the WT Mn^{2+} riboswitch. Cumulative dwell-time distribution plots of $t_{unbound}$ and t_{bound}, fit to single-exponential functions to obtain k_{on} and k_{off} in the presence of 1 mM Mg^{2+} and (**a**) 0 mM Mn^{2+}, (**b**) 0.1 mM Mn^{2+}, (**c**) 0.2 mM Mn^{2+}, and (**d**) 0.5 mM Mn^{2+}. The single-exponential fits to the data are shown in cyan along with the individual unbound and bound life-times.

Supplementary Figure 30

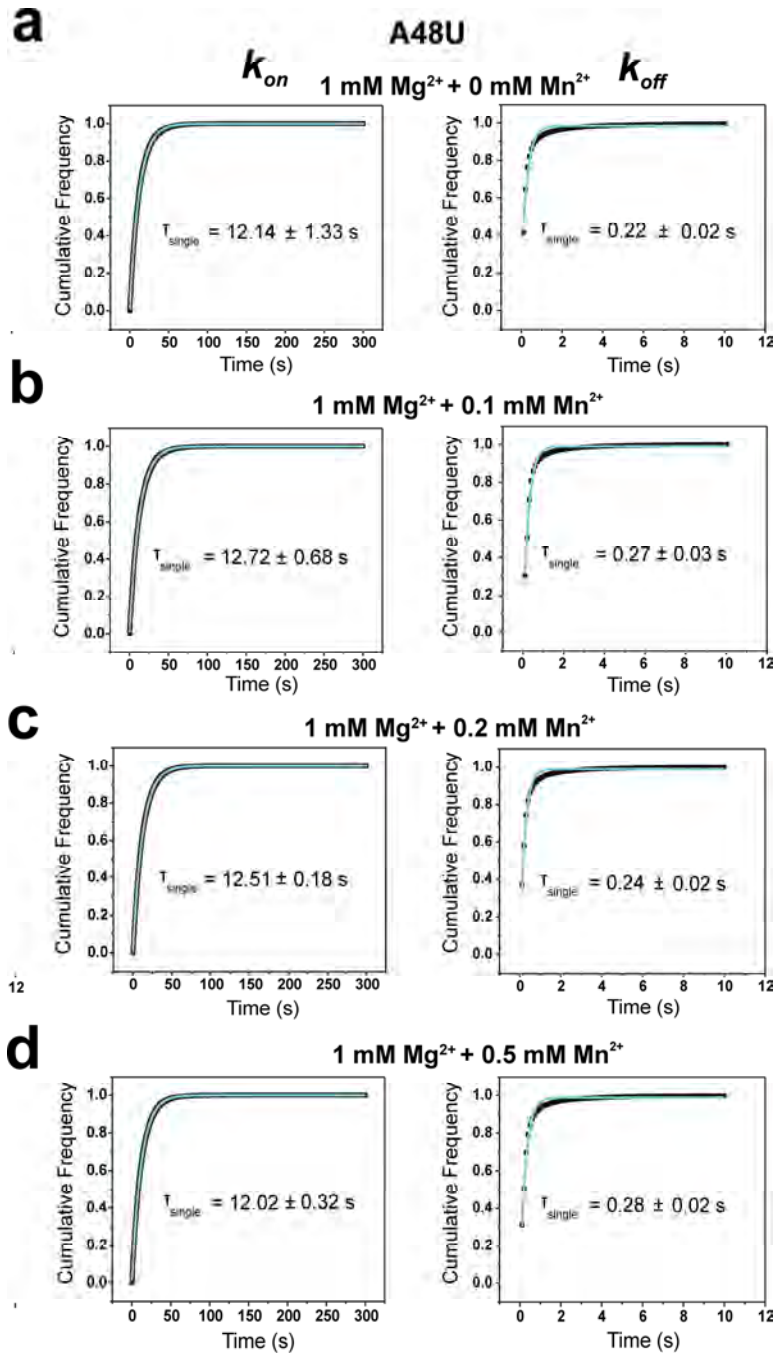

Supplementary Figure 30| Kinetics fits of SiM-KARTS data for the A48U mutant Mn^{2+} riboswitch. Cumulative dwell-time distribution plots of $t_{unbound}$ and t_{bound}, fit to single-exponential functions to obtain k_{on} and k_{off} in the presence of 1 mM Mg^{2+} and (**a**) 0 mM Mn^{2+}, (**b**) 0.1 mM Mn^{2+}, (**c**) 0.2 mM Mn^{2+}, and (**d**) 0.5 mM Mn^{2+}. The single-exponential fits to the data are shown in cyan along with the individual unbound and bound life-times.

Supplementary Note 1 Global structural dynamics of docked structures of aptamers in the MD simulations

To elucidate structural dynamics of the Mn^{2+} sensing riboswitch, we performed a set of explicit solvent MD simulations on microseconds time scale. In addition to simulations containing both M_A and M_B ion binding sites occupied by divalent ions, we performed a set of simulations testing the effect of replacement of these divalent ions by monovalents in each ion binding position separately or in both of them simultaneously (see **Supplementary Table 2**).

The global structural dynamics of the studied systems was visualized by the B-factors calculated per residues (**Supplementary Figure 7**). All simulations revealed similar trends in global structural dynamics except of behavior of L3 loop, which was found to be sensitive to type of ions in the M_A and M_B ion binding sites (see below). All stems exhibited high structural stability in all simulations. We observed larger fluctuations on the tips of P2, P3, and P4 stems. These fluctuations were found to be caused by unstacking of the L2 nucleotide, which should be considered as inherent part of native structural dynamics of GNRA tetraloops[2-6]. In the case of simulations of *L. lactis* structure, B-factor values indicated also large fluctuations of the P2 stem. Detailed analyses revealed that these fluctuations were connected with a reversible bending of the P2 stem and its movement toward and away from the P4 stem. This global movement was correlated with flipping of ε torsion angle of A28 nucleotide, which fluctuated between two states (see **Supplementary Figure 8**).

Supplementary Note 2 MD simulations confirmed *syn* orientation of A48 in L3 loop of *X. oryzae* structure Conformer 2

The electron density of the conformer 2 of the *X. oryzae* structure revealed adenine A48 in *syn*-rather than *anti*-conformation. In order to verify this unusual glycosidic bond orientation within the given structural context, we used two different refinements of the conformer 2 structure (**Supplementary Figure 9**) as starting structures for subsequent MD simulations. These simulations aimed to indirectly probe the orientation of A48 glycosidic bond via analyses of compatibility of a given orientation of A48 with its structural environment reflecting the native A48 orientation through molecular interactions. We thus expected that while simulation starting from native orientation of A48 will fluctuate around starting structure conformation, the non-native orientation of A48 in the starting structure should result in structural changes in initial phase of MD simulation. For sake of completeness, it is also possible that both orientations of A48 might coexist in the crystal lattice ensemble and electron density represents ensemble-averaged picture of A48, which is structurally compatible with its structural environment in both orientations. In such case, both A48 orientations would be equally tolerated by their structural environment and thus both would be equally stable in MD simulations.

Therefore, we performed MD simulations of conformer 2 both with *syn*- and *anti*-oriented A48. Namely, we compared simulations having their ion binding sites occupied by corresponding native divalent ions, i.e., by Mg^{2+} and Mn^{2+} in M_A and M_B, respectively (see

Supplementary Table 2). We observed that the simulation started from structure with *syn*-oriented A48 stably fluctuated around crystal conformation during the entire 2 μs simulation. In contrast, the simulation started with *anti*-oriented A48 revealed significant structural changes during initial phase of the simulation. Namely, the A48 nucleobase was shifted already in the initial geometrical optimization, so that it was coordinated to the Mn^{2+} ion by N7 nitrogen, while N6 exocyclic amino group was repelled away from the Mn^{2+} ion. This movement was accompanied by reconformation of the sugar-phosphate backbone between U52 and C53 that shifted away from A48 to avoid sterical clash (**Supplementary Figure 10**). Subsequently, in the early stages of the simulations, namely during thermal equilibration, such reconformation of U52-C53 sugar-phosphate backbone resulted in destabilization of the U52(H3)…A48(O2') hydrogen bond and exposure of the U52 into solvent (**Supplementary Figure 10**). All these rapid structural changes should not be considered as native structural dynamics of the riboswitch and are unambiguously a consequence of starting structure bias, namely non-native refinement of A48 *anti* orientation. Thus, in agreement with the observed electron density, we found that *anti*-oriented A48 is not compatible with the overall structure of Conformer 2 containing open-conformation of loop L3. Thus, crystallographic data together with MD simulations provide clear evidence of *syn*-orientated A48 in this particular L3 loop conformation; the MD simulations of Conformer 2 started with *anti*-A48 were not further analyzed and discussed.

For the sake of completeness, it is worth noting that MD simulations of Conformer 1 (containing closed conformation of loop L3 and A48 clearly resolved as *anti*-orientated) did not reveal any rapid structural changes during the early stage relaxation that would point to any doubts of the refinement of the L3 loop conformation.

Supplementary Note 3 MD simulations of chain A of the *L. lactis* 6CB3 structure support U44$^-$ to be deprotonated in this particular arrangement involving three Cd^{2+} ions

In chain A of the 6CB3 crystal structure, Bachas and Ferré-D'Amaré reported an unusual arrangement of the ion binding sites involving three Cd^{2+} ions. In this arrangement, the $M_{A,Mg}$ and M_C ions were heptacoordinate, while the ion in the $M_{B,Mn}$ site was reported to be hexacoordinate, in particular to two carbonyl groups of U44, the N7-nitrogen of A41, and three phosphate non-bridging oxygens of G40, U39, and G9. However, the U44(N3) nitrogen is located only 2.2 Å from the Cd^{2+} ion in the $M_{B,Mn}$ site, which raises the question of its protonation state and its potential role as the seventh inner-shell ligand of thus heptacoordinated Cd^{2+} ion in the $M_{B,Mn}$ site.

To address this question, we performed two sets of MD simulations, one set with a canonical U44 and another with N3-deprotonated U44$^-$. In each set, we performed simulations with different ions in the $M_{A,Mg}$, $M_{B,Mn}$, and M_C binding sites so that the $M_{A,Mg}$ and M_C binding sites were occupied by either a Mg^{2+} or K^+ ion, while $M_{B,Mn}$ involved either a Mn^{2+} or K^+ ion. This strategy yielded eight combinations of ion types in these three binding sites for each U44 protonation state (**Supplementary Table 1**).

Clear rearrangements of the ion binding sites were observed in all eight simulations with the canonical form of U44. We even observed complete ejection of the canonical U44 from the ion binding site and loss of its first-shell contacts to the ions in three out of eight simulations, including the simulation containing three divalent ions (two Mg^{2+} ions in the $M_{A,Mg}$ and M_C sites and one Mn^{2+} ion in the $M_{B,Mn}$ site; Figures S10 and S11). In contrast, the simulations containing an N3-deprotonated $U44^-$ revealed rather modest changes of the ion binding site arrangement and the $U44^-$ always kept at least some inner-shell contacts of the crystal structure (Figures S12 and S13). Nonetheless, despite the deprotonation of the $U44^-$, none of these simulations was able to completely reproduce all inner-shell contacts observed in the crystal structure. We hypothesize that the modest rearrangements are caused by the fact that we are using Mg^{2+} and Mn^{2+} (or monovalent K^+) ions instead of Cd^{2+} ions. Note that the large Cd^{2+} ions are generally more prone to tolerate heptacoordination and nitrogen ligands than the smaller Mn^{2+} and Mg^{2+}. Therefore, we suggest that the unusual arrangement of the binding site reported in chain A of the 6CB3 crystal structure is most likely induced by the presence of Cd^{2+} ion and requires an N3-deprotonated uracil U44.

Supplementary Note 4 Stacking pattern of L3

Most of the nucleobases from L3 loop form continuous stacking pattern (**Supplementary Figure 7 D,E** and **Supplementary Figure 19**). This segment is further stacked by its 5'-end on adenine A10 (A9 according to numbering of *L. lactis*) from L1 loop, which forms type I A-minor interaction with G66=C44 (G61=C37 according to numbering of *L. lactis*) base pair. This A-minor interaction together with part of the stacking pattern formed by the A10(A9) adenine and two nucleotides at 5'-end of L3 loop (i.e., A10|A46|C47 and A9|U39|C40 in simulation of structure from *X. oryzae* and *L. lactis*, respectively) represent rather rigid part of the stacking pattern, which was found to be stable in all ionic conditions (**Supplementary Figures 15-19** and **Supplementary Table 2**). In addition to the A-minor interaction making tertiary contact between L1 and L3 loops, the above-mentioned A10|A46|C47 (A9|U39|C40) part of the stacking pattern is stabilized also by other tertiary interactions such as hydrogen bonding of C47 (C40 according to numbering of *L. lactis*) cytosine with riboses of C53 and A45 (G46 and G38 in *L. lactis*) of the P3.2 stem (see Figures S19 and S20 for evolution of all tertiary contacts between A10|A46|C47 (A9|U39|C40) part of the stacking pattern and its structural environment). The insensitivity of this region to types of ions in M_A and M_B sites suggests that the L1-L3 loop tertiary contact mediated by this pattern might be formed in all ionic conditions even if M_A and M_B sites are not yet properly formed and occupied by the corresponding divalent ions.

The rest of stacking pattern of L3 loop (i.e., A48|U52|C51|A50 and A41|C45|U44|U43 in *X. oryzae* and *L. lactis* structures, respectively) showed different dynamics depending mostly on the type of ion in M_B site (**Supplementary Figures 15-19** and **Supplementary Table 2**). The presence of Mn^{2+} ion in M_B significantly stabilized native stacking pattern in L3 loop, while this pattern was destabilized in simulations where the Mn^{2+} ion was replaced by K^+. Surprisingly, when both divalent ions were replaced by K^+ ions, the stability of L3 loop stacking pattern was

higher than in case where only Mn^{2+} ion in M_B site was replaced by monovalent while M_A was occupied by Mg^{2+} ion, though still less stable than in simulations having also M_B site occupied by Mn^{2+}. In order to explain this observation, we hypothesize that stacking pattern of L3 loop represents inherently quite stable conformation of this loop with life-times, when formed, at least on microsecond time scale. However, when M_A binding site is occupied by Mg^{2+}, unlike K^+, it enforces proper positioning of A46 and U52 (U39 and C45 according *L. lactis* numbering) phosphates which leads to destabilization of the stacking pattern of L3. This stacking-structure-destabilization effect of Mg^{2+} can be overcompensated only by binding of Mn^{2+} ion into the M_B binding site.

Supplementary Note 5 Structural dynamics of SRL-like conformation of L1 in different structural contexts

Besides structures of the whole aptamer which all remained in docked state in our simulations, we also performed simulations of the structures consisting only of P1.1, P1.2 and L1 (based on *X. oryzae* – Conformers 1 and 2 and *L. lactis* crystal structures, see **Supplementary Table 2**). Such truncated structure obviously lacks all tertiary contacts to L3 loop and P3 stem and thus its dynamics should correspond to the dynamics of this particular part in undocked state.

The base-pairing (**Supplementary Figure 22**) as well as backbone conformation were monitored and compared to the corresponding values observed in the simulations of the complete aptamer, i.e., in the docked state. Note that the overall conformation of L1 loop as well as base pairing in P1.1 stem (with exception of terminal A-U base pairs of the P1.1 stem in simulation of *L. lactis* aptamer which revealed base pair fraying) were entirely stable in the simulations of complete aptamers. The most significant structural changes were observed in simulation of the isolated P1.2|L1|P1.1 structure based on Conformer 2 of the *X. oryzae* structure. The disruption of G9(N1)…G93(N7) H-bond was followed by reconformation of G8-A94 from *trans*-Sugar Edge/Hoogsteen into *cis*-Watson Crick base pairing and loss of the S-turn conformation of the sugar-phosphate backbone of G8-A10. Interestingly, the simulation of the same structural motif derived from the Conformer 1 of *X. oryzae* crystal structure showed less pronounced changes, in particular, the G9(N1)…G93(N7) H bond was broken and recreated several times. Finally, in case of the simulation based on *L. lactis* structure, the L1 loop resembled conformation observed in the complete aptamer; however, we observed rather significant loss of pairing in P1.1 stem. This may be due to a weaker P1.1 in *L. lactis*, which is shorter by one base pair and has three A-U base pairs capping the stem, as opposed to the two G-C base pairs in the *X. oryzae* structure.

In summary, the data indicate that when A10 is sequestered in the A-minor interaction, the P1.2|L1|P1.1 segment adopts a conformation resembling the topology of a canonical sarcin-ricin loop. Compared to the sarcin-ricin loop consensus sequence, the A10 nt is inserted between its GpU platform and the flexible region. In addition, the trans-Hoogsteen/Hoogsteen base pair in the flexible region adjacent to the GpU platform is replaced by a trans-Watson-Crick/Hoogsteen

pair. When the A10 is not involved in the tertiary interaction, it instead destabilizes the SRL-like topology.

Supplementary Note 6 The *yybP-ykoY* riboswitch can discriminate between similar transition metal ions

The selectivity of the *Xory* riboswitch for Mn^{2+} over Mg^{2+} arises in part from the inner-sphere contact with A48(N7), suggesting that other soft transition metal ions may also be recognized[7]. To test this hypothesis, we probed the effects of different divalent metal ions on the conformation of the riboswitch, at 0.1 mM concentration alone or in the presence of 1 mM Mg^{2+}. FRET histograms showed that out of all the different metal ions tested, Cd^{2+} is most effective in promoting docked conformations (**Fig. 5b, Supplementary Fig. 26**). In the presence of 1 mM Mg^{2+}, addition of 0.1 mM Cd^{2+} resulted in ~65 % of the high-FRET docked conformation, comparable to the docked population upon addition of 0.1 mM Mn^{2+}. Examination of individual smFRET traces as well as the TODP showed that this is due to a large fraction of SD traces (**Supplementary Fig. 26**), in agreement with the tight binding of Cd^{2+} to the *yybP-ykoY* riboswitch shown recently[7]. Among the other metals tested, Ni^{2+}, Co^{2+}, Sr^{2+} or Zn^{2+} had little effect on promoting the folded conformations of the riboswitch under these conditions. Interestingly, in the absence of Mg^{2+}, while 0.1 mM Mn^{2+} alone led to the appearance of DD and SD traces with ~62 % docked population (mean FRET 0.67±0.12) (**Fig. 5c**), 0.1 mM of Ni^{2+}, Co^{2+}, Sr^{2+} or Zn^{2+} did not affect SU traces and Cd^{2+} had only a small effect in promoting DD traces (**Supplementary Fig. 26**). This suggests that, while Mg^{2+} and Mn^{2+} may both bind at $M_{A,Mg}$, Cd^{2+} may be more specific to the $M_{B,Mn}$ site. These results suggest that while the *Xory* riboswitch has some degree of plasticity in recognizing ligands, in a background of Mg^{2+}, it preferentially recognizes Mn^{2+} and Cd^{2+} and can effectively discriminate against similar divalent transition metal ions.

Supplementary Discussion

Comparison of Xory Mn^{2+} bound structures to Cd^{2+} bound structures

With respect to the recent finding that Cd^{2+} can also bind to the *yybP-ykoY* riboswitch[7], our smFRET results and unpublished data from a *yybP-ykoY* and Broccoli-based fluorescent sensor agree with this conclusion. However, our structure (at 2.96 Å resolution) and previous ones with Mn^{2+} cannot provide strong evidence for or against their intriguing argument for heptacoordination as the mechanism of spescificity for Mn^{2+}. While Cd^{2+} is heptacoordinated in the Llac-MntP structure (PDB ID 6CC3), with water as its seventh ligand, it is not clear how that water could enable a mechanism of specificity for Mn^{2+} against other metals. Further, in the highest-resolution structure (6CB3), Cd^{2+} at M_B was found to be hexacoordinate. The Llac-alx structure (6CC1) is also modelled as bound in a heptacoordinate fashion to M_B, with the seventh ligand here coming from a second phosphoryl oxygen from the same phosphate of U44.

However, this structure is similar to all of our Mn^{2+}-bound structures, in that the resolution is not high enough to show the subtle difference in orientation of a phosphate that would be required to distinguish hexa- from heptacoordination. As for the M_A site, our Cd^{2+}-only smFRET data suggest that M_A probably prefers either Mg or Mn over Cd^{2+}. Upon inspection of their data, M_A does not appear clearly heptacoordinate in any of their structures. It is actually octacoordinated in the *Llac* structure with Cd/Mg/Ba (PDB 6CB3) and another claim (Llac-MntP) relies on placed waters not seen in the electron density. A very high-resolution structure of a *yybP-ykoY* riboswitch with Mn^{2+} is required to address this interesting question. In any case, taken together with our structures, these prior structures agree with the finding of flexibility in the Mn-binding area, even when the riboswitch ligand is bound. It is a separate question whether Cd^{2+} is a biologically relevant ligand, as it is typically considered toxic and xenobiotic for most organisms, and its high-affinity binding to enzymes at sites of other metals is generally considered aberrant[8].

Supplementary References

1. Bottaro, S., Di Palma, F. & Bussi, G. The role of nucleobase interactions in RNA structure and dynamics. *Nucleic Acids Res.* **42**, 13306-14 (2014).
2. Kuhrova, P., Banas, P., Best, R.B., Sponer, J. & Otyepka, M. Computer Folding of RNA Tetraloops? Are We There Yet? *J. Chem. Theory Comput.* **9**, 2115-25 (2013).
3. Sponer, J.E. et al. Theoretical studies on the intermolecular interactions of potentially primordial base-pair analogues. *Chemistry (Easton)* **16**, 3057-65 (2010).
4. Menger, M., Eckstein, F. & Porschke, D. Dynamics of the RNA hairpin GNRA tetraloop. *Biochemistry* **39**, 4500-7 (2000).
5. Zhao, L. & Xia, T. Direct revelation of multiple conformations in RNA by femtosecond dynamics. *J. Am. Chem. Soc.* **129**, 4118-9 (2007).
6. Kuhrova, P. et al. Computer Folding of RNA Tetraloops: Identification of Key Force Field Deficiencies. *J. Chem. Theory Comput.* **12**, 4534-48 (2016).
7. Bachas, S.T. & Ferre-D'Amare, A.R. Convergent Use of Heptacoordination for Cation Selectivity by RNA and Protein Metalloregulators. *Cell Chem Biol* **25**, 962-973 e5 (2018).
8. Begg, S.L. et al. Dysregulation of transition metal ion homeostasis is the molecular basis for cadmium toxicity in Streptococcus pneumoniae. *Nat Commun* **6**, 6418 (2015).